UNIVERSITY OF SOUTHAMPTON

FACULTY OF PHYSICAL SCIENCES AND ENGINEERING

School of Electronics and Computer Science

Nano Research Group

Simulation of Total Ionizing Dose and Random Dopant Fluctuations in sub-100 nm transistor nodes

by

Eleni Chatzikyriakou

Thesis for the degree of Doctor of Philosophy

March 8, 2017

UNIVERSITY OF SOUTHAMPTON

ABSTRACT

FACULTY OF PHYSICAL SCIENCES AND ENGINEERING
School of Electronics and Computer Science

Doctor of Philosophy

SIMULATION OF TOTAL IONIZING DOSE AND RANDOM DOPANT FLUCTUATIONS IN SUB-100 NM TRANSISTOR NODES

by Eleni Chatzikyriakou

Finite Elements Method simulations of Total Ionizing Dose in two state-of-the-art transistor nodes are presented: The 45 nm Partially-Depleted Silicon-on-Insulator MOSFET and the 22 nm bulk FinFET. A systematic method has been developed to study charge trapping in field isolation oxides using the simulation software Sentaurus device. The method is based on solving transport equations for carriers in the oxide. Aspects of simulation of interface trap formation through de-passivation from ionic hydrogen are discussed. This includes transport of hydrogen species in the device and state transitions. Calibration of the trapping model is performed using experimental results on Buried OXide irradiated capacitors of 400 nm SiO_2. The extracted parameters are then used in the two FET technologies examined. In both cases, increased radiation hardness of the devices, tested using the bulk traps method, up to total doses of 600 KRad(SiO_2) in the case of the PDSOI and 1 MRad(SiO_2) in the case of the FinFET is shown. In the 45 nm node, Random Dopant Fluctuations (RDFs) using the Sano and the Impedance Field Method are examined in combination with charge introduced in the field oxide regions. RDFs are shown to have a significant effect in the sub-threshold characteristics of the irradiated devices during the weak inversion of the parasitic transistor induced in the device. Their effect is negligible, however, when the parasitic channel is fully formed.

Contents

List of Figures

List of Tables

List of Publications

1. E. Chatzikyriakou, K. Potter, and C. H. De Groot, ‘A systematic method for simulating Total Ionizing Dose effects using the Finite Elements Method,’ J. Comp. El. (Submitted).
2. E. Chatzikyriakou, W. Redman-White, and C. H. De Groot, ‘Simulation of the combined effects of Total Ionizing Dose and Random Dopant Fluctuations in the 45 nm PDSOI node,’ Microelectronics Reliability, 2016.
3. E. Chatzikyriakou, K. Potter, W. Redman-White, and C. H. De Groot, ‘Three- dimensional Finite Elements Method simulation of Total Ionizing Dose in 22 nm bulk nFinFETs,’ Nucl. Instruments Methods Phys. Res. Sect. B Beam Interact. with Mater. Atoms, 2016. doi: 10.1016/j.nimb.2016.09.007
4. E. Chatzikyriakou, K. Potter, W. Redman-White, and C. H. De Groot, Finite Elements Method simulation of leakage path formation in 22 nm bulk FinFETs under Total Ionizing Dose, COSIRES 2016, Loughborough, UK.
5. E. Chatzikyriakou, K. Morgan, P. Ashburn, W. Redman-White, C. H. De Groot, Total Ionizing Dose and random dopant fluctuation effects in 65- nm gate length partially depleted Silicon-on-Insulator nMOSFETs, IEEE NANO 2015, 659662. doi: 10.1109/NANO.2015.7388691.
6. E. Chatzikyriakou, C. H. De Groot, Simulation and Modelling of Commercial Transistor Technologies under Total Ionizing Dose, Nanogroup meeting 2015, University of Southampton.
7. K. Potter, E. Chatzikyriakou, K. Morgan, C. H. De Groot, Total Ionizing Dose Radiation Effects in CMOS Transistors and Memory, Nanogroup meeting 2014, University of Southampton.
8. K. Potter, K. Morgan, C. Shaw, P. Ashburn, W. Redman-White, and C. H. De Groot, ‘Total ionizing dose response of fluorine implanted Silicon-On-Insulator buried oxide,’ Microelectronics Reliability, 2014, vol. 54, no. 910, pp. 23392343.

Acknowledgements

This PhD taught me that the most treasured source of happiness in someone's life is to be surrounded by people that share the same values.

Useful conversations and comments where provided by Dr Nicholas Wyn Owen at R.A.L., Dr Marc Gaillardin and Prof. J. L. Leray at CEA/DAM, Prof. R. D. Schrimpf at Vanderbilt University and Dr. Ioannis Zeimpekis in the University of Southampton.

My warmest and kindest thank you to to Prof. C.H. de Groot for trusting me with this thesis.

Through the toughest times, it was not the love of my parents that pushed me back to motion, it was my father's tears for the lives of the people that die each day and his love for humanity. It is our wish and our best interest the products of research to be used for us and not against us.

This PhD project was supported by the UK Engineering and Physical Sciences Research Council (EPSRC) award No. 1304067. The author would like to acknowledge the use of the IRIDIS High Performance Computing Facility, and associated support services at the University of Southampton.

List of Symbols

β	Reciprocal thermal energy (V^{-1})
$\boldsymbol{J_n}$	Electron current density (A/cm^2)
$J_{\boldsymbol{p}}$	Hole current density (A/cm^2)
$\boldsymbol{S_{n,p}}$	Carrier flux density through the interface (cm^{-2}s^{-1})
$\dot{D}$	Dose rate (Rad/s)
ϵ	Electrical permittivity of material (F/cm)
μ_n	Electron mobility (cm^2/Vs)
μ_p	Hole mobility (cm^2/Vs)
ϕ	Electrostatic potential (V)
ρ	Density (g/cm^3)
σ_n	Capture cross sections of electron trapping sites (cm^2)
σ_p	Capture cross sections for hole trapping sites (cm^2)
$\boldsymbol{E}$	Magnitude of electric field (V/cm)
c	Particle capture rate in MSC (cm^{-3}s^{-1})
c^n_{CB}	Capture of an electron from the conduction band (cm^{-3}s^{-1})
c^p_{CB}	Capture of a hole from the conduction band (cm^{-3}s^{-1})
c^n_{VB}	Capture of an electron from the valence band (cm^{-3}s^{-1})
c^p_{VB}	Capture of a hole from the valence band (cm^{-3}s^{-1})
D	Total Dose (Rad)
D_i	Diffusion coefficient (cm^2/s)
D_n	Diffusion coefficient for electrons (cm^2/s)

D_p	Diffusion coefficient for holes (cm^2/s)
d_c	Carrier density (cm^{-3})
E_act	Process activation energy (eV)
e^n_CB	Emission of an electron to the conduction band (cm^{-3}s^{-1})
e^p_CB	Emission of a hole to the conduction band (cm^{-3}s^{-1})
E_C	Conduction band energy (eV)
E_di	Diffusion activation energy (eV)
$E_{\mathrm{F},n/p}$	Carrier quasi-Fermi energies (eV)
E_F	Equilibrium Fermi energy (eV)
E_I	Intrinsic Fermi energy (eV)
E_trap	Energy level of the trap (eV)
e^n_VB	Emission of an electron to the valence band (cm^{-3}s^{-1})
e^p_VB	Emission of a hole to the valence band (cm^{-3}s^{-1})
E_V	Valence band energy (eV)
f_n	Electron occupation probability
f_p	Hole occupation probability
f_y	Hole yield
g_n	Degeneracy factor for electron traps
g_p	Degeneracy factors for hole traps
G_ehp	Electron-hole pair generation rate (cm^{-3})
H_i	Inner energy of a transition state (eV)
j_n	Drift coefficient for electron traps
j_p	Drift coefficient for hole traps
k_c	Reciprocal long-range Coulomb force screening length (cm^{-1})
m	Sentaurus fitting parameter for carrier yield
m_e	Electron effective mass
m_p	Hole effective mass

n	Density of mobile electrons (cm^{-3})
n_1	Intrinsic electron concentration (cm^{-3})
N_A	Doping concentration (cm^{-3})
N_A^-	Concentration of ionized acceptors (cm^{-3})
N_D^+	Concentration of ionized donors (cm^{-3})
n_0^{B}	Electron equilibrium density in semiconductors with Schottky metal contact (cm^{-3})
N_{at}	Areal charge density (cm^{-2})
N_{C}	Conduction band density of states (cm^{-3})
n_{I}	Intrinsic carrier density (cm^{-3})
n_{t}	Concentration of electron trapping sites (cm^{-3})
N_{V}	Valence band density of states (cm^{-3})
$n_{i,\mathrm{eff}}$	Effective intrinsic concentration in the oxide (cm^{-3})
p	Density of mobile holes (cm^{-3})
p_1	Intrinsic hole concentration (cm^{-3})
p_t^+	Concentration of trapped holes (cm^{-3})
p_0^{B}	Hole equilibrium density in semiconductors with Schottky metal contact (cm^{-3})
p_{t}	Concentration of hole trapping sites (cm^{-3})
r_0	Maximal transition frequency (s^{-1})
R_{net}	Net recombination term (cm^{-3}s^{-1})
s_i	Transition state occupational probability
t_{ox}	Thickness of the oxide (cm)
v_{th}	Particle thermal velocity (cm/s)
W_{dep}	Depletion region width (cm)

List of Constants

g_{SiO2}	Irradiation factor	7.6×10^{12}	ehp × cm^{-3} × rad(SiO_2)
h	Planck's constant	6.62×10^{-34}	m^2kg/s
m_0	Free electron mass	9.11×10^{-31}	kg
$v_{\mathrm{th}}{}^{\mathrm{n}}$	Electron thermal velocity	2.0420×10^{7}	cm/s
$v_{\mathrm{th}}{}^{\mathrm{p}}$	Hole thermal velocity	1.5626×10^{7}	cm/s
q	Electron charge	1.6×10^{-19}	C
k	Boltzman's constant	8.625	eV/K

Chapter 1

Introduction

In a radiation harsh environment, electron devices experience disturbances from many different sources. In space, depending on the altitude or deep-space mission journey followed, the sources of radiation may include energetic protons and other nuclei from Galactic Cosmic Rays as well as energetic electrons and protons in the Van Allen belts. Solar flares, emitting electromagnetic radiation of different wavelengths, including gamma rays and X-rays, can be sensed both in space and at sea-level on Earth a few days after a major eruption on the Sun's surface (Figure 1.1).

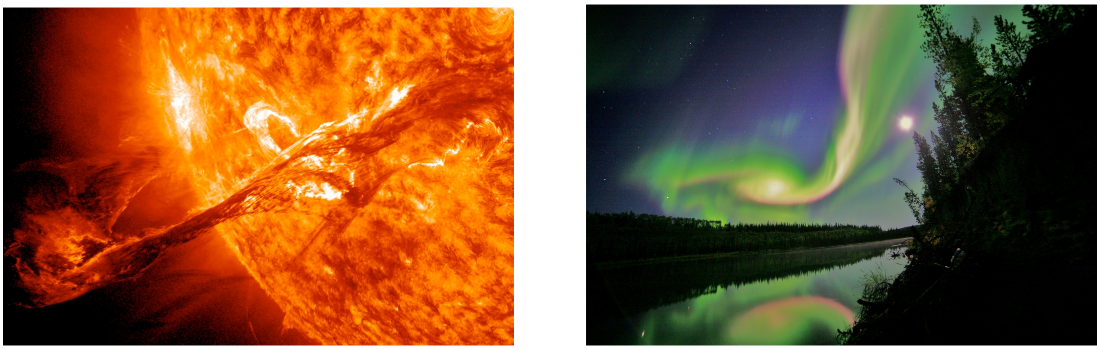

(a) Eruption of a long filament on the Sun's surface captured by NASAs Solar Dynamics Observatory (SDO) on August 31, 2012

(b) Aurora over Whitehorse, Yukon on the night of September 3, 2012

Figure 1.1: Coronal mass ejection, originating from an explosion on the surface of the Sun, travelling at over 900 miles per second and interacting with the Earth's magnetosphere [1].

Every year, a number of satellites experience temporary or permanent failure for many reasons, including failures in electronic and electrical equipment. The space weather processes contributing and leading to failure of on-board devices are very complex and difficult to analyse as all required data might not be available. For example, in [2], electrical effects due to electrostatic discharges were examined using telemetry data related to 26 anomalies in solid-state power amplifiers of Inmarsat satellites over a period of 16 years and compared with space weather data. According to their findings, deep dielectric charging was the main cause of failure during declining phases of the solar cycle from charges accumulating in the materials after high-energy electron fluxes. However, as the study also points out, it is quite challenging to connect the source of radiation with its subsequent effect. Historically, some cases have been well documented and attributed to specific effects. As a notable example, the Hubble Space Telescope's mission STS-31 experienced Random Access Memory bit flips and high photomultiplier tube counts in its fine guidance system on separate occasions while passing through the South Atlantic Anomaly. The latter caused guide star acquisition failures while both were attributed to ionization effects [3].

In high-energy physics establishments such as particle accelerators for physics experiments, nuclear power plants and fusion energy devices (tokamaks), energetic particles used for their operation and their ionizing products (fluxes of gamma and X-rays) gradually degrade electronic devices operating close to areas of increased exposure [4]. Sensory equipment, robotic control and telemetry and data acquisition electronics can all be affected in such harsh environments [5]. Further to this, electronics operating close to medical equipment that produces radiation of hazardous nature to them, can be reduced in their lifespan or temporarily malfunction i.e. by preventing a bit to be zeroed. In this work, degradation that occurs due to charges accumulating in the isolation regions of transistors and preventing normal on-off operation will be examined. Our focus will be on the effects of ionizing radiation and specifically due to gamma rays incident in the structure.

Ionizing radiation is the term used to describe radiation capable of ionizing matter. Total Ionizing Dose (TID) is the measure of incident radiation on the material that is capable to produce free electrons inside it following different physical mechanisms such as Compton scattering [6]. Electron-hole pairs created inside the isolation regions of the electronic devices by such processes cause positive charges to become trapped and leakage paths to be formed. This can lead to a total loss of the transistor by not allowing it to turn off. The effect is persistent until the charge trapped is annealed which may take days to months, or if the ionizing radiation persists, may never occur. TID is used to differentiate between soft errors occurring in logic devices (Single Event Effects-SEEs) that are caused by a trail of charges induced by energetic particles passing through the active regions and bulk of devices and collected at the electrodes.

The attempt to make electronic devices more resilient to radiation is referred to as hardening and the final product as rad-hard device. Hardening can be of different types and at different levels. Hardening by process is performed at the technology level and involves changing materials, fabrication designs and processes to suite particular needs for harsh environments. Hardening by design involves changing the structure of the Integrated Circuits in ways that can mitigate the effects of radiation [7], for example with the use of redundant components in order to avoid downtime. Error detection and correction functions for soft errors such as those implemented in MRAM technologies and Field Programmable Gate Arrays (FPGAs) can also mitigate the effects of radiation. Except for these error correction techniques, FPGAs provide the added advantage of correcting firm errors that occur in memory cells that control logic functions or in routing matrices by rebooting the FPGA [8].

There are many commercial-off-the-self solutions for electronics with different specifications operating in a range of harsh environments by companies such as Aitech Defense Systems, Space Micro Inc. and BAE Systems. These technologies are usually behind state-of-the-art commercial technology nodes for general use due to the time required for testing and customizing. However, as device sizes become smaller there are many indications such as the thinning of the gate isolation region in transistors and the smaller volumes introduced in Silicon-on-Insulator technologies that show that mainstream commercial technologies could potentially be useful for radiation harsh environments. The combination of TID-hardened mainstream commercial processes and hardware such as Field Programmable Gate Arrays (FPGAs) can contribute to solutions that are robust against both TID and SEEs.

Step-by-step examination of integrated circuits (from technology to design) for use in radiation environments is employed by the hardening community. Examination of commercial transistor technologies gives a measure of their suitability for specific uses. Simulations play an integral part in the device design and scaling. However, the processes involved in the examination of the TID effects spread in a wide range from the microscopic level to device physics.

Finite Elements Method (FEM) simulations of Total Ionizing Dose have the potential to provide very detailed and accurate results to technology designers through the use of rate equations and defect state occupational probabilities. Analytical models as well as models with more details on the microscopic level have been devised for various situations. These models are or can be incorporated relatively easy in the device simulators. Despite this fact, FEM simulations of TID are not common in the literature, or their use is restricted to simplified models of fixed charge.

In this work, we systematically simulate charge trapping in SiO_2. We use the simulation software Synopsys TCAD. Bulk oxide trapping can be simulated using the drift-diffusion model and trapping equations coupled with Poisson's equation [9]. Simulation of interface trap formation can also be achieved with the use of transport equations for hydrogen species and defect state transitions [10]. We apply the charge trapping method to a two dimensional Partially-Depleted Silicon-on-Insulator (PDSOI) technology and a three-dimensional bulk FinFET technology.

Approaching the deep sub-micron regime, Silicon-on-Insulator (SOI) Field Effect Technologies dominated high-performance computing such as network servers and low power applications for mobile and hand-held devices [11]. The small active silicon volume of

SOI transistors that is isolated from the rest of the substrate, has also been shown to offer better immunity to transient errors [12–14]. Transient effects result from ionized particles going through the active silicon volume leaving a trail of charges that is then collected at one of the terminals.

Variability plays a crucial role in device yield. But it has also been shown that device variability can produce a significantly different post-irradiation response in devices where pre-irradiation variability gives no measurable response deviation [15]. Many factors such as stress and geometrical differences in the active silicon region can affect variability in the radiation response of deep sub-micron SOI MOSFETs [16–19]. Finding the exact reason behind such variations through experimental means is not easy since all factors fluctuate at the same time and there is no way of controlling all but the parameter of interest. In [20], the case of Random Dopant Fluctuations is examined in combination with traps located in the gate dielectric using simulations. In this work, the variability due to random dopant fluctuations (RDF) in the radiation response of the 45 nm PDSOI technology node is examined through simulation methods. RDFs is a significant source of variability [21], with [22] suggesting a percentage of 50% of the total variability from all sources.

In Chapter 3, the computational aspects of this study are presented through describing the basics of the FEM. Theoretical details of carrier transport and trapping in the oxide in combination with device models used to realistically simulate the TID effects are discussed, while also a description of the two methods used for the RDF simulations (the Sano and the Impedance Field Method - IFM) is given. In Chapter 4, system calibration to experimental results for the trapping model of irradiated 400 nm SiO_2 capacitors is shown. Extraction of interface trap densities performed through a computational method is also presented. The use of state transitions for the simulation of interface trap formation after irradiation is discussed. In Chapter 5, RDF simulations on the IBM 45 nm PDSOI nMOSFET node are shown complemented by two-dimensional simulations of TID. In Chapter 6, calibration of the 22 nm nFinFET to the Intel node and TID simulation results are presented.

Chapter 2

Total Ionizing Dose in deep sub-micron Field Effect Transistors

The continued scaling of state-of-the-art transistors dictates gate oxide thinning to follow the reduction in gate length in order to sustain performance and power improvement. The reduced thickness of such dielectrics leads to fewer trapped charges and tunnelling, thereby making them more robust to TID effects. Instead, TID response of state-of-the-art deep sub-micron transistors is dominated by charge trapping in field oxides such as the Buried OXide (BOX) and the Shallow Trench Isolation (STI) [23].

When irradiated, these oxides gather charges which cause drain-to-source leakage current in nFETs. Positive charges trapped in field oxides of SOI technologies cause two main parasitic transistors to be formed: a) at the Si/BOX interface and b) at the sidewall interface of the Silicon with the STI (Figure 2.1) [24–26]. In PDSOI devices, this parasitic transistor has been shown to be formed at the bottom corner of the silicon with the STI [27].

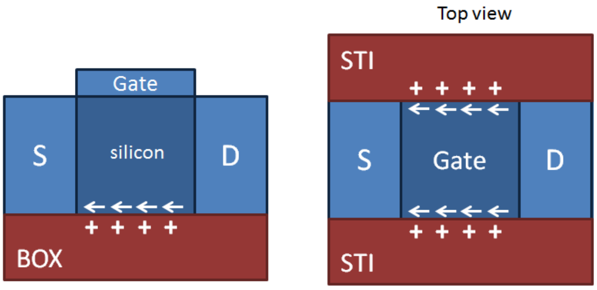

Figure 2.1: Leakage paths formed at the back (left) and sidewall channel (right) of a SOI MOSFET

The areal charge required in the oxide to turn on a parasitic channel is equal to the doping concentration in the depletion region of this channel:

$$N_{\text{ot}} = N_{\text{A}} x_{\text{d,max}} = \frac{(4q\epsilon_s N_{\text{A}} \phi_{\text{F}})^{1/2}}{q} \tag{2.1}$$

where q is the electronic charge, N_{A} is the doping density in silicon at the interface with the oxide, $x_{\text{d,max}}$ is the maximum depletion width of the channel and ϕ_{F} is the bulk potential with a concentration of N_{A} [13]. In other words, the formation of the inversion channel is very much dependent on the doping concentration extending to the 'walls' of the silicon.

PDSOI nMOSFETs of the 90 nm node and below incorporate high body doping on the order of 10^{18} - 10^{19} cm^{-3} to suppress short channel effects. Therefore, these devices have shown increased tolerance to TID provided that this doping level reaches the interfaces with the oxide [16, 19, 28]. On the other hand, Fully Depleted SOI nMOSFETs have lower doping levels which makes them more susceptible to parasitic channel inversion. Furthermore, their post-irradiation response is degraded since the top silicon layer is fully depleted and this causes coupling between the back and front channels of the device [13]. A high current regime similar to that of latch-up has also been observed in FDSOI with no body contacts [29].

TID in nFETs with multiple gates has been examined by several groups [30–34]. SOI nFinFETs have a geometry-dependent radiation response that is driven by electrostatic coupling. For example, 40 nm wide Ω-FETs have shown increased tolerance when compared to wider FinFETs (10 μm). This is because the electrostatic behaviour in the fin in the first case is dominated by the lateral gates, reducing the contribution of the back gate to the front channel conduction [35, 36]. Also, positive gate bias during irradiation worsens TID response as the charges are trapped closer to the interface of the BOX with the Si, therefore increasing contribution of the back-gate. In all cases, variation in the post-irradiation response is suppressed with increasing number of fins [37].

TID response of bulk nFinFETs shows similar dependence to the geometry of the fin with that of SOI nFinFETs, namely devices with wider fins exhibit reduced - to minimized - off-state current [38]. The I_{off} variation of the devices with more fins is averaged out and therefore TID appears less pronounced than in single-fin devices [39]. Also, devices with larger gate lengths have exhibited increased radiation hardness. The worst bias condition for irradiation in 90 gate-length nFinFETs has been shown to be the OFF state (V_{g} = 0 V, V_{ds} = 50 mV) [39]. The TID response in this case depends on the distribution of the trapped charge in the STI, as shown in the Figure 2.2.

Therefore, PDSOI technologies of present commercial applications as well as narrow width bulk nFinFETs are both interesting for the radiation hardening community. However, the small dimensions of these devices raise questions of variability, such as RDFs.

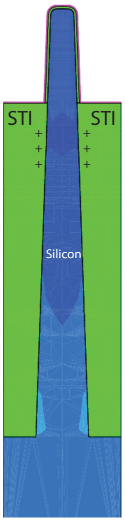

Figure 2.2: Cross section of a bulk FinFET showing the locations where charge will be trapped in the STI at the neck of the fin

RDFs produce threshold voltage (V_t) shifts in the front gate channel, but can also produce V_t shifts of the parasitic channels of the device. This can potentially create a spread in the off-state leakage current after irradiation.

RDFs result from the statistical nature of the density of discrete dopant atoms found in the depletion region of the scaled devices. For example, for a PDSOI MOSFET with W/L=100/30 nm, doping concentration $N_A = 5\times10^{18}$ cm^{-3} and depletion region width $W_{dep} = 1.6\times10^{-6}$ cm, the average total number of dopant atoms is N=240. The standard deviation of N is $\sigma_N = \left\langle (\Delta N)^2 \right\rangle^{1/2} = N^{1/2}$=15.5 which is about 6.5% of the original density [40]. On the other hand, FinFETs are fully depleted devices that only include doping for the purpose of controlling V_{th} for specific applications [41]. This makes this problem less prevalent in this technology [42–44].

TID response of any technology, however, is not only dependent on the configuration of the doping concentration in silicon, but also on the density of trapped charge in the oxides and its distribution at specific locations. Charge trapping mechanisms are largely affected by the bias conditions of the device as they define the electric field in the oxides. The bias-dependence for various SOI devices have been examined by several groups [45–48]. FEM simulations have the capacity to provide details on the charge distribution under specific bias conditions. However, many authors adopt the fixed oxide charge approach in their simulations, which creates a lot of issues in accurately describing radiation effects. For example, in [49] unrealistic humps are observed in the I-V simulation results due to the charges included in the top silicon corner, where they contribute to the increase of the electric field and the creation of a corner parasitic structure.

The physics and chemistry of the mechanisms involved in carrier trapping in SiO_2 have been examined extensively over the years. A number of studies have been made on crystal structure defects in quartz and α-SiO$_2$ using Electron Paramagnetic Resonance and Electron Spin Resonance techniques. The existing defects observed over the years go with the notation of E'-centers. E$_1$' in quartz and E$_\gamma$' and E$_\delta$' in α-SiO$_2$ [50–52].

Oxygen vacancies are at the heart of these defects. The E$_\gamma$' center has been found to be a deep hole trap, having an anisotropic spin distribution. It is thought to be an oxygen vacancy that undergoes asymmetric relaxation. In the neutral state, Si atoms nearby oxygen vacancies bond to form a dimer. In the positively charged state, one of these Si atoms relaxes and bonds with a fourth oxygen atom. [52–54]. There is no consensus over the exact nature of the E$_\delta$' center. It is a shallow hole trap. Prevailing theories are that it is either single oxygen vacancy that remains in the dimer state in both the charged and neutral states [55] or a cluster of four vacancies of E$_\gamma$'-like dangling bonds [56–61].

In many cases, Si/SiO$_2$ interface states have been shown to increase under total ionizing dose and this has been largely attributed to reactions with hydrogen species [62–66]. Most noted reaction thought to take place at the interface in such cases is

$$\mathrm{SiH} + \mathrm{H}^+ \rightarrow \mathrm{D}^+ + \mathrm{H}_2 \tag{2.2}$$

where D is the dangling bond whose final state will depend on the electrostatic potential at the interface [67–71].

Earlier theories that atomic hydrogen is the mobile species responsible for the de- passivation process have been refuted by the conclusion that H$^+$ is more stable than H in SiO$_2$ [64, 72]. The origin of H$^+$ in (2.2) has been a subject of investigation. Primary mechanisms thought to be responsible are H$_2$ cracking in positively charged states in the oxide bulk and H$_2$ cracking at hydrogenated defects in the oxide after capture of a hole [73].

Interface states are the cause of increased base current in bipolar transistors and therefore have been studied in the relevant context [74–76]. This effect has been shown to exhibit a dose-rate dependence called Enhanced Low Dose Rate Sensitivity (ELDRS), with increased interface state formation observed under low dose rates [77–79]. It is customary to distinguish between time-dependent effects and true dose rate effects (ELDRS) [80, 81]. Also, dependencies of H$_2$ concentration in hermetically sealed packages during irradiation has been studied in bipolar transistors in an effort to distinguish between the exact microscopic mechanisms taking place. [74, 82, 83].

Space charge effects have been examined in the past for the case of high dose rates (HDR). Holes trapped close to the interface can create an electrostatic barrier for protons to migrate there and create additional interface traps [81, 84]. Bimolecular recombination between electrons and holes under HDR has also been used in order to explain

ELDRS effects [79]. In [83] it is shown that bimolecular recombination does not differ from the simple fractional yield equation and similarly space charge effects are not significant, unless in very high dose rates of 100 Rad(SiO_2)/s and beyond. Furthermore, in the same work, the competing hydrogen dimerization process has been shown to be significant in devices irradiated under 1% H_2 per volume, while H_2 cracking becomes more important as H_2 concentration in the environment increases further.

Hydrogen transport and interface state creation can be included in the FEM simulator in a self-consistent manner. Sentaurus device has the capacity to simulate transport of hydrogen species and reactions between them. Also, interface states can assume different configurations (i.e. passivated, de-passivated, positively or negatively charged). This is achieved using the Multi-State Configurations functionality.

Chapter 3

Computational and analytical methods

3.1 Finite Elements Method Basics

In electronics, FEM simulators aim at the computation of the current on the device terminals when a voltage is applied. This is done by solving Poisson's equation in combination with carrier transport inside the device volume, namely, dividing the structure into small pieces called elements. The division creates geometric structures as those shown in Figure 3.1. Vertices are points where lines, areas, edges etc. intersect. Edges define lines where areas intersect, while elements are areas enclosed by edges.

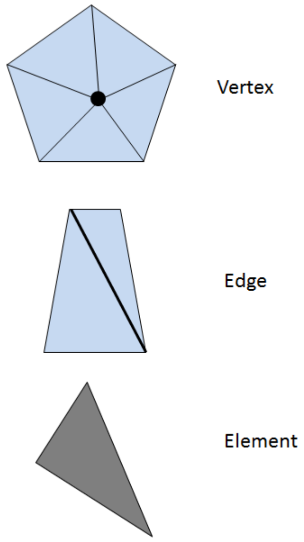

Figure 3.1: Meshing elements in FEM simulators

Mesh elements can be either two- or three-dimensional. The solution of all required equations is found at the vertex points between them. This is done by first defining shape functions for the elements. Some values remain constant inside them (i.e. space charge). For others, a gradient exists to preserve continuity of the solution [85]. The device under study can be either in equilibrium or in non-equilibrium conditions. In the former case, the simulation is called quasi-stationary. The sweep can be performed either on the voltage at an electrode, or on some other model from a list of possible models. Such an example is the DoseRate parameter of the RadiationBeam used during our simulations. Non-equilibrium conditions are simulated using the transient functionality where calculations are performed as a function of time. Bias can be applied here too, at time intervals specified by the user.

Correct operation of device simulations dictates proper use of models and parameters. It is the responsibility of the simulation designer to assure results are physical, realistic and according to existing theories. In the case of deep sub-micron technologies, quantum effects need to be taken into consideration and there are various models that can be used to explain the arising changes in device characteristics. For the case of TID examined in this work, the simulator has been ‘tweaked’ into solving carrier transport equations in the oxides for the carriers that are generated through irradiation by defining the regions to be semiconducting. To achieve this, all the theoretical aspects involved in the process had to be carefully examined.

The FEM device solver is used in combination with processing simulation in the Technology Computer Aided Design (TCAD) suite Synopsys Sentaurus. Process simulation is used to simulate processing steps as those taking place in the lab (deposition, etching etc.). Similar meshing rules apply during processing as those for device simulation. Typical examples of equations include material growth based on temperature and time, implantation of species in materials based on dose and energy and diffusion of dopant atoms from position of higher to position of lower concentration.

3.2 Ionizing dose and charge trapping

In the drift-diffusion formalism of carrier transport in the oxides used here, the generated carrier pairs that are considered are those that have escaped the initial recombination. The amount of pairs that escape the initial recombination is dependent on the electric field in the oxide, namely, higher electric field produces more electron-hole pairs. This is modelled using the carrier yield.

After this initial separation, the electrons are thought to move fast towards the electrodes while the holes that remain follow a slower motion towards areas of lower electrostatic potential. The motion of holes has been explained using different mechanisms and models, however, the net effect is for the holes to move with a low mobility which is derived experimentally by their time-of-flight [9]. ‘Late’ recombination is taken into account using the same model as that in semiconductors (eg. Shockley-Read Hall). Only hole trapping is considered in this work as this is thought to be the dominant trapping mechanism taking place in SiO_2.

3.2.1 Electron-hole pair creation and initial recombination

For gamma rays incident in the oxide, the electron-hole pair generation rate is calculated using the generation term G_{ehp} ($\mathrm{cm}^{-3}\cdot\mathrm{s}^{-1}$) [86], given by

$$G_{\mathrm{ehp}} = \dot{D} \cdot g_{\mathrm{SiO2}} \cdot f_{\mathrm{y}}\left(\boldsymbol{E}\right) \tag{3.1}$$

with $\dot{D}$, the dose rate ($\mathrm{rad(SiO_2)/s}$), g_{SiO2} is the 'irradiation factor' that is calculated here using

$$g_{\mathrm{SiO2}} = \frac{\rho}{w} \cdot 6.24 \cdot 10^{13} = 7.6 \cdot 10^{12} \mathrm{ehp} \times \mathrm{cm}^{-3} \times \mathrm{rad}\left(\mathrm{SiO_2}\right)^{-1} \tag{3.2}$$

ρ = 2.196 is the density ($\mathrm{g/cm^3}$) [87] and w = 18 eV is the energy required to create an electron-hole pair [76]. We are also taking into account that 1 rad = $6.24 \cdot 10^{13}$ eV/g.

As mentioned previously, a fraction of the electron-hole pairs gets recombined after their initial creation. The percentage of non-recombined carrier pairs is calculated using 'carrier yield' , f_y, and is a function of the electric field.

$$f_{\mathrm{y}}\left(\boldsymbol{E}\right) = \left(\frac{|\boldsymbol{E}| + E_1}{|\boldsymbol{E}| + E_2}\right)^m \tag{3.3}$$

where $\boldsymbol{E}$ is the local electric field (V/cm) , E_1, E_2 and m are fitting parameters.

3.2.2 Carrier transport

Starting from the Poisson's equation, the trapped holes density term is added to describe their contribution to the electrostatic potential in the oxide,

$$\boldsymbol{\nabla} \cdot \left(\epsilon \boldsymbol{\nabla} \phi\right) = -q\left(p - n + N_{\mathrm{D}}^{+} - N_{\mathrm{A}}^{-} + p_{\mathrm{t}}^{+}\right) \tag{3.4}$$

where q is the electron charge, ϵ is the absolute permittivity of the material, N_{D}^{+} and N_{A}^{-} are ionized donor and acceptor impurities. The oxide in our simulations is considered to be an intrinsic semiconductor, therefore, these values do not play a significant role. p_{t}^{+} is the density of the trapped holes (cm^{-3}).

The electron and hole continuity equations for our simulations that include charge trapping take the following form [76, 86, 88],

$$\frac{\partial n}{\partial t} = \frac{1}{q}\boldsymbol{\nabla}\cdot\boldsymbol{J_n} + G_{\mathrm{ehp}} - R^{n}_{\mathrm{nt}} \tag{3.5}$$

$$\frac{\partial p}{\partial t} = -\frac{1}{q}\boldsymbol{\nabla}\cdot\boldsymbol{J_p} + G_{\mathrm{ehp}} - R^{p}_{\mathrm{pt}} \tag{3.6}$$

where $\boldsymbol{J_{n,p}}$ in the electron and hole current densities (A/cm^2) which can be given by

$$\boldsymbol{J_n} = qn\mu_n E + qD_n\boldsymbol{\nabla}n \tag{3.7}$$

$$\boldsymbol{J_p} = qp\mu_p E - qD_p\boldsymbol{\nabla}p \tag{3.8}$$

where $D_{\mathrm{n,p}}$ is the diffusion coefficient for electrons and holes and $\mu_{n,p}$ is the electron and and hole mobility. The recombination terms in the continuity equations are given in Section 3.2.6.1.

The continuity equations in quasi-stationary state, become

$$-\frac{1}{q}\boldsymbol{\nabla}\cdot\boldsymbol{J_n} = G_{\mathrm{ehp}} - R_{\mathrm{SRH}} \tag{3.9}$$

$$\frac{1}{q}\boldsymbol{\nabla}\cdot\boldsymbol{J_p} = G_{\mathrm{ehp}} - R_{\mathrm{SRH}} \tag{3.10}$$

where the term R_{SRH} is equal for both electrons and holes and is given in Section 3.2.6.2.

3.2.3 Trapped Charge

We use the occupational probability of a trap to describe the state of the trap. The probability of a trap being occupied by an electron is f_n , and the probability of it being occupied by a hole is $f_p = 1 - f_n$ [89]. This is a number between 0 and 1 which when multiplied by the number of trapping sites gives the number density of the occupied traps, for example,

$$p_{\mathrm{t}}^{+} = p_{\mathrm{t}} \times (1 - f_n) \tag{3.11}$$

Here p_t^+ is used for the ionized hole trapping sites and p_t for the total number of hole trapping sites.

The occupational probability depends on capture and emission processes for the traps. We can think of these processes as chemical reactions.

$$p + p_\mathrm{t} \Leftrightarrow p_\mathrm{t}^+ \tag{3.12}$$

$$n + p_\mathrm{t}^+ \Leftrightarrow p_\mathrm{t} \tag{3.13}$$

3.2.4 Capture and emission processes

When a hole moves to a hole trapping site from the valence band, a trapping event is thought to occur. In reality, the electron that exists in this defect in the oxide, is emitted to the valence band under the influence of the electrostatic potential (depending on the activation energy of the trap) and therefore valence band recombination occurs. When a hole that is trapped in a donor defect is emitted in the conduction band, the donor becomes de-ionized (de-trapping). In this case, a free electron from the conduction band is trapped at the positively ionized donor. As it leaves behind the conduction band, this electron does not contribute to conduction current anymore, and therefore a conduction band recombination event is thought to occur. These processes are shown schematically in Figure 3.2

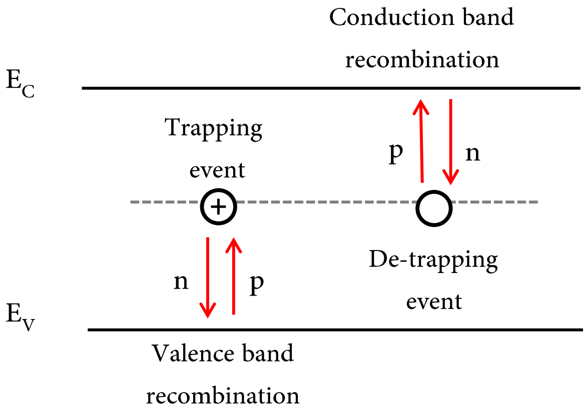

Figure 3.2: Trapping, de-trapping and equivalent recombination events for a hole trap

Traps can also contribute to the creation of electron and hole conduction current. For the case of donor traps, the processes are shown in Figure 3.3.

Trapping and de-trapping with subsequent carrier generation and recombination occurs sequentially until equilibrium is reached. For this reason, carrier capture and emission rates are always added together.

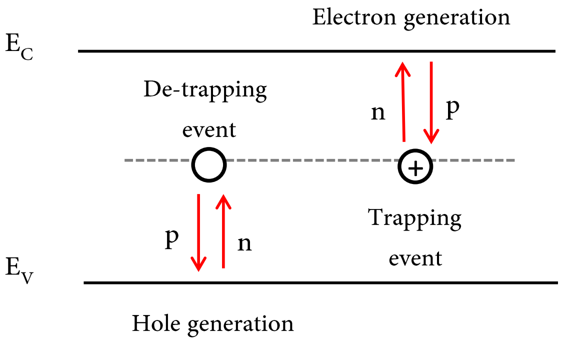

Figure 3.3: Trapping, de-trapping and equivalent carrier generation events for a hole trap

To facilitate further discussion, the capture and emission processes to the conduction and valence bands were given names as shown in Table 3.1. This table also shows the type of process occurring for a donor type of trap.

Process	**Abbreviation**	**Donor trap event**	**Effect on current**
e emission to the CB	e^n_{CB}	Trapping	Electron Generation
e emission to the VB	e^n_{VB}	Trapping	Hole Recombination
h emission to the CB	e^p_{CB}	De-trapping	Electron Recombination
h emission to the VB	e^p_{VB}	De-trapping	Hole Generation
h capture from the CB	c^p_{CB}	Trapping	e^n_{CB}
h capture from the VB	c^p_{VB}	Trapping	e^n_{VB}
e capture from the CB	c^n_{CB}	De-trapping	e^p_{CB}
e capture from the VB	c^n_{VB}	De-trapping	e^p_{VB}

Table 3.1: Capture and emission processes from and to the conduction band (CB) and valence band (VB)

There are four equations describing capture and emission processes

$$c^n_{\text{CB}} = \sigma_n \left[(1 - j_n)\, v^n_{\text{th}} n + j_n \frac{\boldsymbol{J_n}}{q} \right] \tag{3.14}$$

$$c^p_{\text{VB}} = \sigma_p \left[(1 - j_p)\, v^p_{\text{th}} p + j_p \frac{\boldsymbol{J_p}}{q} \right] \tag{3.15}$$

$$e^n_{\text{CB}} = v^n_{\text{th}} \sigma_n \frac{n_1}{g_n} \tag{3.16}$$

$$e^p_{\text{VB}} = v^p_{\text{th}} \sigma_p \frac{p_1}{g_p} \tag{3.17}$$

where $v_{\text{th}}{}^n$ (cm/s) and $v_{\text{th}}{}^p$ (cm/s) are the thermal velocities of electrons and holes respectively, $\sigma_{n,p}$ (cm^2) the capture cross sections of electrons and holes, $g_{n,p}$ is the degeneracy factors of the traps, $\boldsymbol{J_{n,p}}$ are the current densities (A/cm^2) and $j_{n,p}$ are the J-factors for electron and hole traps that show the amount to which the current density of the mobile carriers is responsible for the carrier trapping. For example, with $j_{n,p}$=1, trapping is totally dependent on the current densities of the mobile carriers (full J-model), but with $j_{n,p}$=0, it is the thermal velocities of the carriers that define the amount of trapping (V-model) [86]. It is shown in the experimental capacitor calibration section than only the full drift model leads to physical results.

Finally,

$$n_1 = N_{\mathrm{C}}\mathrm{exp}\left\{\frac{q \times (E_{\mathrm{trap}} - E_{\mathrm{C}})}{kT}\right\} \tag{3.18}$$

$$p_1 = N_{\mathrm{V}}\mathrm{exp}\left\{\frac{q \times (E_{\mathrm{V}} - E_{\mathrm{trap}})}{kT}\right\} \tag{3.19}$$

with $E_{\mathrm{trap}}, E_{\mathrm{C}}, E_{\mathrm{V}}$ the energies of the trap, the conduction and the valence band respectively (eV), N_{C} and N_{V} (cm^{-3}) are the effective densities of states of the conduction and valence bands which are taken from

$$N_{\mathrm{C}} = 2\left(\frac{2\pi m_{\mathrm{e}}kT}{h^2}\right)^{\frac{3}{2}} 10^{-6} \tag{3.20}$$

$$N_{\mathrm{V}} = 2\left(\frac{2\pi m_{\mathrm{p}}kT}{h^2}\right)^{\frac{3}{2}} 10^{-6} \tag{3.21}$$

with m_{e}=0.5m_0 and m_{p}=7.0m_0 [90].

3.2.5 Trapping rate

The trapping rate for a hole trap is defined as follows,

$$\frac{\mathrm{d}p_{\mathrm{t}}^{+}}{\mathrm{d}t} = p_{\mathrm{t}}\left[(1 - f_{\mathrm{p}})\left(c_{\mathrm{VB}}^{p} - e_{\mathrm{CB}}^{n}\right) - f_p\left(e_{\mathrm{VB}}^{p} - c_{\mathrm{CB}}^{n}\right)\right] \tag{3.22}$$

That is, the percentage of occupied traps times the rates of the events that make the traps empty (emission of a hole and capture of a hole) and the remaining unoccupied traps times the capture events. Substituting we get,

$$\begin{aligned}\frac{\mathrm{d}p_{\mathrm{t}}^{+}/\mathrm{d}t}{p_{\mathrm{t}}} = (1-f_p)&\left\{\sigma_p\left[(1-j_p)\,v_{\mathrm{th}}^{p}p + j_p\frac{\boldsymbol{J_p}}{q}\right] - v_{\mathrm{th}}^{n}\sigma_n n_1\right\}\\ -f_p&\left\{v_{\mathrm{th}}^{p}\sigma_p p_1 - \sigma_n\left[(1-j_n)\,v_{\mathrm{th}}^{n}n + j_n\frac{\boldsymbol{J_n}}{q}\right]\right\}\end{aligned} \tag{3.23}$$

3.2.6 Occupational Probability

3.2.6.1 Transient

Going back to the occupational probability of a trap and taking hole occupation as an example, the capture and emission rates contribute as follows,

$$\frac{\partial f^p}{\partial \mathrm{t}} = \sum_i r_i^p \tag{3.24}$$

where the sum is for all capture and emission events [10], and therefore,

$$r_i^p = (1-f^p)\,c_i^p - f^p e_i^p \tag{3.25}$$

Using the superposition principle,

$$\frac{\partial f^p}{\partial t} = (1-f^p)\sum_i c_i^p - f^p\sum_i e_i^p \tag{3.26}$$

Expanding the sums,

$$\frac{\partial f^p}{\partial t} = (1-f^p)\left(c_{\mathrm{CB}}^p + c_{\mathrm{VB}}^p\right) - f^p\left(e_{\mathrm{CB}}^p + e_{\mathrm{VB}}^p\right) \tag{3.27}$$

Using the equivalence of processes,

$$\frac{\partial f^p}{\partial t} = (1-f^p)\left(e_{\mathrm{CB}}^n + c_{\mathrm{VB}}^p\right) - f^p\left(c_{\mathrm{CB}}^n + e_{\mathrm{VB}}^p\right) \tag{3.28}$$

where the emission processes from left to right are as follows: (a) Electron generation, (b) Hole recombination, (c) Electron recombination, (d) Hole generation.

Using Equations 3.14-3.17 and re-arranging we have,

$$\frac{\partial f^p}{\partial t} + f^p \left\{ v_{\text{th}}^n \sigma_n \frac{n_1}{g_n} + \sigma_n \left[(1-j_n)\, v_{\text{th}}^n n + j_n \frac{\boldsymbol{J_n}}{q} \right] + v_{\text{th}}^p \sigma_p \frac{p_1}{g_p} + \sigma_p \left[(1-j_p)\, v_{\text{th}}^p p + j_p \frac{\boldsymbol{J_p}}{q} \right] \right\} = v_{\text{th}}^n \sigma_n \frac{n_1}{g_n} + \sigma_p \left[(1-j_p)\, v_{\text{th}}^p p + j_p \frac{\boldsymbol{J_p}}{q} \right] \tag{3.29}$$

3.2.6.2 Quasistationary

For the quasi-stationary case, we solve Equation 3.24 for t=∞,

$$f^p = \frac{\sum_i c_i^p}{\sum_i \left(c_i^p + e_i^p\right)} \tag{3.30}$$

$$f^p = \frac{c_{\text{CB}}^p + c_{\text{VB}}^p}{\left(c_{\text{CB}}^p + e_{\text{CB}}^p\right) + \left(c_{\text{VB}}^p + e_{\text{VB}}^p\right)} \tag{3.31}$$

Again, using the equivalence of processes we have,

$$f^p = \frac{e_{\text{CB}}^n + c_{\text{VB}}^p}{\left(e_{\text{CB}}^n + c_{\text{CB}}^n\right) + \left(c_{\text{VB}}^p + e_{\text{VB}}^p\right)} \tag{3.32}$$

and substituting,

$$f^p = \frac{v_{\text{th}}^n \sigma_n \frac{n_1}{g_n} + \sigma_p \left[(1-j_p)\, v_{\text{th}}^p p + j_p \frac{\boldsymbol{J_p}}{q} \right]}{\left\{ v_{\text{th}}^n \sigma_n \frac{n_1}{g_n} + \sigma_n \left[(1-j_n)\, v_{\text{th}}^n n + j_n \frac{\boldsymbol{J_n}}{q} \right] \right\} + \left\{ \sigma_p \left[(1-j_p)\, v_{\text{th}}^p p + j_p \frac{\boldsymbol{J_p}}{q} \right] + v_{\text{th}}^p \sigma_p \frac{p_1}{g_p} \right\}} \tag{3.33}$$

3.2.7 Recombination processes

We can now express the recombination terms for one trapping level as,

$$R_{\text{pt}}^n = p_{\text{t}} \left[(1-f_p)\, c_{\text{CB}}^n - f_p e_{\text{CB}}^n \right] \tag{3.34}$$

$$R_{\text{pt}}^p = p_{\text{t}} \left[f_p c_{\text{VB}}^p - (1-f_p)\, e_{\text{VB}}^p \right] \tag{3.35}$$

$$R_{\text{pt}}^n = p_t \left\{ (1-f_p)\, \sigma_n \left[(1-j_n)\, v_{\text{th}}^n n + j_n \frac{\boldsymbol{J_n}}{q} \right] - f_p v_{\text{th}}^n \sigma_n n_1 \right\} \tag{3.36}$$

$$R_{\mathrm{pt}}^{p} = p_t \left\{ f_p \sigma_p \left[\left(1 - j_p\right) v_{\mathrm{th}}^{p} p + j_p \frac{\boldsymbol{J_p}}{q} \right] - \left(1 - f_p\right) v_{\mathrm{th}}^{p} \sigma_p p_1 \right\} \tag{3.37}$$

The recombination in steady state is equal for electrons and holes and is the following for SRH,

$$R_{\mathrm{SRH}} = \frac{p_{\mathrm{t}} \left\{ \sigma_n \left[\left(1 - j_n\right) v_{\mathrm{th}}^{n} n + j_n \frac{\boldsymbol{J_n}}{q} \right] \sigma_p \left[\left(1 - j_p\right) v_{\mathrm{th}}^{p} p + j_p \frac{\boldsymbol{J_p}}{q} \right] - v_{\mathrm{th}}^{n} \sigma_n v_{\mathrm{th}}^{p} \sigma_p n_{i,\mathrm{eff}}^{2} \right\}}{v_{\mathrm{th}}^{n} \sigma_n n_1 + \sigma_n \left[\left(1 - j_n\right) v_{\mathrm{th}}^{n} n + j_n \frac{\boldsymbol{J_n}}{q} \right] + v_{\mathrm{th}}^{p} \sigma_p p_1 + \sigma_p \left[\left(1 - j_p\right) v_{\mathrm{th}}^{p} p + j_p \frac{\boldsymbol{J_p}}{q} \right]} \tag{3.38}$$

where $n_{i,\mathrm{eff}}^{2}$ is the effective intrinsic concentration of the oxide.

3.3 Areal charge

Using Poisson's equation, we can calculate the areal trapped charge projected at the Si/SiO$_2$ interface (cm^{-2}) with,

$$_{\mathrm{at}} = \int_0^{t_{\mathrm{ox}}} \frac{x}{t_{\mathrm{ox}}} p_{\mathrm{t}}^{+} \left(x\right) \mathrm{d}x \tag{3.39}$$

where t_{ox} is at the silicon/oxide interface, and t_{ox}-x is the distance from the interface (cm).

3.4 Thermionic emission model

It was observed during simulation tests that proper boundary conditions had to be included in the model to account for accurate transport of the generated carriers out of the oxide. In the literature, the generated carriers are believed to escape to the nearest electrode. While this is true, however, a fraction of them is directed towards the Si/SiO$_2$ interface where electric field discontinuities create unphysical results. Therefore, the boundary conditions of the oxide had to be properly modelled. For this reason, thermionic emission was activated at the Si/SiO$_2$ interface.

The thermionic emission model implementation in Sentaurus device is based on the heterojunction model derived in [91]. The total energy and perpendicular momentum of the electron are conserved. For two materials with conduction band edges $E_{\mathrm{C},1}$ and $E_{\mathrm{C},2}$ and ΔE_{C} = $E_{\mathrm{C},2}$ - $E_{\mathrm{C},1}$ $>$0, the equivalent current densities $\boldsymbol{J_{n,1}}$ and $\boldsymbol{J_{n,2}}$ are set as [92],

$$\boldsymbol{J_{n,2}} = \boldsymbol{J}_{\mathrm{n},1} \tag{3.40}$$

$$\boldsymbol{J_{n,2}} = 2q\left[v_{n,2}n_2 - \frac{m_{n,2}}{m_{n,1}}v_{n,1}n_1\mathrm{exp}\left(-\frac{\Delta E_\mathrm{C}}{kT_{n,1}}\right)\right] \tag{3.41}$$

where $v_{\mathrm{n,i}}$ are the emission velocities,

$$v_{n,i} = \sqrt{\frac{kT_{n,i}}{2\pi m_{n,i}}} \tag{3.42}$$

The electron energy flux density escaping material 1,

$$\boldsymbol{S_{n,2}} = \boldsymbol{S_{n,1}} + \frac{1}{q}\boldsymbol{J_{n,2}}\Delta E_\mathrm{C} \tag{3.43}$$

$$\boldsymbol{S_{n,2}} = -4\left[v_{n,2}n_2kT_{n,2} - \frac{m_{n,2}}{m_{n,1}}v_{n,1}n_1kT_{n,1}\mathrm{exp}\left(-\frac{\Delta E_\mathrm{C}}{kT_{n,1}}\right)\right] \tag{3.44}$$

For holes,

$$\boldsymbol{J_{p,2}} = \boldsymbol{J_{p,1}} \tag{3.45}$$

$$\boldsymbol{J_{p,2}} = -2q\left[v_{p,2}p_2 - \frac{m_{p,2}}{m_{p,1}}v_{p,1}p_1\mathrm{exp}\left(\frac{\Delta E_\mathrm{V}}{kT_{p,1}}\right)\right] \tag{3.46}$$

$$\boldsymbol{S_{p,2}} = \boldsymbol{S_{p,1}} + \frac{1}{q}\boldsymbol{J_{p,2}}\Delta E_\mathrm{V} \tag{3.47}$$

$$\boldsymbol{S_{p,2}} = -4\left[v_{p,2}p_2kT_{p,2} - \frac{m_{p,2}}{m_{p,1}}v_{p,1}n_1kT_{p,1}\mathrm{exp}\left(\frac{\Delta E_\mathrm{V}}{kT_{p,1}}\right)\right] \tag{3.48}$$

and

$$v_{p,i} = \sqrt{\frac{kT_{p,i}}{2\pi m_{p,i}}} \tag{3.49}$$

m_n and m_p are calculated from the effective conduction and valence band DOS using,

$$\frac{m_{\mathrm{n}}}{m_0} = \left(\frac{N_{\mathrm{C}}}{2.5094 \times 10^{19}}\right)^{2/3} \tag{3.50}$$

$$\frac{m_{\mathrm{p}}}{m_0} = \left(\frac{N_{\mathrm{V}}}{2.5094 \times 10^{19}}\right)^{2/3} \tag{3.51}$$

3.5 Hydrogen transport

Transport of hydrogen species is modelled using the following equation,

$$\frac{\partial}{\partial t}\left[X_i\right] + \boldsymbol{\nabla}\cdot \left[D_{\mathrm{iexp}}\left(-\frac{E_{\mathrm{di}}}{kT}\right)\left(\frac{q}{kT}E\left[X_i\right] - \boldsymbol{\nabla}X_i - \alpha_{\mathrm{td}}X_i\boldsymbol{\nabla}\ln T\right)\right] + R_{\mathrm{net}} = 0 \tag{3.52}$$

X_i is the density of the hydrogen species (cm^{-3}). Hydrogen species used are atomic hydrogen (H), hydrogen molecule (H_2), hydrogen ion (H^+). D_i is the diffusion coefficient (cm^2/s), E_{di} is the diffusion activation energy (eV), α_{td} the prefactor for thermal diffusion term, R_{net} is the net recombination term due to chemical reactions (cm^{-3}s^{-1}).

3.6 State Transitions

Multistate configurations (MSC) in Sentaurus device are defined by a number of states, N, and their occupation probabilities s_1,...,s_N for which,

$$\sum_i s_i = 1 \tag{3.53}$$

holds. The following equation relates the state occupational probability with capture and emission rates of the transitions involved in the MSC.

$$\dot{s}_i = \sum_{j\neq i}\sum_{t\in T_{ij}} c_{ij}s_j - e_{ij}s_i \tag{3.54}$$

Each transition involves two states, i and j, where i is the 'to' state and j is the 'from' state. T_{ij} is the set of transitions between i and j. The following holds for the capture and emission rates (c and e) of each transition,

$$c = c_{ij} = e_{ji} \text{ , } e = e_{ij} = c_{ji}$$

The inner energy of the state is given by,

$$H_i = E_i + K_i^- E_i^- \tag{3.55}$$

where E_i is the base energy, K_i^- is the number of the negative elementary charges and E_i^- the energy of one electron in the state.

In equilibrium, the occupational probability of the state is determined by,

$$s_i^* = Z_i / Z \tag{3.56}$$

$$Z = \sum_i Z_i \tag{3.57}$$

$$Z_i = g_i \mathrm{exp}\left(-\beta\left(H_i - K_i^- E_\mathrm{F}\right)\right) \tag{3.58}$$

where g_i is the degeneracy factor, β is the thermodynamic 1/kT and E_F is the quasi-Fermi energy. The latter is approximated inside the code used for the MSC, as follows. The intrinsic carrier density is defined by,

$$n_\mathrm{I} = \sqrt{N_\mathrm{C} N_\mathrm{V} \mathrm{exp}\left(-\beta E_g\right)} \tag{3.59}$$

and the intrinsic Fermi energy,

$$E_\mathrm{I} = \frac{1}{2}\left[\left(E_\mathrm{C} + E_\mathrm{V}\right) + kT\mathrm{ln}\left(\frac{N_\mathrm{V}}{N_\mathrm{C}}\right)\right] \tag{3.60}$$

The carrier quasi-Fermi energies are approximated with,

$$E_{\mathrm{F},n} = E_\mathrm{I} + kT\mathrm{ln}\left(\frac{n}{n_\mathrm{I}}\right) \tag{3.61}$$

$$E_{\mathrm{F},p} = E_\mathrm{I} - kT\mathrm{ln}\left(\frac{p}{n_\mathrm{I}}\right) \tag{3.62}$$

and the equilibrium Fermi energy with,

$$E_\mathrm{F} = \frac{1}{2}\left(E_{\mathrm{F},n} + E_{\mathrm{F},p}\right) \tag{3.63}$$

In this work, the Arrhenius law is used to describe capture at dangling bonds and formation or annealing of an interface state. Specifically, the capture rate is,

$$c = r_0 \mathrm{exp}\left(-\beta E_{\mathrm{act}}\right) \tag{3.64}$$

with r_0, the maximal transition frequency and E_{act} the activation energy. The emission rate is computed from,

$$e = \frac{s_j^*}{s_i^*} c \tag{3.65}$$

After the interface states are de-passivated, the capture rate is described using a simple trapping model,

$$c = \sigma v_{\mathrm{th}} d_{\mathrm{c}} \tag{3.66}$$

where σ is the capture cross section (cm^2), d_{c} is the carrier density (cm^{-3}) and v_{th} is the thermal velocity of the carrier. The emission rate is computed from,

$$\frac{e}{c} = \left[g_{ji}\mathrm{exp}\left(-N_n\beta_n\left(E_{\mathrm{F},n} - \overline{E_{\mathrm{C}}}\right) + N_p\beta_p\left(E_{\mathrm{F},p} - \overline{E_{\mathrm{V}}}\right) + \beta_{\mathrm{l}}\left(-N_n\overline{E_{\mathrm{C}}} + N_p\overline{E_{\mathrm{V}}} - H_{ji}\right)\right)\right] \tag{3.67}$$

where $\mathrm{g}_{\mathrm{ji}}=\mathrm{g}_{\mathrm{j}}/\mathrm{g}_{\mathrm{i}}$ and H_{ji} = H_{j} - H_{i}. The average conduction and valence band energies, $\overline{E_{\mathrm{C}}}$ and $\overline{E_{\mathrm{V}}}$ are given from,

$$\overline{E_{\mathrm{C}}} = E_{\mathrm{C}} + \tfrac{3}{2}kT_n \text{ and } \overline{E_{\mathrm{V}}} = E_{\mathrm{V}} - \tfrac{3}{2}kT_p$$

3.7 Random Dopant Fluctuations

3.7.1 Sano method

Random Dopant Fluctuations (RDFs) can be simulated by using a randomly non-uniform concentration of the dopant atoms in the active silicon region. To achieve this we use the Sano method in Sentaurus mesh. This method solves the problem of singularities arising in Drift-Diffusion simulators when the mean distance of the discrete dopants is bigger than the size of the mesh elements. The singularities result due to the very high electrostatic potential difference between adjacent mesh elements when an atom occupies one single element. Experiments have shown that the charge distribution can be thought to be averaged out in deep sub-micron devices because part of the Coulomb potential of the dopants is lost in scattering mechanisms [93].

Therefore, to properly represent the potential of discrete dopants in relatively 'coarse' meshes when comparing to the mean distance between them, the Coulomb potential of the dopant atoms is divided in long and short range parts and only the long range part is kept. To achieve that, we use the screening factor k_c defined as the inverse of the screening length for a discrete dopant atom. The choice of this parameter should be such that the charge density from the dopants felt by the carriers is that acting upon their drift motion and not on scatterings. One idea is to use the Conwell-Weisskopf model for this parameter,

$$k_\mathrm{c} \approx 2 \times N_\mathrm{ac}^{1/3} \tag{3.68}$$

Where N_ac is the acceptor density used for macroscopic simulations (cm^{-3}). In [93], the screening factor is a fitting parameter fine-tuned so as the results from longer channel devices matched the characteristics of those with shorter channel. The applicability of the Conwell-Weisskopf model is test in Section 5.4.1.

Using the parameter k_c, and the long range part of the Coulomb potential, the charge density is given by,

$$n\left(r\right) = N_\mathrm{f} \frac{k_\mathrm{c}^3}{2\pi^2} \frac{\sin\left(k_\mathrm{c} r\right) - \left(k_\mathrm{c} r\right)\cos\left(k_\mathrm{c} r\right)}{\left(k_\mathrm{c} r\right)^3} \tag{3.69}$$

where N_f is a normalization factor such that the integral of $n\left(r\right)$ over the entire simulation space becomes unity and r is the distance from the discrete dopant [94].

The normalized long-range number density as a function of distance from the dopant location is shown in Figure 3.4. This oscillatory function is cut off at the first occurrence of zero in Sentaurus mesh. Therefore, for k_c=3.3×10^6 cm^{-1}, the relationship between n and r becomes as shown in Figure 3.5. The exact number density at the element where the discrete dopant is located will be defined by the normalization factor. The number density function in piecewise form is as follows:

$$n\left(r\right) = \begin{cases} N_\mathrm{f} \frac{k_\mathrm{c}^3}{2\pi^2} \frac{\sin(k_\mathrm{c} r) - (k_\mathrm{c} r)\cos(k_\mathrm{c} r)}{(k_\mathrm{c} r)^3}, & \text{if } k_\mathrm{c} r < 4.4934 \\ 0, & \text{if } k_\mathrm{c} r > 4.4934 \end{cases} \tag{3.70}$$

The derivation of this equation can be found in Appendix B.

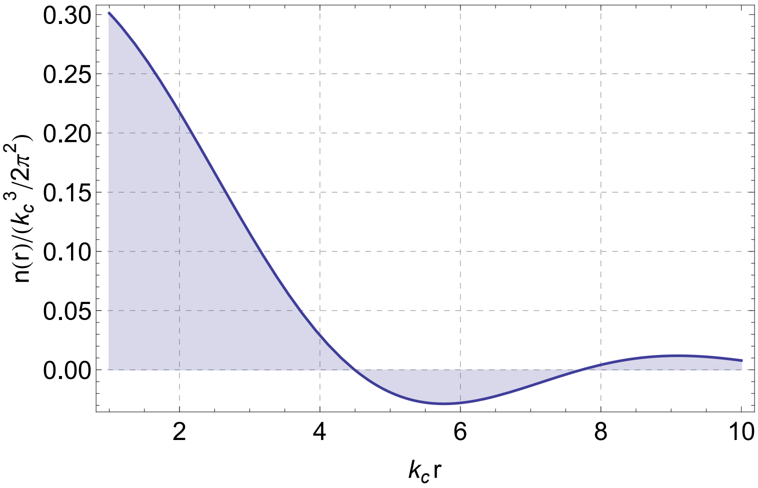

Figure 3.4: Normalized long-range number density of a discrete dopant

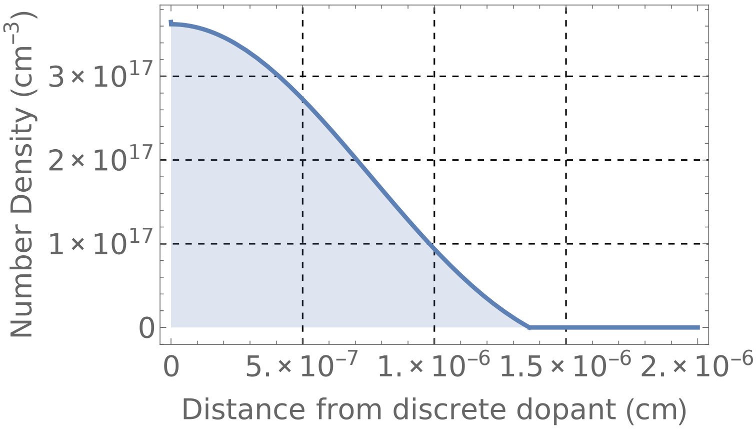

Figure 3.5: Doping number density as a function of distance from the point of location of the atom. The normalization factor used in this figure is 0.59688 [94]

3.7.2 Impedance Field Method

The Impedance Field Method (IFM) in Sentaurus device can be used to examine variations in devices from different sources, including RDFs. This method does not include converting the doping profile to an atomistic. Instead, it uses only one solution to a reference device, and then calculates the effect of the variation as a linear response to a perturbation of the contact current or voltage.

There are two types of IFM implemented in Sentaurus device that can be used for examination of RDFs: The noise IFM which produces current and voltage spectral densities of the results and the statistical IFM which produces a large number of randomized variations of the doping profiles and computes the modification of the device characteristics in linear response. In this work, the statistical IFM is used to produce the full I-V results of the devices and compare them with those of the Sano method.

The Green's function is solved once, for the reference device, for each contact. For the case of contact current, the perturbation due to RDFs at location x and angular frequency ω will result in contact current response [10],

$$\delta I_c = \int G(x,\omega)\,\delta N_\xi(x,\omega)\,dx \tag{3.71}$$

where c is the contact node, $G(x,\omega)$ is Green's function and N_ξ is the equation that involves the doping concentration term. The angular frequency, ω, is used for the noise-like IFM, but is zero for the statistical IFM used in this study [95, 96].

Using a Poisson distribution, the probability to find k dopant atoms in a box volume $\mathrm{V_i}$ with average doping concentration $\mathrm{N_i}$ at a vertex i of the mesh,

$$P_i(k) = \frac{(N_i V_i)^k}{k!}\exp(-N_\mathrm{i} V_\mathrm{i}) \tag{3.72}$$

the dopant atom in this equation can be either an acceptor or a donor. Sentaurus device calculates the response due to either acceptor or donor atom fluctuations. In the cases where both are examined (as is performed in this work), the two sources of variation are considered to be uncorrelated [10].

3.8 Overview

The theoretical aspects and simulation models used in this work have been discussed. Basic concepts of the FEM were presented. This method is used to solve the rate equations governing device operation. Charge trapping equations were explained and the capture/emission processes in donor traps have been described in detail. These equations are solved self-consistently with the Poisson equation in simulations hereafter. The thermionic emission model, essential to the simulation method developed here, was also explained. Charge generation, transport and trapping equations are used in this work to describe TID effects in the oxides, and are therefore solved in the corresponding regions. State transition equations using an Arrhenius law for passivation and de-passivation of interface states and a simple trapping model for electron/hole capture in the de-passivated states have been presented. Hydrogen species play a dominant role in the interface trap formation. The diffusive transport model used for this purpose was also given in this chapter. Lastly, the two models used to simulate RDF effects were presented. This includes the Sano method and the long-range Coulomb potential equation as well as the contact current perturbation and dopant Poisson distribution in the mesh elements when using the IFM.

Chapter 4

Simulation and calibration of 400 nm SiO_2 capacitors

Thick field isolation is widely used today as a Buried OXide (BOX) in Silicon-on-Insulator technologies [97], a Shallow Trench Isolation separating devices in single and multi-gate technologies [98] and it is also commonly found in 2D semiconductor transistors such as graphene and MoS_2 [99–101]. These oxides are the main contributing factor to Total Ionizing Dose (TID) effects of deep sub-micron technologies, contrary to the thin gate oxides where trapped charges are able to tunnel out under the influence of the electric field [19].

In this work, thick oxide capacitors with 400 nm SiO_2 were fabricated at the University of Southampton and subsequently irradiated at Cranfield University using Co^{60} [102]. These experimental results were used to calibrate the simulation model from which the model parameters were extracted and used in the transistor simulations. The area of the capacitors is 316 × 316 μm. The two samples were irradiated at different doses: 11.6 krad(SiO_2) for sample A and 58 krad(SiO_2) for sample B.

The pre- and post- irradiation transfer characteristics were simulated in Synopsys device. The simulations were performed on the Iridis supercomputer at the University of Southampton. The simulation times and threads used varied for each experiment. The maximum time for running one simulation was 60 hrs. The maximum number of processors used simultaneously was 16 and the maximum number of threads 32.

4.1 Capacitor pre-irradiation simulations

The experimental pre- and post-irradiation results of two capacitor samples used further in this work are shown in Figure 4.2. Increased capacitance in the inversion region can occur when the frequency of the AC signal during measurements is lower than the time required for equilibration of the mobile charges through drift and diffusion processes. In this case, however, the AC signal is 1 MHz, which is usually high enough to prevent accumulation of charges in the depletion region. Another case where such a situation has been observed was explained by a lateral AC current flow, whose area extends beyond the metallic plate of the gate in combination with surface states at the Si/SiO$_2$ interface [102, 103]. Namely, carriers that have been trapped at interface states away from the metal electrode, create a lateral current when de-trapped as the capacitor bias changes. The midgap voltage shift is extracted using sdevice in section 4.3.3. Here, we note that the voltage shift at C = 7 pF is ΔV = -1.38 V for sample A and ΔV = -3.04 V for sample B.

The pre-irradiation experimental results were used to calibrate initial parameters. The 2D capacitor simulation model is shown in Figure 4.1. The doping concentration used is $N_\mathrm{a} = 6.4\times10^{14}$ cm^{-3}, as extracted in [102]. The oxide thickness was determined to be 390 nm in agreement with C_max.

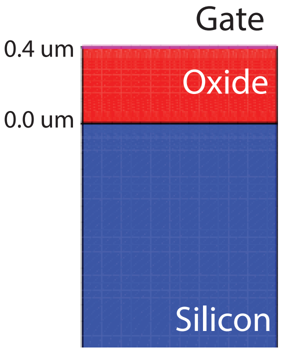

Figure 4.1: Capacitor 2D simulation structure

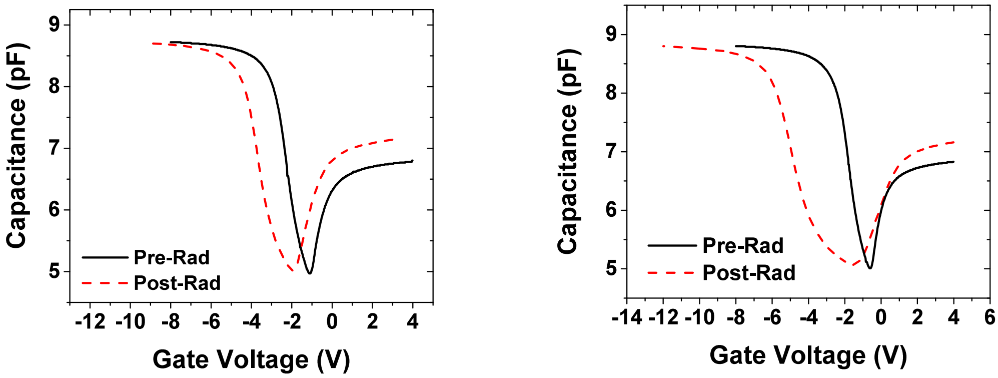

(a) Sample A (b) Sample B

Figure 4.2: Pre- and post-irradiation experimental C-V results of 400 nm SiO$_2$ capacitors

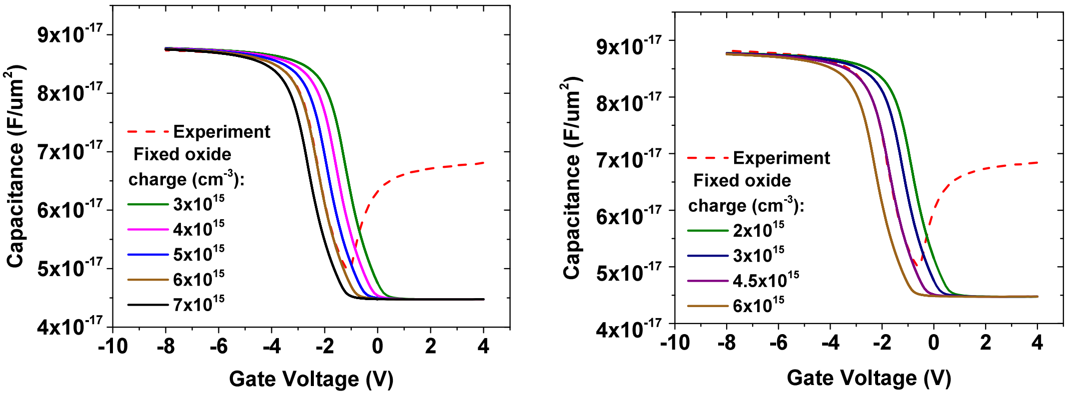

(a) Sample A

(b) Sample B

Figure 4.3: C-V characteristics with different fixed oxide charge

Fixed oxide charge, N_{ot} (cm^{-3}), was also introduced to fit the midgap voltage to the experiment. The C-V results of the simulations of the two samples with different amount of fixed oxide charges in comparison to the experimental pre-rad results are shown in Figure 4.3. For Sample A, $N_{\text{ot}} = 6 \times 10^{15}$ cm^{-3} and for Sample B, $N_{\text{ot}} = 4.5 \times 10^{15}$ cm^{-3}.

Physically, the current flowing through an interface of a metal with a semiconductor is non-linear in nature and dependent on the electronic states existing on this interface. The discontinuity present due to the difference in the Fermi level of the two materials is translated to a barrier height with rectifying characteristics [104]. In the present capacitor model, a Schottky metal/oxide contact with workfunction of 4.28 eV was used. The Schottky contact prevented voltage shifts when different amount of traps were defined in the oxide by fixing the electrostatic potential difference in the oxide to a value relative to the barrier height between the metal and silicon. For an Ohmic contact, charge neutrality and equilibrium is assumed,

$$n_{i,\text{eff}}^2 = n_0 p_0 \quad , \quad n_0 - p_0 = N_{\text{D}} - N_{\text{A}}, \tag{4.1}$$

where n_0 and p_0 are the electron and hole equilibrium concentrations respectively (cm^{-3}). And the electrostatic potential for Boltzman statistics is given by,

$$\phi = \phi_{\text{F}} + \frac{kT}{q} \text{asinh} \left(\frac{N_{\text{D}} - N_{\text{A}}}{2 n_{i,\text{eff}}} \right) \tag{4.2}$$

where ϕ_{F} is the Fermi potential at the contact, which equals the voltage applied.

For a Schottky contact, charge neutrality on the two sides of the interface does not hold, and the following boundary conditions are applied,

$$n_0^{\mathrm{B}} = N_{\mathrm{C}}\exp\left(\frac{-q\Phi_{\mathrm{B}}}{kT}\right) \quad , \quad p_0^{\mathrm{B}} = N_{\mathrm{V}}\exp\left(\frac{-E_{\mathrm{g}}+q\Phi_{\mathrm{B}}}{kT}\right) \tag{4.3}$$

$$\boldsymbol{J_n}\cdot\widehat{n} = qv_{\mathrm{th}}^{n}\left(n-n_0^{\mathrm{B}}\right) \quad , \quad \boldsymbol{J_p}\cdot\widehat{n} = -qv_{\mathrm{th}}^{p}\left(p-p_0^{\mathrm{B}}\right) \tag{4.4}$$

$$\phi = \phi_{\mathrm{F}} - \Phi_{\mathrm{B}} + \frac{kT}{q}ln\left(\frac{N_{\mathrm{C}}}{n_{i,\mathrm{eff}}}\right) \tag{4.5}$$

where Φ_{B} is the barrier height of the Schottky contact defined as the difference between the contact workfunction and the calculated electron affinity of SiO$_2$, E_{g} is the SiO$_2$ bandgap, $\widehat{n}$ is the unit vector normal to the interface and n_0^{B} and p_0^{B} are the equilibrium carrier densities.

The midgap voltage shifts induced with the Ohmic metal/oxide contact with different p_{t} concentrations can be seen in Figure 4.4(a). The charge equilibrium conditions on the two sides of the interface produce equivalent ${p_{\mathrm{t}}}^{+}$ densities that create voltage shifts. The electric field in the capacitor oxide in the direction from the metal to the silicon is shown in Figure 4.4(b). It can be seen that, for the gate voltage examined, the simulation model with the oxide defined as dielectric (OAD) and the oxide defined as a semiconductor (OASC) and a Schottky metal/oxide contact, the two values are in agreement. This is also true for the conduction band edge as seen in Figure 4.5.

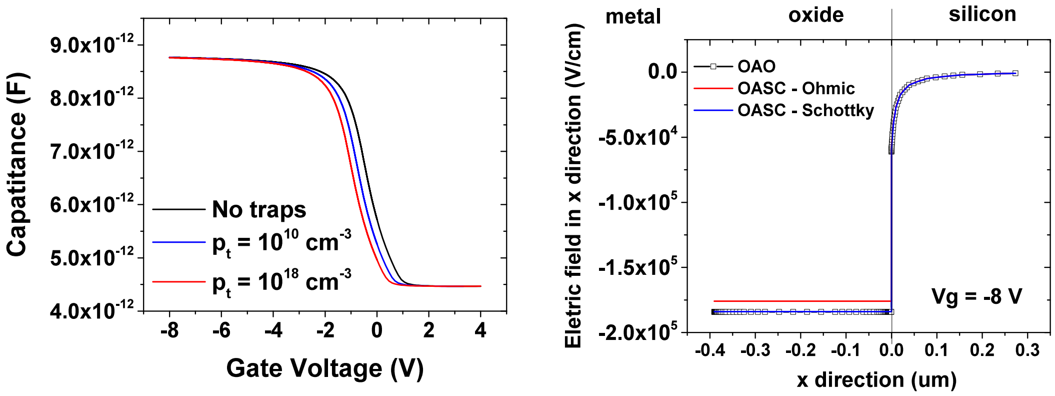

(a) C-V characteristics with Ohmic metal/oxide contact and different oxide trap concentrations

(b) Electric field in the x direction of the structure for the cases of oxide as dielectric (OAD), oxide as semiconductor (OASC) with Ohmic and Schottky contact with the metal. V_{g}=-8 V.

Figure 4.4: Comparison of device characteristics with Schottky and Ohmic contact

Thermionic emission was enabled at the silicon/oxide interface to prevent convergence issues that were caused by the high density of holes trapped at the interface due to the abrupt change in electrostatic potential. Physically, thermionic emission of the carriers produced is thought to occur during irradiation.

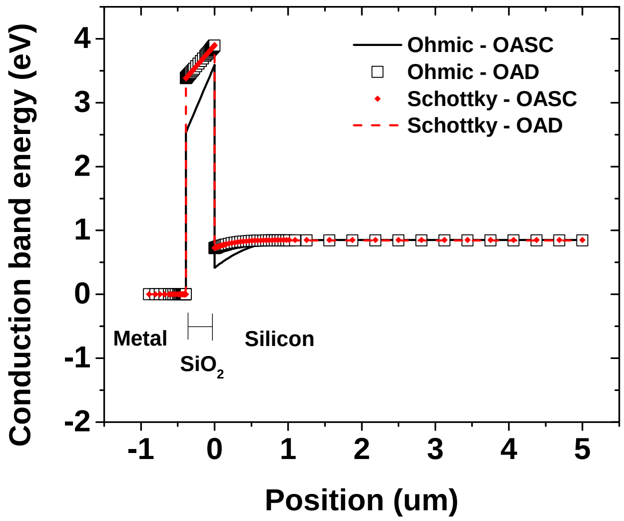

Figure 4.5: Band diagrams of oxide as dielectric (OAD) and oxide as semiconductor (OASC) with Schottky and Ohmic contact. $V_g = 0$ V.

4.2 Post-irradiation parameters

4.2.1 Hole yield and dose rate

The hole yield in Equation 3.3 was fitted to the experimental results from Schwank et al. [105] as shown in Figure 4.6. The values of the parameters are shown in Table 4.1.

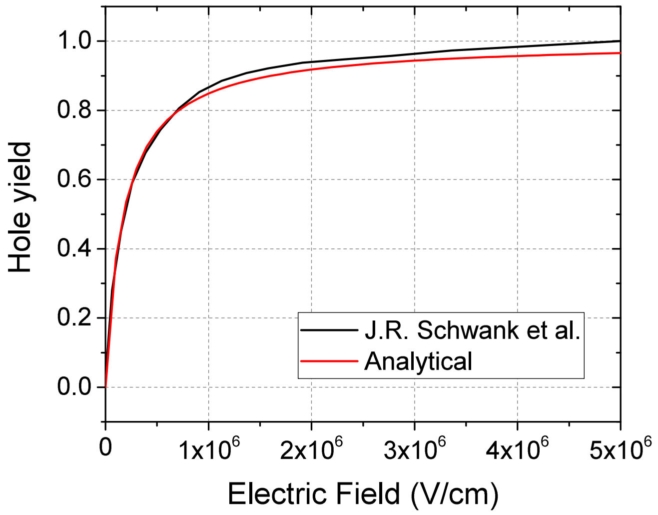

Figure 4.6: Hole yield as a function of Electric field. The black line is taken from the literature for Co^{60} [25]. The red line is the fitted hole yield. The parameters used in Equation 3.3 are shown in Table 4.1.

The fabricated capacitors were irradiated at $\dot{D}$=240 kRad(Si)/h = 67 Rad(Si)/s. The conversion factor used is 1 Rad(Si) = 0.58 Rad(SiO$_2$) [106]. The final dose rate used in the simulations is 38.6 Rad(SiO$_2$)/s. This dose rate was also used in setting up the environment for the subsequent simulations.

Parameter	Description	Value	Units
E_1	Fitting Parameter	0.1	V/cm
E_2	Fitting Parameter	2×10^5	V/cm
m	Fitting Parameter	0.9	
g	Irradiation Term	$7.6\cdot10^{12}$	cm^{-3} Rad(SiO$_2$)
$\dot{D}$	Dose Rate	38.6	Rad(SiO$_2$)/s

Table 4.1: Parameters used for hole yield

4.2.2 Carrier transport

The parameters used for carrier transport are shown in Table 4.2. The mobility values of electrons are extracted are in accordance to [76].

	Symbol	Value	Units
Electron Mobility	μ_n	20	cm^2 V^{-1} s^{-1}
Hole Mobility	μ_p	10^{-5}	cm^2 V^{-1} s^{-1}
SiO$_2$ bandgap	E_g	9	eV
SiO$_2$ electron affinity	χ	0.9	eV

Table 4.2: Parameters used for the constant mobility model in sdevice

The density of states (DOS) in SiO$_2$ can take a wide range of values, depending on the fabrication process, the thickness of the oxide as well as the position inside it. Theoretical studies of the effective masses of electrons and holes in the conduction and valence bands for different modifications of the SiO$_2$ crystal structure have been performed. In [90], it was found that amorphous SiO$_2$ has similar structure to $\alpha-$ SiO$_2$ and that in the latter there exists an isotropic electron effective mass tensor with $m_e^*=0.5m_0$, and an anisotropic hole effective mass with m_{lh}=1.3m$_0$ and m_{hh}=7.0m_0.

Using Equation 3.20, the effective conduction band DOS for m_e^*=0.5m_0 is N_C = 8.867×10^{18} cm^{-3}. Using Boltzmann statistics, the intrinsic carrier density is,

$$n_i = \sqrt{N_C N_V} \exp\left[-\frac{E_g q}{2kT}\right] \tag{4.6}$$

For a range of N_V values between 5.0×10^{17} cm^{-3} and 5.0×10^{20} cm^{-3}, n$_i$ shows negligible change (Figure 4.7),

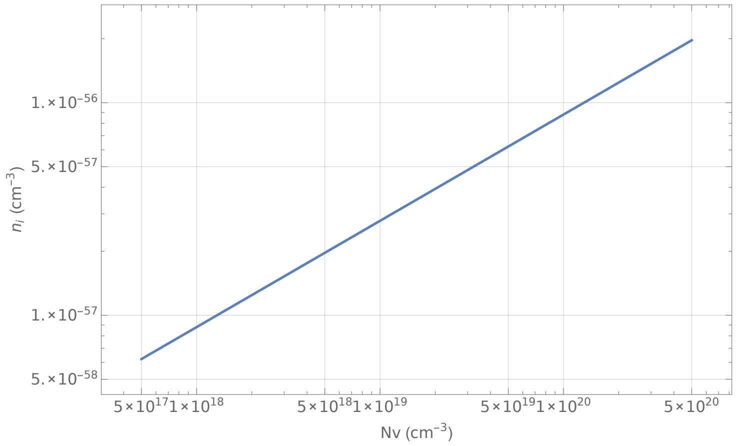

Figure 4.7: Intrinsic carrier density in SiO$_2$ as a function of valence band effective DOS, using Boltzmann statistics N_C = 8.867×10^{18} cm^{-3}

In our simulations, as a rule, N_V = 1.931×10^{20} cm^{-3} derived from,

$$m_\mathrm{h}^* = (m_\mathrm{lh} m_\mathrm{hh} m_\mathrm{hh})^{1/3} = 3.9 m_0 \tag{4.7}$$

However, it was observed that in some cases N_V >10^{20} cm^{-3} affected convergence and this was taken into consideration.

4.2.3 Numerical check of solution in the oxide

The use of the oxide as a semiconducting structure and subsequent solution of the transport equations in it has created differences to the usual solution of the device. In this chapter, we perform numerical checks against solutions of the equations at one point in the oxide.

A 2D test structure of dimensions 400x1000 nm was prepared. It consists entirely of an oxide region that is treated as semiconductor, with the band-gap parameters of SiO$_2$. Two electrodes are connected on the two sides of the oxide as shown in Figure 4.8. The direction from the top to the bottom electrode is defined as the x direction, whereas the direction perpendicular to it, is defined as the Y direction. The structure details are shown in Table 4.3.

Dimensions	400 nm × 1μm
Contacts	Schottky
Mesh Density(x,y)	(5-10 nm, 10 nm)

Table 4.3: Parameters for the 2D oxide region

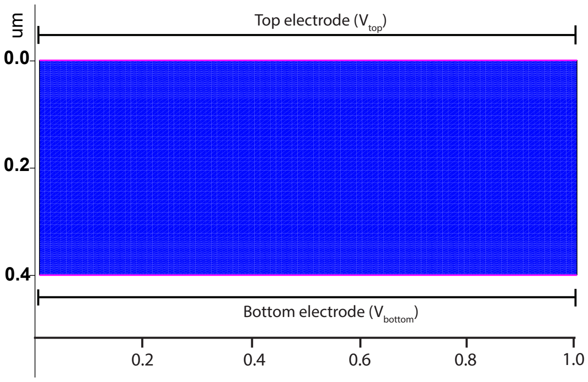

Figure 4.8: 2D structure used as a test structure. Top electrode and bottom electrode are shown. X direction is from top towards bottom electrode, Y direction is taken to be parallel to the electrodes (left to right).

Step-by-step the numerical checks for the TID process are: (a) Irradiation, (b) Carrier transport and (c) Hole trapping.

4.2.4 Carrier generation

The radiation generation was tested using Equation 3.1.

Location (x,y) (μ m)	Simulator Absolute El. Field (V/cm)	Simulator G_{ehp} ($cm^{-3}s^{-1}$)	Calculated G_{ehp} ($cm^{-3}s^{-1}$)
(0.20,0.50)	384.231	1.0498×10^{12}	1.051×10^{12}

Table 4.4: Calculated values for electron-hole pair generation with given values of Electric Field

Table 4.4 shows that the electron-hole pair generation rate calculated closely matches the simulated value at location X = 0.2 μm, Y = 0.5 μm in the test structure.

4.2.5 Transport in quasistationary

The bandgap parameters and mobility values of this oxide structure are shown in Table 4.2. Classical drift-diffusion was chosen and constant mobility. These values were taken from [76].

The electron and hole fluxes for the quasi-stationary case with Dose Rate = 38.6 Rad (SiO_2)/s at V_{top} = 1.1 V are shown in Figure 4.9. The electron flux is higher at V_{top}, due to the positive bias. Likewise the hole flux is higher at V_{bottom}. The flux in the Y direction remains constant.

The rate of change of the electron and hole current densities in the X and Y direction are shown in Figure 4.10. Due to carrier equilibrium, both and carrier flux and the rate of change of the current density are symmetrical between the electrons and holes. The rate of change in the X direction follows the slope of the current flux in Figure 4.9(a). Namely, as X increases, the electron flux decreases and its derivative is negative. Equivalently, the hole flux increases with X and its derivative is positive.

Position(x,y)	(0.34922,0.5) µm	
d$\boldsymbol{J_p}$/qdx	4.390×10^{13}	cm^{-3}s^{-1}
d$\boldsymbol{J_p}$/qdy	0	cm^{-3}s^{-1}
d$\boldsymbol{J_n}$/qdx	-4.391×10^{13}	cm^{-3}s^{-1}
d$\boldsymbol{J_n}$/qdy	0	cm^{-3}s^{-1}
G$_{\text{ehp}}$	4.385×10^{13}	cm^{-3}s^{-1}
R$_{\text{SRH}}$	3.246×10^{9}	cm^{-3}s^{-1}

Table 4.5: Simulator output for current continuity in quasistationary simulation of the test structure

The simulator output for checking proper operation of the continuity equations is shown in Table 4.5. The numbers match Equations 3.9 and 3.10, which for two dimensions, become:

$$-\left(\frac{\partial \boldsymbol{J_p}}{q\partial x}+\frac{\partial \boldsymbol{J_p}}{q\partial y}\right)+G_{\text{ehp}}-R_{\text{SRH}}=0 \tag{4.8}$$

$$\left(\frac{\partial \boldsymbol{J_n}}{q\partial x}+\frac{\partial \boldsymbol{J_n}}{q\partial y}\right)+G_{\text{ehp}}-R_{\text{SRH}}=0 \tag{4.9}$$

The electron flux through the contacts during the quasi-stationary simulation of the test structure is shown in Figure 4.11. The current going through the top electrode at V$_{\text{top}}$ = 1.1 V is equal to that at the top electrode in Figure 4.9(a). For this, we are taking into accout that the current at the contacts is calculated as the surface integral of the current density over the contact area (DirectCurrent in sdevice [10]). The contact area is 1 µm^2.

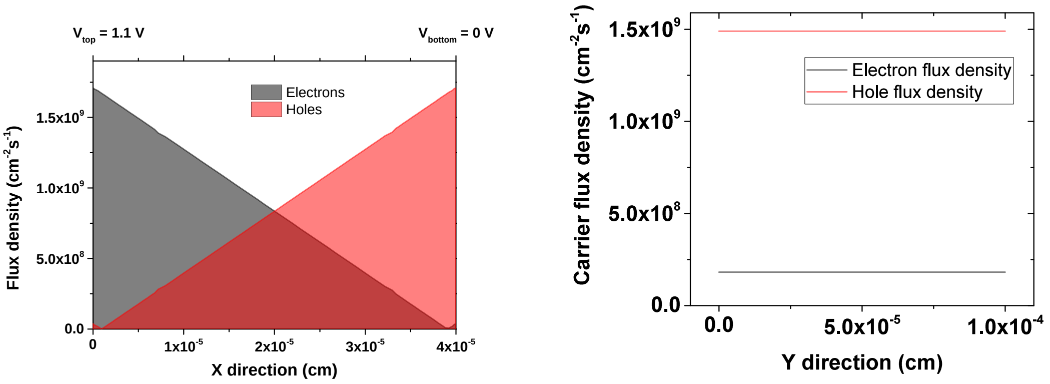

(a) Electron and hole flux density in the X direction (b) Electron and hole flux density in the Y direction

Figure 4.9: Electron and hole flux density in quasistationary simulations of the test structure.

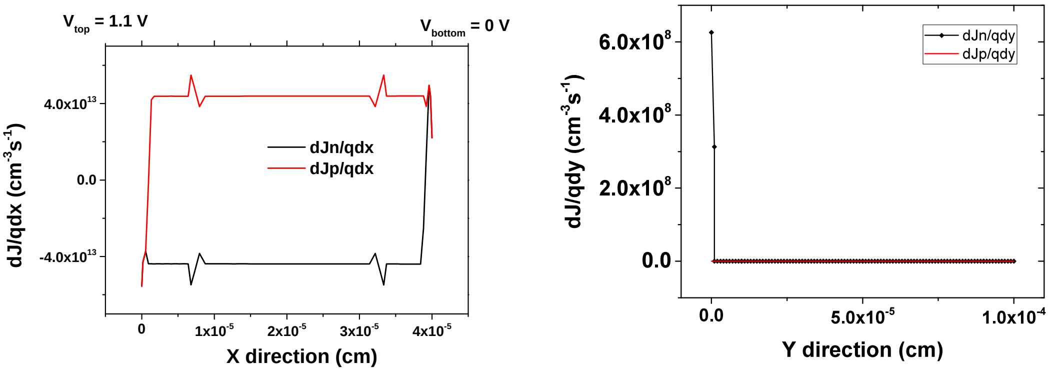

(a) Rate of change of the current density in the X direction (b) Rate of change of the current density in the Y direction

Figure 4.10: Rate of change of electron and hole current densities

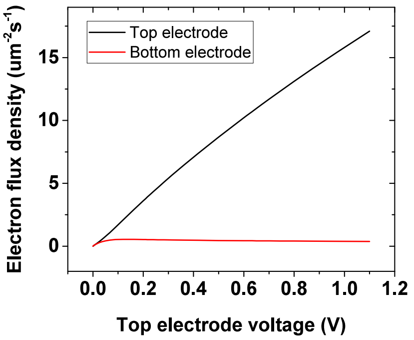

Figure 4.11: Contact flux during quasi-stationary simulation of the test structure as a function of V$_{top}$.

4.2.6 Transport in transient

Checks on quantitative accuracy of transport in transient is complicated to perform due to the time fluctuations of the current. The carrier flux densities inside the oxide for a one-dimensional cut at the middle of the top electrode after total dose of 3474 Rad(SiO_2) are shown in Figure 4.12(a) for V_{top} = 0 V and Figure 4.12(b) for V_{top} = 1.1 V.

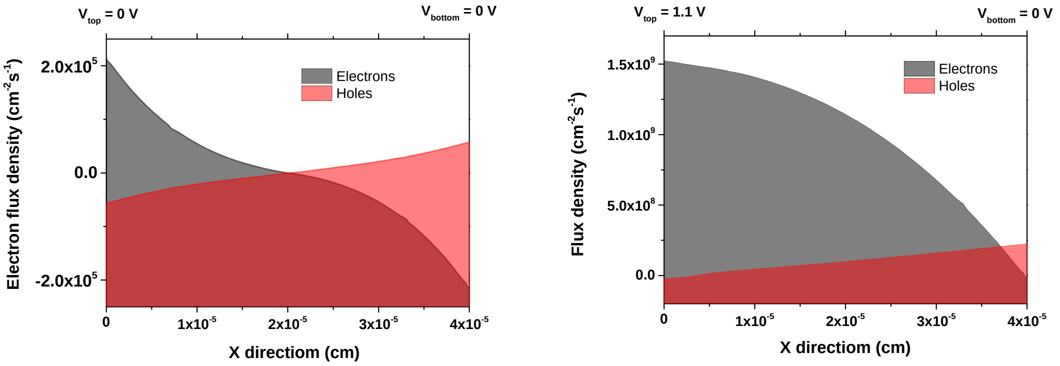

(a) Carrier flux densities in the x direction during transient simulation with V_{top} = 0 V, Total Dose = 3474 Rad(SiO_2)

(b) Carrier flux densities in the x direction during transient simulation with V_{top} = 1.1 V, Total Dose = 3474 Rad(SiO_2)

Figure 4.12: Flux densities in the test structure

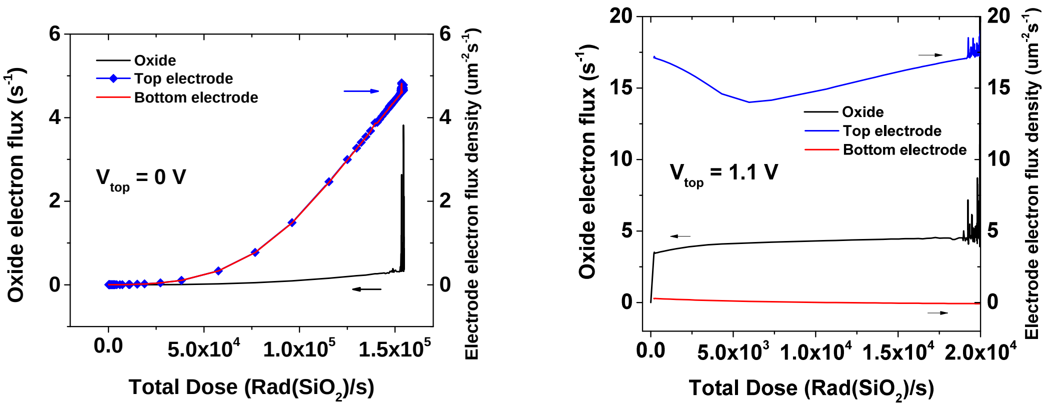

(a) Electron flux as a function of total dose with V_{top}=0 V

(b) Electron flux as a function of total dose with V_{top}=1.1 V

Figure 4.13: Flux densities in the test structure

As an example, the electron fluxes at the positions close to the top electrode are given in Table 4.6. These values are comparable to those of the electron flux going though the top electrode, as shown in Figures 4.13(a) and 4.13(b), namely, for V_{top}= 1.1 V, the top electrode electron flux is recorded to be 15.23 $\mu m^{-2}s^{-1}$ while for V_{top} = 0 V, 0.013 $\mu m^{-2}s^{-1}$.

V_{top} (V)	Location	e flux (cm^{-2}s^{-1})
0	top electrode	15.23×10^{8}
1.1	top electrode	21.32×10^{4}

Table 4.6: Electron flux at the positions of the electrodes as taken from the results in Figure 4.12

4.2.7 Hole trapping in quasistationary

The parameters used for the carrier trapping model are shown in Table 4.7. The degeneracy factor for the traps is unity. The J-factors for the traps are also unity. In the case of irradiation, we assume that trapping is dependent on carrier drift. In the case of no irradiation, only diffusion is considered as a trapping mechanism. We assume deep traps, therefore, an effective activation energy for the traps is set at 4 eV above valence band. The reason for this is explained in section 4.3.

In order to calculate carrier trapping-related results, some values were extracted from the simulator for V_{top} = 1.1 V. These are shown in Table 4.8. Using the equations presented in Section 3.2.5 the values shown in Table 4.9 were calculated analytically.

Description	**Symbol**	**Value**	**Units**
Conduction band degeneracy factor	g_{n}	1	
Valence band degeneracy factor	g_{p}	1	
Electron J-factor	$g_{\mathrm{n}}^{\mathrm{J}}$	1	
Hole J-factor	$g_{\mathrm{p}}^{\mathrm{J}}$	1	
Electron thermal velocity	v_{th}^{n}	2.042×10^{7}	cm/s
Hole thermal velocity	v_{th}^{p}	1.562×10^{7}	cm/s
Electron capture cross section	σ_n	10^{-12}	cm^2
Hole capture cross section	σ_p	6.8×10^{-14}	cm^2
Electron constant emission rate	$\mathrm{e}_{\mathrm{const}}^{n}$	0	s^{-1}
Hole constant emission rate	$\mathrm{e}_{\mathrm{const}}^{p}$	0	s^{-1}
Effective Density of States in CB	N_{C}	8.867×10^{18}	cm^{-3}
Effective Density of States in VB	N_{V}	1.931×10^{20}	cm^{-3}
Energy of donor traps	E_{trap}	E_{V}+4	eV

Table 4.7: Parameters used for the trapping model in sdevice

Substituting these values in (3.33) we get,

$$0.358153 = \frac{2.168\times10^{-70}+0.000101277}{\left(2.168\times10^{-70}+0.0001815\right)+\left(0.000101277+1.495\times10^{-53}\right)} \tag{4.10}$$

The RHS of this is 0.3562, therefore the quasi-stationary equations are solved correctly in the oxide.

Point	(-0.05078,0.5) μm	
E_C	1.25208	eV
E_V	-7.74792	eV
J_p	2.383×10^{-10}	A/cm^2
J_n	2.904×10^{-11}	A/cm^2
p	5.522×10^9	cm^{-3}
n	405.43	cm^{-3}
p_t^+	1.790×10^{13}	cm^{-3}
p_t	5×10^{13}	cm^{-3}
f_p	0.358158	
G_ehp	4.385×10^{13}	cm^{-3}s^{-1}
R_SRH	3.246×10^9	cm^{-3}s^{-1}

Table 4.8: Simulator output for calculation of occupational probability. V$_\text{top}$ = 1.1 V.

Point	(-0.05078,0.5)	
e^n_CB	2.168×10^{-70}	cm^{-3}s^{-1}
e^p_VB	1.495×10^{-53}	cm^{-3}s^{-1}
c^n_CB	0.0001815	cm^{-3}s^{-1}
c^p_VB	0.000101277	cm^{-3}s^{-1}
R_SRH	3.25023×10^9	cm^{-3}s^{-1}

Table 4.9: Calculated values for occupational probability of hole traps during quasi-stationary simulation, Y = 0.5 μm and V$_\text{top}$ = 1.1 V

4.3 Capacitor post-irradiation simulations

The irradiation simulations were performed in transient first and then in quasi-stationary mode after ‘freezing’ the traps in their state. The simulation flow is shown in Figure 4.14. T1 and T2 denote beginning and ending of transient simulations respectively. ’Q’ denotes quasi-stationary simulation beginning or ending. Transient simulations are solved for a specific time range. Quasi-stationary simulations, on the other hand, are solved for a random range t = 0→1. Any sweep on parameters is performed such that $P = P_0 + t(P_1 - P_0)$. Where P_0 is the initial value and P_1 is the final value.

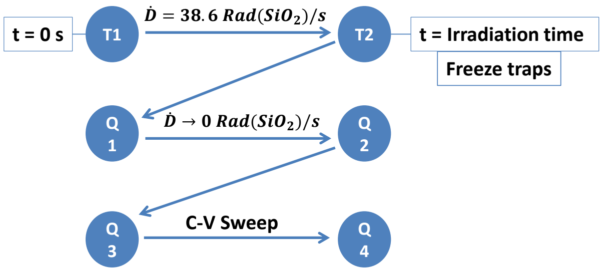

Figure 4.14: Simulation flow for the trapping equation in the capacitor

The average positive trapped charge density as a function of total dose was monitored during transient simulation and is shown in Figure 4.15(a). For sample B, the rate of change of trapped charge shows a reduction, however, saturation has not been reached up to the total dose of 58 kRad(SiO_2). The difference in the trapping rate is due to the different fixed oxide charge concentration defined to calibrate the pre-irradiation results.

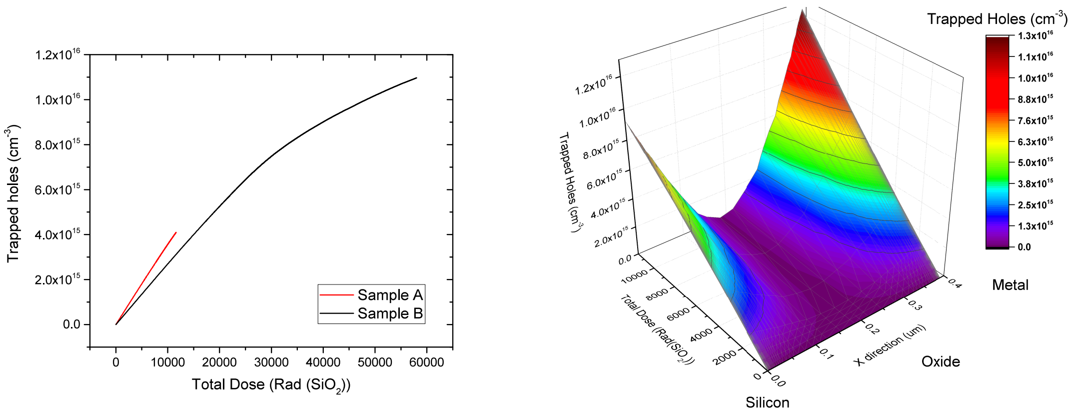

(a) Average trapped charge in the oxide as a function of total dose

(b) Evolution of trapped holes of sample A in a one-dimensional cut from the metal to the silicon in the oxide

Figure 4.15: Average traped charge and its evolutions in the oxide.

The evolution of the distribution of trapped charge in the oxide is shown in 4.15(b). With increasing total dose, the trapped charge is aggregated at the interfaces of the oxide with the metal and the silicon. This is due to the higher flux of the carriers created in the oxide at those locations and can be partly attributed to the electric field collapse effect as described in [9]. Initially, the carriers following paths according to their charge and the potential difference created based on the metal work-function and doping concentration in silicon. However, with increasing total dose, holes are trapped close to one of the interfaces and the electrostatic potential in the oxide changes causing the carriers to follow reverse paths. This process is repeated until equilibrium ($dp_t^+/dt = 0$).

4.3.1 J-coefficient

A set of simulations was performed to study the effects of drift and diffusion-enabled trapping. The j-coefficient in Equation 3.23 controls the percentage of contribution of its process to the final value of the trap occupational probability. Physically, at very low electric fields, diffusion is considered to be the dominant mechanism for the capture of holes, while at higher electric fields, diffusion is thought to prevail over drift [107]. This process, however, is interlinked with the carrier yield. At very low electric fields, the generated carriers can be significantly reduced, reaching zero during electric field collapse [9].

The average trap density in the oxide with increasing contribution of diffusion-enabled trapping and a uniform trap density of 10^{18} cm^{-3} is shown in Figure 4.16(a). Note that the sum of the drift and diffusion factors is 1. The trapped charge density is increased with increasing contribution of the drift motion of the holes in the trapping process. This is directly translated to increase in voltage shift in Figure 4.16(b). The reduction in the voltage shift value that occurs with the increasing contribution of the hole diffusion does not allow for adequately simulating the TID effect in the capacitor. Further simulations were performed to examine the issue.

In Figure 4.17(a), the average trap density and voltage shift with J-coef = 0.99 is shown. Above a trap density of 10^{17} cm^{-3}, there is no change in the average trap holes density. This is shown more clearly for three different contributions in Figure 4.17(b). It is seen that only 100% drift accurately represents trapping in the oxide as even 1% of diffusion causes an abrupt saturation of the midgap voltage shift and furthermore the goal of -1.5 V for sample A is not achieved.

4.3.2 Effective activation energy of traps

A number of studies have been made on the microscopic nature of the SiO_2 defects using density functional calculations. However, there is no general consensus over the most prevalent types and their characteristics. A good review is given in [59]. The

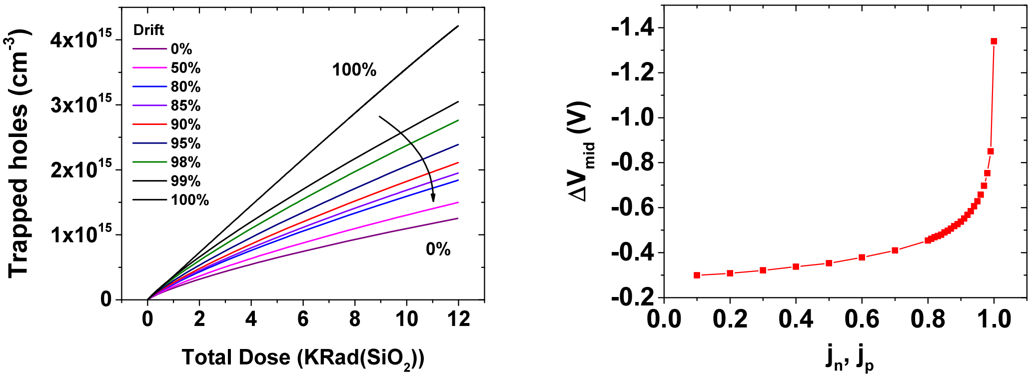

(a) Contribution of the drift motion of holes to the average trapped charge in the oxide. $p_t = 10^{18}$ cm^{-3}.

(b) Flatband voltage shift of the capacitor for different j-coefficient values.

Figure 4.16: J-coefficient effects on device response

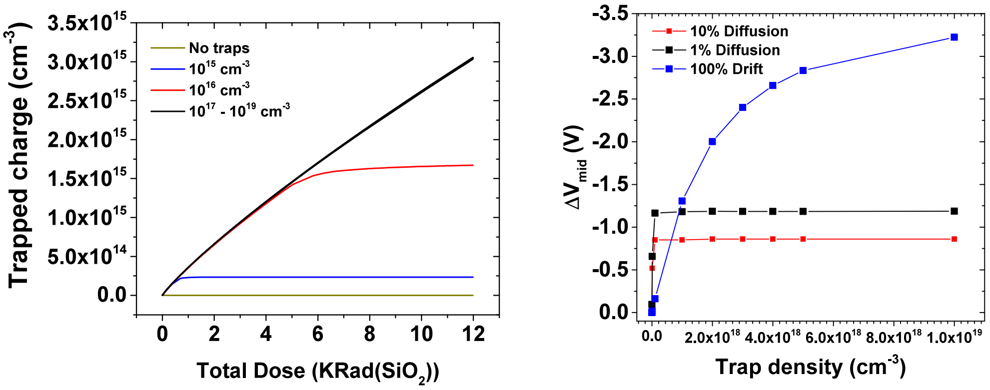

(a) Average trapped hole density in the oxide with different trap densities and 99% drift.

(b) Midgap voltage shift as a function of trap density.

Figure 4.17: Effect of drift and diffusion coefficient.

findings include a dimer configuration with a shallow activation energy ≈ 1 eV from the valence band edge and a concentration of 80% (E_δ' center) while bistable defects with an activation energy of ≈ 4.5 eV had a concentration of 20% (E_γ' center). Further studies have shown that immediately after irradiation, the predominant trapping site is the shallow E_δ', and, gradually, as the shallow traps get annealed with time, charges at shallow traps get annealed and get trapped in deep hole trapping sites [60, 108].

To test the effects of hole trapping under different activation energies of the traps, the average trapped charge in the oxide was recorded as a function of time. The results are shown in Figure 4.18. It is seen that the trapped charge is lower in the case of shallow traps with activation energy E_V+1 eV. This is due to the role played by the hole emission factor in Equation 3.17 for different values of effective density of gap states. The factors of this equation are shown in Table 4.10. This table shows that the hole emission factor in the case of shallow traps is higher, reducing the value of the occupational probability.

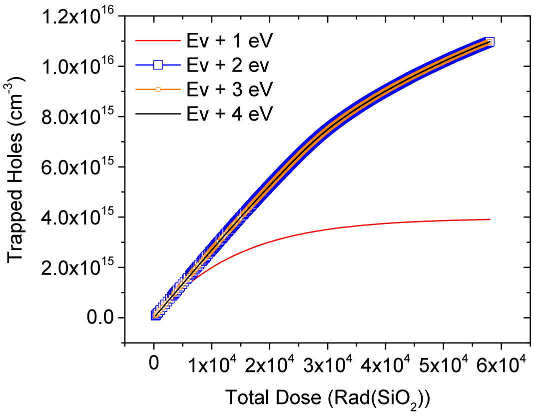

Figure 4.18: Average trapped charge in the oxide (sample B) as a function of time at different trap activation energies

The effective density of gap states for electrons (n_1) and holes (p_1) as a function of activation energy (E_{trap}) of the trap are shown in Figure 4.19. At lower values of the trap energy, the hole density increases significantly. This affects the hole emission factor, as shown in Figure 4.20. At E_{trap} = E_V+1 eV, the emission factor reaches the value of 0.00337 s^{-1}.

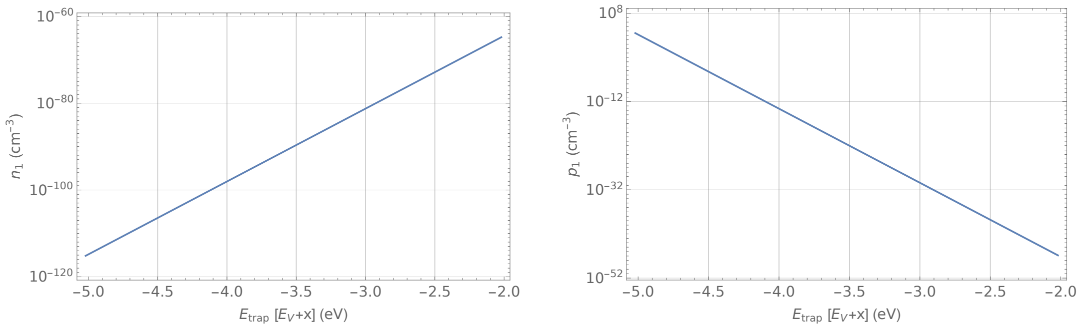

(a) Electrons (b) Holes

Figure 4.19: Effective density of carriers as a function of trap activation energy at the point (X,Y) = (0.05,0.5) μm in the oxide. The energy is measured in relation to the valence band. In the case of V_g = 0 V, E_V = -5.8208 eV.

		E_{v+1} eV	E_{v+4} eV	Unit
Occupational probability	f^p	0.00575	0.01311	
Electron emission factor	$v^n_{th}\sigma_n n_1$	9.62×10^{-121}	2.16×10^{-70}	s^{-1}
Electron capture factor	$\sigma_n j_n J_n/q$	7.73×10^{-5}	8.89×10^{-5}	s^{-1}
Hole emission factor	$v^p_{th}\sigma_p p_1$	0.00337	1.49×10^{-53}	s^{-1}
Hole capture factor	$\sigma_p j_p J_p/q$	3.86×10^{-4}	3.67×10^{-4}	s^{-1}

Table 4.10: Simulation output at time = 1000 s

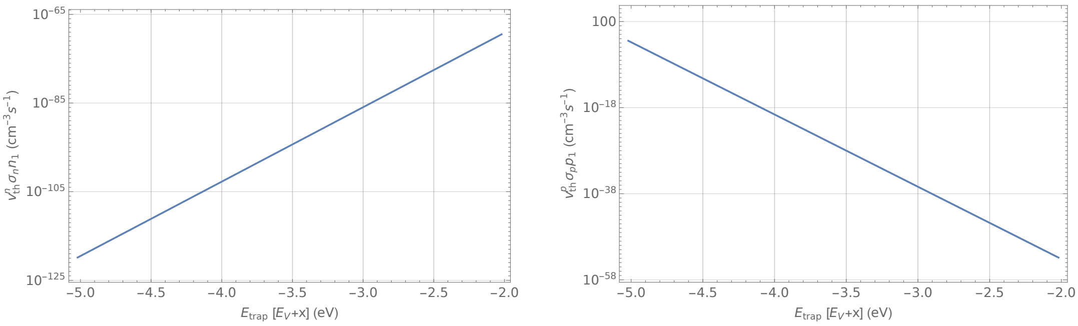

(a) Electron emission rate (cm^{-3}s^{-1}) (b) Hole emission rate (cm^{-3}s^{-1})

Figure 4.20: Electron and hole emission factor as a function of trap activation energy.

4.3.3 Calibrating trap density

The capacitors were calibrated to the midgap voltage (C_{mid}). This was found by solving the capacitor model with interface traps at a concentration of 10^{11} cm^{-3} deep within the silicon bandgap (0.56 eV from the conduction and valence band for electrons and holes respectively), as shown in Figure 4.21. C_{mid} and ΔV_{mid} were found from the point of intersection. This point represents the ‘intrinsic energy’ (E_i) in the middle between E_C and E_V. This computational method was used to avoid errors when extracting the midgap voltage analytically.

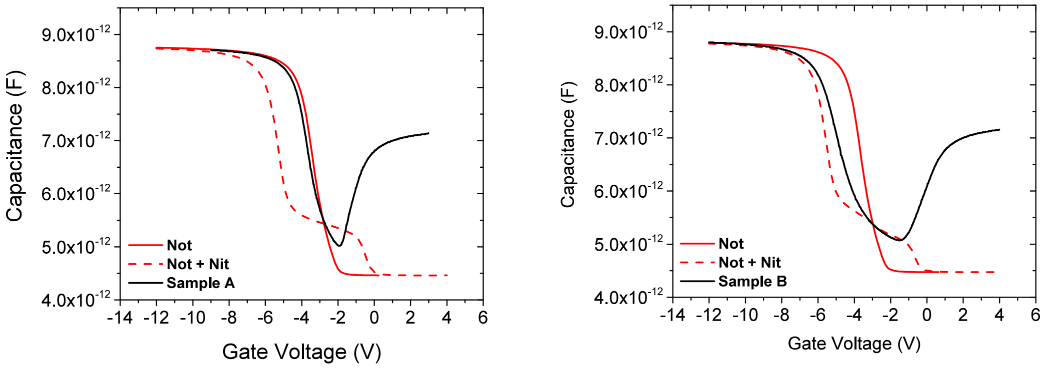

(a) Sample A (b) Sample B

Figure 4.21: Calibrating the effective oxide charge to C_{mid}

From this, the post-irradiation effective oxide charge, N_{ot}, was extracted. A transient solve was then performed separately, to extract the trap density, p_t. The C-V post-irradiation results for the two samples are shown in Figure 4.22. Table 4.11 lists important parameters for the simulations including post-rad charge density and trap density for each sample. Bulk trap densities are lower than found previously in commercial thick oxide capacitors [45]. This can be due to annealing of the trapped charge since the experimental measurements were performed one day after irradiation. The pre- and post-irradiation experimental and simulation results for sample A are shown in Figure 4.23.

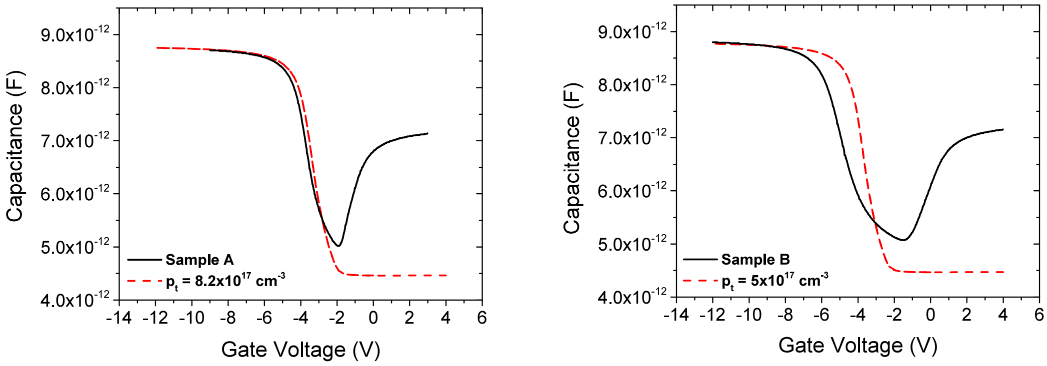

(a) Sample A

(b) Sample B

Figure 4.22: Capacitor C-V radiation simulations. The experimental results are shown in black and the simulation results are shown in red dashed line.

	Sample A	Sample B	
t_{ox}	391.5	389.5	nm
Pre-Rad N_{ot}	6×10^{15}	4.5×10^{15}	cm^{-3}
p_{t}	8.2×10^{17}	5.0×10^{17}	cm^{-3}
Post-Rad $p_{\text{t}}{}^{+}$	3.2×10^{15}	4.5×10^{15}	cm^{-3}
p_{it}	10^{11}	10^{11}	cm^{-2}

Table 4.11: Parameters for calibrating to midgap voltage

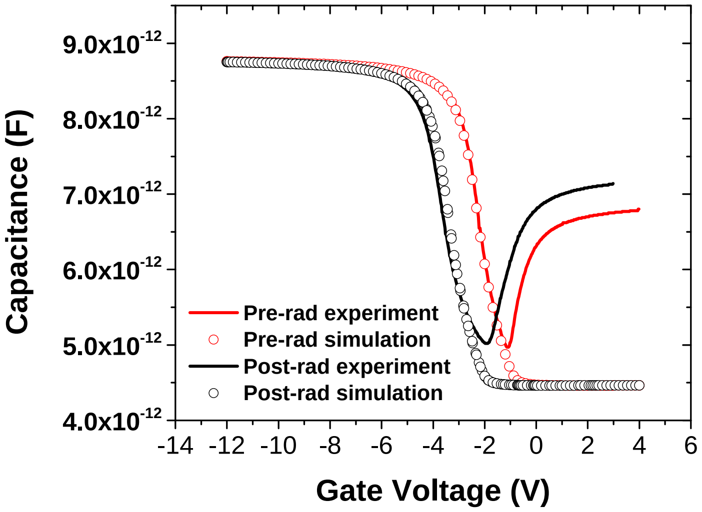

Figure 4.23: Pre and post-irradiation experimental and simulation results for sample A.

4.4 Hydrogen Transport in 400 nm SiO$_2$ capacitors

4.4.1 Interface traps

In this section, simulation of interface trap formation as a result of TID in the 400 nm SiO$_2$ capacitor samples is discussed. For this, we have used a third sample (sample C), irradiated at 290 kRad(SiO$_2$). Pre-irradiation fixed oxide charge of 3.7×10^{15} cm^{-3} was found for this sample and effective oxide thickness of t_{ox} = 388.5 nm. The pre- and post- irradiation characteristics are shown in Figure 4.24. The same simulation method was used to extract ΔV_{mid} as in section 4.3.3. The charge density used to fit post-rad characteristics is Post-Rad N_{ot} = 1.25×10^{16} cm^{-3}.

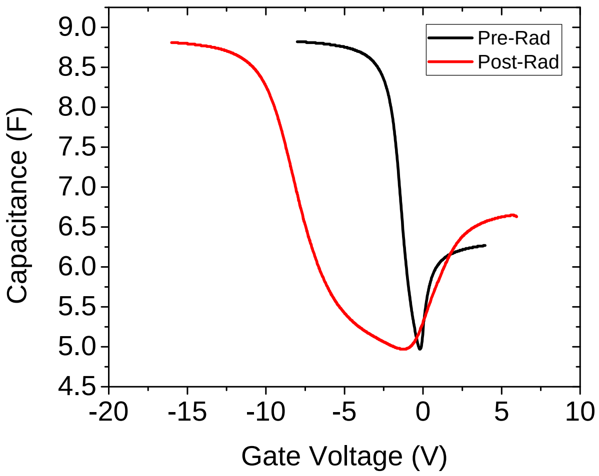

Figure 4.24: Pre and post irradiation results of capacitor sample irradiated at 290 kRad(SiO$_2$)

The activation energies of the interface traps will ultimately define the shape of the C-V curve, in addition to their densities. In Figure 4.25 are provided, for illustration purposes, the C-V results of sample B with different activation energies of acceptor and donor traps at a density of 10^{11} cm^{-2}. The values used for the cross sections are equivalent to the values used for the bulk traps and within the range given in [109]. From these figures we observe that a single trap energy level is not adequate to describe the interface state induced voltage shift. This was further confirmed at the interface trap density calibration process below.

Initially, fixed activation energies of 0.45 eV from either the conduction or valence band were used. The results are shown in Figure 4.26 and the densities are given in Table 4.12. These results were taken after numerous efforts with different combinations of energies and densities. Varying activation energies for the traps were used next. This is shown in Figure 4.27, while the densities for each activation energy are listed in Table 4.13.

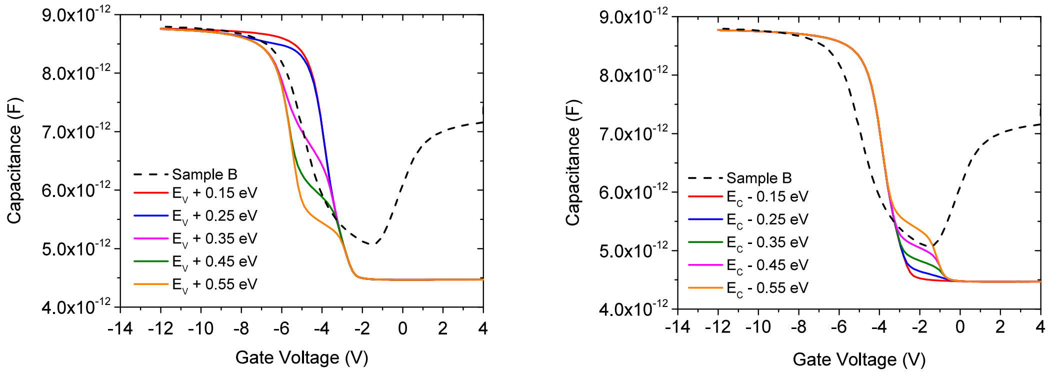

(a) Donor interface trap density 10^{11} cm^{-2} - Sample B (b) Acceptor interface trap density 10^{11} cm^{-2} - Sample B

Figure 4.25: Donor and acceptor interface traps at different activation energies with density 10^{11} cm^{-2}

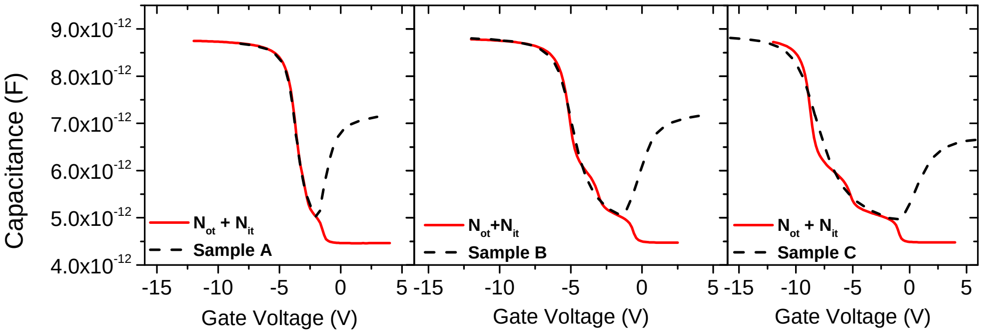

Figure 4.26: C-V results with N_{it} at fixed activation energies (as shown in Table 4.12)

		Density	Activation energy
Sample A	Donors	10^{10} cm^{-2}	E_V + 0.45 eV
	Acceptors	4×10^{10} cm^{-2}	E_C - 0.45 eV
Sample B	Donors	7.1×10^{10} cm^{-2}	E_V + 0.45 eV
	Acceptors	1×10^{11} cm^{-2}	E_C - 0.45 eV
Sample C	Donors	1.5×10^{11} cm^{-2}	E_V + 0.45 eV
	Acceptors	2×10^{11} cm^{-2}	E_C - 0.45 eV

Table 4.12: Densities of interface traps with activation energies of 0.45 eV from the conduction band for acceptors and valence band for donors.

Overall, for the three irradiated samples, acceptor and donor trap densities (eV^{-1}cm^{-2}) are shown in Figure 4.28. This is shown as a function of total dose, however, the samples are different, therefore small differences in the trap densities are thought to exist. Qualitatively, the interface traps show a logarithmic increase, indicating interface trap formation as a result of irradiation.

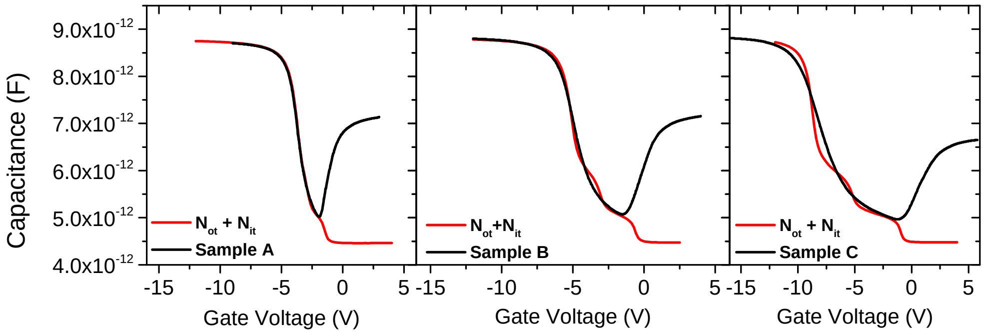

Figure 4.27: Interface traps with varying activation energies

		Density	Activation energy	Average
Sample A	Donors	10^{10} cm^{-2}	E_V + 0.45 eV	5.1×10^{9} eV^{-1}cm^{-2}
	Acceptors	4×10^{10} cm^{-2}	E_C - 0.45 eV	2×10^{10} eV^{-1}cm^{-2}
Sample B	Donors	3.4×10^{10} cm^{-2}	E_V + 0.37 eV	2.0×10^{10} eV^{-1}cm^{-2}
	Donors	3×10^{10} cm^{-2}	E_V + 0.52 eV	
	Acceptors	10^{11} cm^{-2}	E_C - 0.48 eV	5×10^{10} eV^{-1}cm^{-2}
Sample C	Donors	7×10^{10} cm^{-2}	E_V + 0.29 eV	4.8×10^{10} eV^{-1}cm^{-2}
	Donors	7×10^{10} cm^{-2}	E_V + 0.39 eV	
	Donors	5.8×10^{10} cm^{-2}	E_V + 0.53 eV	
	Acceptors	1.2×10^{11} cm^{-2}	E_C - 0.50 eV	6.7×10^{10} eV^{-1}cm^{-2}
	Acceptors	10^{11} cm^{-2}	E_C - 0.40 eV	

Table 4.13: Densities and activation energies of interface traps of C-V results in Figure 4.27

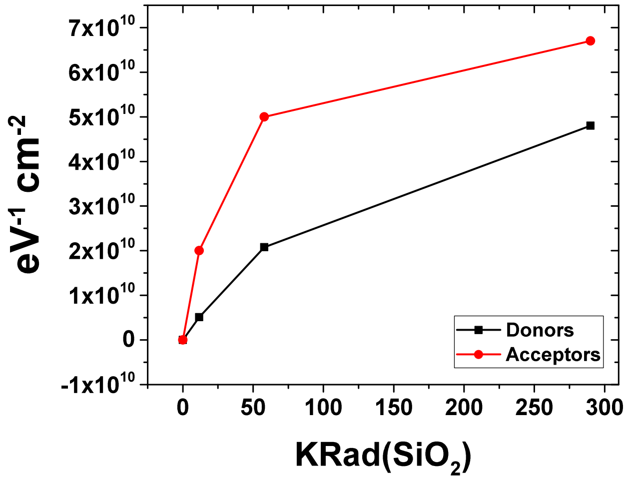

Figure 4.28: Interface trap increase as a function of total dose.

4.4.2 Interface trap formation using state transitions

Transport of hydrogen species at the Si/SiO_2 interface leads to reactions inducing interface states where positive and negative charges are trapped. The exact details of this process are varying in the literature. In MOS capacitors, the theoretical explanation given to this process is less detailed than in bipolar transistors due to the dose-rate dependent effect observed in the latter. The transition state diagram used in this work is shown in Figure 4.29.

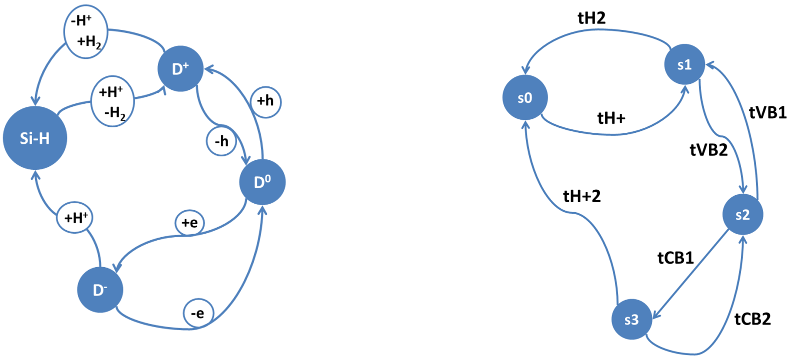

(a) Chemical reaction symbols (b) Symbolic names used in the simulator

Figure 4.29: State transition diagram showing passivation and depassivation of interface dangling bonds.

The chemical reactions taken into account are as described in [110]. The passivated Si-H bond turns into a positively charged interface state, D^+, absorbing a proton (H^+) and releasing a hydrogen molecule (H_2).

$$\mathrm{Si-H+H^+ \leftrightarrow D^+ + H_2} \tag{4.11}$$

H_2 leaving the interface then enters the SiO_2. We neglect dissociation of H_2 occurring in the silicon because transport of the molecule to the Si is very unlikely due to the very high barrier of the process. Passivation of the interface state is modelled using a) The reverse of reaction (4.11) and b) Negatively charged interface states capturing a H^+ (Reaction 4.11) [79].

$$D^- + H^+ \rightarrow Si - H \tag{4.12}$$

Concentrations, diffusion barriers and diffusion coefficients of the hydrogen species are shown in Table 4.14. Symbolic names of this table are given in Figure 4.29(b). H_2 concentration is dependent on the hydrogen existing in the environment during processing. H^+ formation is simulated using initial value concentrations uniformly spread inside the oxide. Their contribution to interface trap formation is then a result of their diffusive transport in the oxide.

	Si	SiO_2	Si/SiO_2	Ref.
H_2 concentration	10^{11} - 10^{18} cm^{-3}	10^{11} - 10^{18} cm^{-3}	10^{-300} cm^{-2}	[83]
H_2 diffusion barrier	2.4 eV	0.2 eV	0.2 eV	[110]
H_2 diffusion coefficient	10^{-4} cm^{2}s^{-1}	10^{-4} cm^{2}s^{-1}	10^{-4} cm^{2}s^{-1}	[79]
H^+ concentration	10^{-300} cm^{-3}	-	10^{-300} cm^{-2}	[83]
H^+ diffusion barrier	0.4 eV	0.7 eV	1.0 eV	[81, 83]
H^+ diffusion coefficient	1 cm^{2}s^{-1}	1 cm^{2}s^{-1}	1 cm^{2}s^{-1}	[79]

Table 4.14: Hydrogen species transport variables

It has been postulated in numerous studies that a H^+ arriving at the Si/SiO_2 interface moves laterally with a barrier of 0.2 - 0.3 eV until it finds and de-passivates a passivated dangling bond. In the case of an abrupt interface, the barrier to pass into the silicon is 1.0 eV, while in the case where it encounters a sub-oxide bond (a strained Si-Si bond on the side of the SiO_2) the barrier that the H^+ needs to overcome to move away from it is asymmetric (1.5 eV on the Si side) [68, 84, 110].

For simplicity, we are considering an abrupt interface here, and all H^+ trapping leads to de-passivation of dangling bonds. The direction of the H^+ is thought to occur only in the SiO_2-Si direction. Therefore, only the barriers for transport through the interface are considered.

Table 4.15 lists all variables used in state transitions. The barrier energies for passivation and de-passivation of the dangling bonds are taken from [110]. The thermal velocities used for H^+ is similar to that of H_2. The activation energies of the acceptor and donor traps created are defined in relation to the valence band.

	tH2	**tH+**	**tH+**	
Trap energy (eV)	0	0	0	
Activation energy (eV)	1.3	0.6	1.3	
Cross section (cm^2)	-	-	-	-
Thermal velocity (cm/s)	1.754×10^5	1.754×10^5	1.754×10^5	
	tCB1	**tCB2**	**tVB1**	**tVB2**
Trap energy (eV)	E_V+0.675	E_V+0.675	E_V+0.225	E_V+0.225
Activation energy (eV)	0	0	0	
Cross section (cm^2)	10^{-12}	10^{-12}	10^{-16}	10^{-16}
Thermal velocity (cm/s)	2.042×10^7	2.042×10^7	1.562×10^7	1.562×10^7

Table 4.15: State transition variables

4.5 Conclusions

The methodology used to simulate charge generation, transport and trapping in the oxide regions of MOS devices was presented. The method includes the oxide defined as a semiconducting structure with a wide bandgap and a Schottky contact with the metal gate. Operation of transport with the drift-diffusion model and bulk trapping mechanisms were first checked in a test structure. The effect of the activation energies the bulk traps as well as contributions from drift and diffusion-enabled trapping of the holes were explained. The simulation model was calibrated to experimental capacitors with 400 nm SiO_2. The post-rad characteristics were fitted to the midgap voltage of the irradiated capacitor using a computational method of calculating the intrinsic energy. The densities of the traps when a uniform trap concentration is taken into account was found to be 8.2×10^{17} cm^{-3} and 5×10^{17} cm^{-3} for two samples irradiated at 11.6 KRad(SiO_2) and 58 KRad(SiO_2) respectively. It was realised that for an accurate simulation of charge trapping after irradiation in the capacitors, the most important parameters were the density of the traps, their effective activation energies and the model used to calculate charge trapping (drift or diffusion enabled). These are adequate for calibrating simulation results to experiments.

Average interface trap densities per eV were extracted for the two aforementioned samples. A third sample irradiated at 290 kRad(SiO_2) was also simulated. The state transitions method of interface trap formation with irradiation was described. The drift-diffusion model was used in this case as well for transport of the carriers generated through irradiation in the oxide. Transport of hydrogen species was also activated. This method can lead to a full description of TID effects in the oxide. The only drawback to its implementation is that Synopsys Sentaurus does not currently include negative hydrogen ions (H^-) in its list of hydrogen species. H^- is included in some models of interface trap passivation and de-passivation in the literature and could potentially be essential to a realistic description of the model.

Chapter 5

Combined Random Dopant Fluctuations and Total Ionizing Dose effects in 45 nm PDSOI nMOSFETs

Previous studies on 45 nm and 32 nm PDSOI nodes have revealed increased TID hardness due to the high body doping incorporated to suppress short channel effects [19, 28] and the use of a thick silicon film that mitigates electrostatic coupling between the front gate transistor and any parasitic channels induced in the device after irradiation [111].

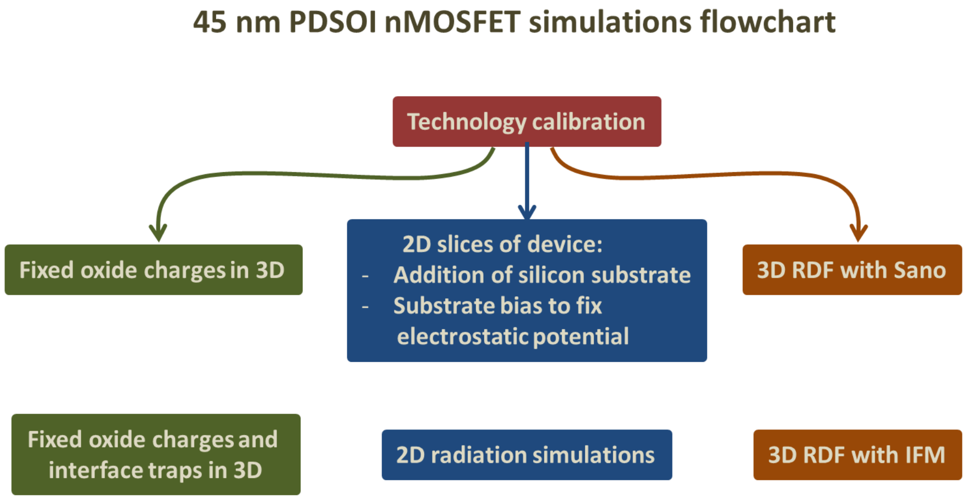

Figure 5.1: Flowchart of the simulations performed on the IBM 45 nm PDSOI MOSFET model.

RDFs as a source of variability become significant in deca-nanometer technologies. It has been suggested that at 45 nm they approach 50% of total variability [22]. TID results have been shown experimentally to become affected by variations from different sources in devices that showed no response deviation un-irradiated [112]. In this chapter, combined TID and RDF simulations of the 45 nm PDSOI nMOSFET, calibrated to the IBM node, are presented. The focus is on the effects that changes in the number and position of dopant atoms can have on the TID response of the device taking into account that such effects require a large number of devices to be measured.

Three-dimensional RDF simulations using the models described in Section 3.7 as well as two-dimensional simulations of irradiation using the bulk charge trapping method, as described in Chapter 4, are demonstrated. The model parameters derived in the last chapter are also used. These were extracted from calibrating to experimental results of thick oxide capacitors fabricated at the University of Southampton.

A flowchart presenting all the simulation stages is given in Figure 5.1. The technical difficulty involved in three-dimensional simulations of irradiation is significant. With adequate time and expertise, the model can be made to converge. Due to time constrains, only two-dimensional simulations were considered here. The latter provided a way to simulate important effects and different bias conditions fast. The RDF simulations were performed using two different methods (the Sano and IFM). These further allowed a comparison to be made between the two methods.

5.1 Calibration to the 45 nm PDSOI IBM node

A floating body 45 nm PDSOI nMOSFET was constructed in Sentaurus process (Figure 5.2). The steps are similar to the gate-first flow in [113]. The model is initially created in 2D. After placement of the BOX, and subsequent deposition of the top Silicon film, the STI is created. The threshold voltage adjustment implant preceded gate deposition and Source/Drain implant formation. Nickel Silicide was used for the contacts. At last, the device was extruded to 3D and the STI adjacent to the gate was formed using placement commands. The STI forms a corner of 85^o with the Silicon. The structure was finally mirrored in the X direction as shown in Figure 5.3. Important device characteristics and structural parameters are shown in conjunction with those in [114] and [115] in Table 5.1.

For the device simulation, hydrodynamic transport for electrons was used inside silicon. All other transport is modelled using drift-diffusion. The Philips Unified Mobility model is included with velocity saturation, mobility degradation due to the electric field perpendicular to the semiconductor-insulator interface. SRH avalanche recombination with *CarrierTempDrive* was used. All model parameters are given in Appendix B.

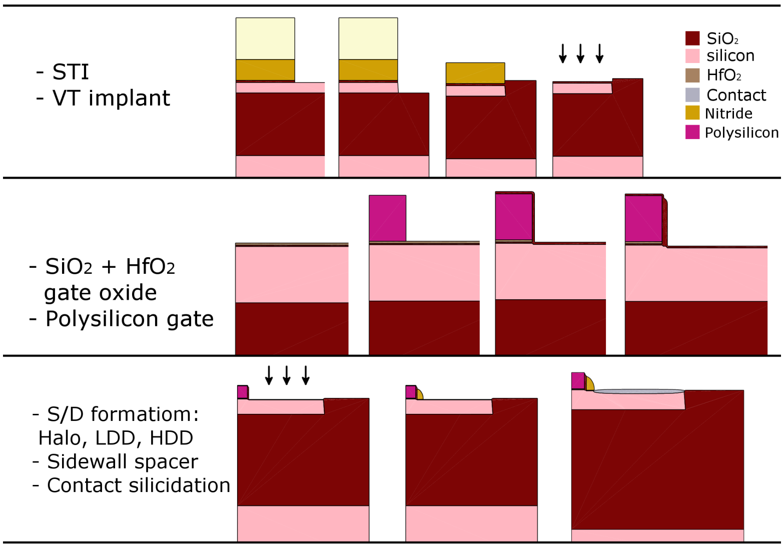

Figure 5.2: Process steps for the 45 nm PDSOI MOSFET simulation model

In fitting the MOSFET characteristics to the commercial node, a few points were kept in mind. Initially, the well implant was used for fitting V_t at 0.39 V [114]. The I_d-V_g of some of the devices with different Well and Halo implants examined are shown in Figure 5.4 (V_{dLin} = 50 mV, V_{dSat} = 1.0 V). The implant doses used are explained in Table 5.2. An increase in the off-state current is observed with decreasing well and Halo implant dose. Further HDD and LDD doses were examined and their characteristics extracted as shown in Table 5.3.

Threshold voltages (V_t), saturation current (I_{dSat}), off-state current (I_{off}) and sub-threshold slope characteristics (SS_{sat}) were extracted for all simulations and compared to [114]. The values that are finally chosen are shown in Table 5.4.

The I-V characteristics of the device compared to those found in [116] are shown in Figure 5.5. The 1D doping profile that resulted from this process in the two cuts shown in Figure 5.3(b) are given in Figure 5.6. The device shows a doping density of up to

Parameter	IBM 45 nm node	This work
Physical L_g (nm)	35	35
EOT (nm)	1.0	1.0
t_{Si} (nm)	60	50
I_{dSat}(μA/μm)	1240	1220
I_{off} (nA/μm)	200	4
V_t (V)	0.35	0.36
V_{dd} (V)	1.0	1.0

Table 5.1: Structural device characteristics of the 45 nm PDSOI MOSFET [114, 115].

	Well (cm^{-2})	Halo (cm^{-2})
Sim_1	4×10^{13}	4×10^{12}
Sim_2		1×10^{12}
Sim_3		9×10^{11}
Sim_4	2×10^{13}	4×10^{12}
Sim_5		1×10^{12}
Sim_6		9×10^{11}

Table 5.2: Varying implant doses for fitting 45 nm MOSFET characteristics

5.4×10^{18} cm^{-3}. The doping density in the third dimension is uniform and extends to the STI sidewalls.

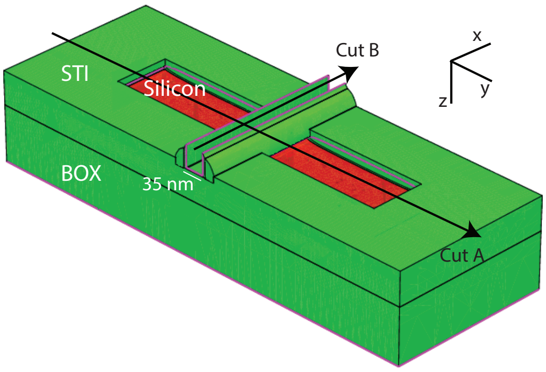

(a) 3D structure of the 45 nm PDSOI MOSFET

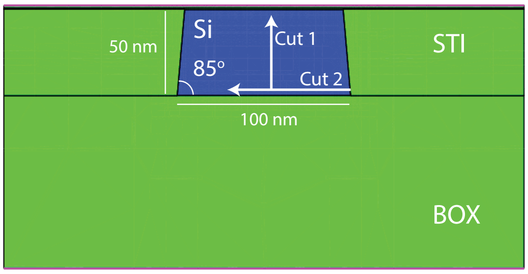

(b) Cut A

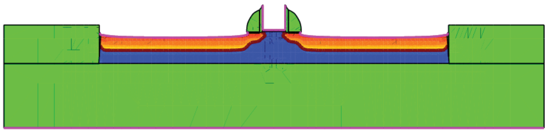

(c) Cut B

Figure 5.3: Structure of the 45 nm PDSOI MOSFET simulation model

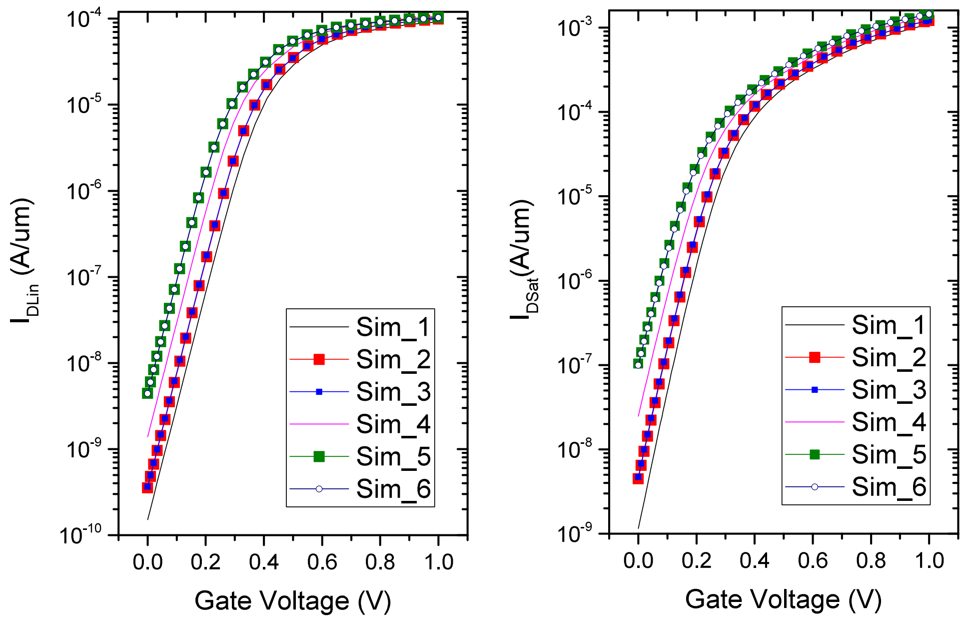

Figure 5.4: I_d-V_g characteristics used for fitting the simulation model to the 45 nm technology node.

LDD Dose (cm^{-2})	HDD Dose (cm^{-2})	V_{tlin} (V)	I_{dSat} ($\mu A/\mu m$)	I_{off} (nA/µm)	SS_{sat} (mV/dec)
5×10^{14}	6×10^{14}	0.368	1132	2	61.913
	8×10^{14}	0.360	1134	2	77.119
8×10^{14}	5×10^{14}	0.365	1220	4	62.914
	6×10^{14}	0.368	1207	3	62.117
	8×10^{14}	0.361	1184	3	77.766

Table 5.3: Varying LDD and HDD doses and resulting device characteristics of the 45 nm PDSOI MOSFET simulation model.

		Dose (cm^{-2})	Energy (keV)
Well implant	B	4.0×10^{13}	8.0
Halo	BF_2	9.0×10^{11}	20.0
LDD	As	8.0×10^{14}	2.0
HDD	As	5.0×10^{14}	6.0

Table 5.4: Implant doses and energies of the final simulation model.

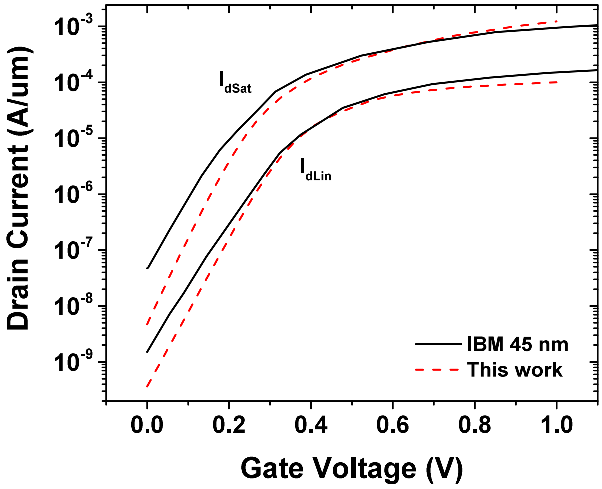

Figure 5.5: I_d-V_g simulation results of 45 nm PDSOI MOSFET compared to experimental results from [116].

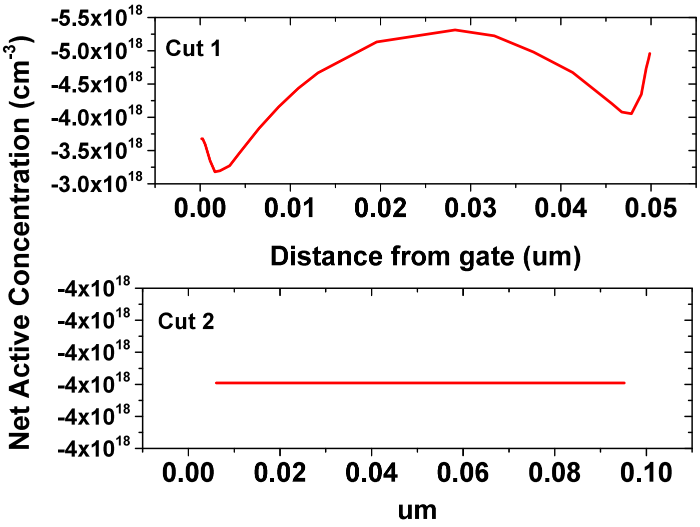

Figure 5.6: Doping concentration through Cut 1 and 2 as shown in Figure 5.3(c).

5.2 Fixed field oxide charges in the 45 nm PDSOI

The oxide regions surrounding the device are separated so that contributions from the STI and BOX are examined separately. The topology of the device at the corners created by the isolation oxides is very important to the device response [117]. The 'humps' observed in earlier technologies resulted from charges gathering at the top silicon/STI corner when the trench is recessed [118]. Other authors indicate the absence of humps in certain technologies [27, 49] and its correlation to simulation results with fixed oxide charges. It is generally concluded that humps are observed in situations where the top STI corner is not sufficiently rounded and irradiation occurs under zero bias, as positive gate voltages push holes to the opposite direction [76, 107, 119, 120]. In this work, we have used a planar STI configuration in order to examine the effects of RDFs on the sidewall channel excluding topology effects.

The 45 nm PDSOI model was constructed using a 85° STI inclination which is an average value for sub-100 nm MOSFET technologies [107, 121]. Furthermore, to investigate the case where no contact of the Source/Drain regions to the BOX occurs, shallow junctions of x_{j} = 20 nm were included.

Fixed charges were defined in the field oxides of the device. These were added to the BOX only, STI only and both the BOX and STI as uniform charge spread throughout the oxide volume. The I_{d}-V_{g} results are shown in Figure 5.7. The areal charge, N_{at}, is extracted by multiplying the volume density with the width of the oxide region. Explicit values of ΔV_{t} and ΔI_{off} are listed in Table 5.5.

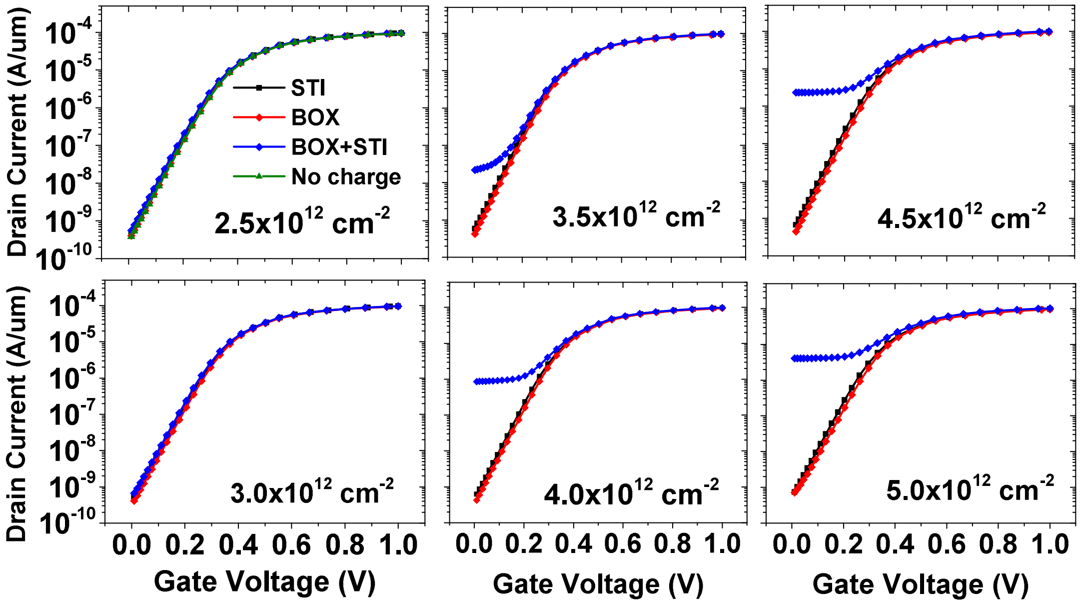

Figure 5.7: Uniform oxide charges in the BOX and STI.

	BOX		STI		BOX+STI	
Charge (cm^{-2})	ΔV_t (V)	ΔI_{off} (A)	ΔV_t (V)	ΔI_{off} (A)	ΔV_t (V)	ΔI_{off} (A)
2.5×10^{12}	-0.002	3.04×10^{-12}	-0.008	1.36×10^{-11}	-0.010	2.03×10^{-11}
3×10^{12}	-0.003	3.78×10^{-12}	-0.001	1.75×10^{-11}	-0.014	1.75×10^{-11}
3.5×10^{12}	-0.003	4.59×10^{-12}	-0.011	2.20×10^{-11}	-0.017	2.18×10^{-9}
4×10^{12}	-0.005	5.58×10^{-12}	-0.015	2.70×10^{-11}	-0.044	8.60×10^{-8}
4.5×10^{12}	-0.005	7.17×10^{-12}	-0.015	3.28×10^{-11}	-0.044	2.30×10^{-7}
5×10^{12}	-0.006	3.42×10^{-12}	-0.017	3.94×10^{-11}	-0.068	4.04×10^{-7}

Table 5.5: V_t shifts and increase in I_{off} at different oxide charge concentration energies

With the chosen planar STI topology, ΔV_t of 17 mV is observed during the highest examined charge density ($N_{at}=5\times10^{12}$ cm^{-2}). At this charge, also minimal coupling between the front and back transistors starts taking place. Longer channel PDSOI transistors that incorporate lower levels of body doping have exhibited front/back gate coupling similar to FDSOI architectures [122]. This does not seem to be a problem in the 45 nm technology and beyond, since the high body doping prevents full depletion of the top silicon film.

However, we clearly see that although there is no contact between the S/D implants and the BOX (due to the use of ultra-shallow junctions), the device exhibits off-state current. This only happens when both the BOX and STI charge is included. The off-state current and depletion region in this case is shown in Figure 5.8 for no charge and $N_{at}=5\times10^{12}$ cm^{-2}.

A large portion of the current is aggregated at the bottom Silicon corner. Figure 5.9 shows the electric field lines in the field oxides. Their direction further confirms that the bottom corner transistor takes place in our device. Holes created in the STI and BOX follow the direction of the electric field lines and get trapped in defect centers (E_γ' and E_δ') [60]. According to the theory, the trapped charge density will be higher towards the end of the lines at the interface with the silicon, as the hole flux there will be higher. Ionic hydrogen (H^+) also follows the same path. At the Si/SiO$_2$ interface, hydrogen can de-passivate dangling bonds creating either interface traps, or introducing fixed positive

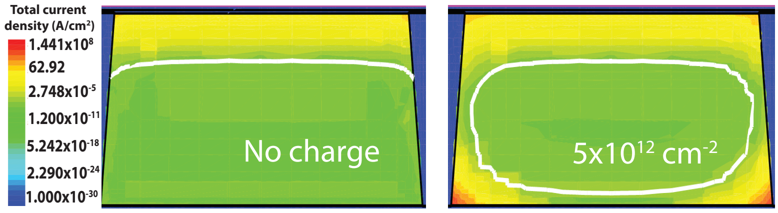

Figure 5.8: Depletion region and current density in a cut perpendicular to the gate for the cases of no charge and bulk charge of areal density $N_{at}=5\times10^{12}$ cm^{-2}. V_g = 0 V, V_{ds} = 0.05 V.

charge [68]. In our device, the field lines have a similar distribution as that in over-etched STI 0.2 μm PDSOI MOSFETs [27], moving from the STI to the BOX and from the BOX towards the silicon and the bottom silicon corner.

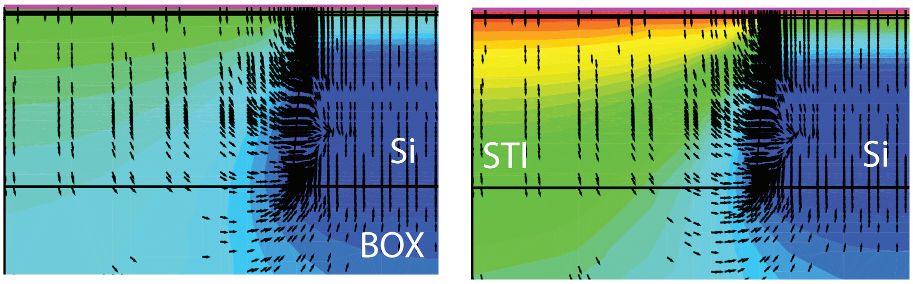

(a) V_g = 0 V, V_{ds} = 0.05 V (b) V_g = 1 V, V_{ds} = 0.05 V

Figure 5.9: Electric field lines in the field in the 45 nm PDSOI MOSFET model. The coloured gradient shows the electrostatic potential

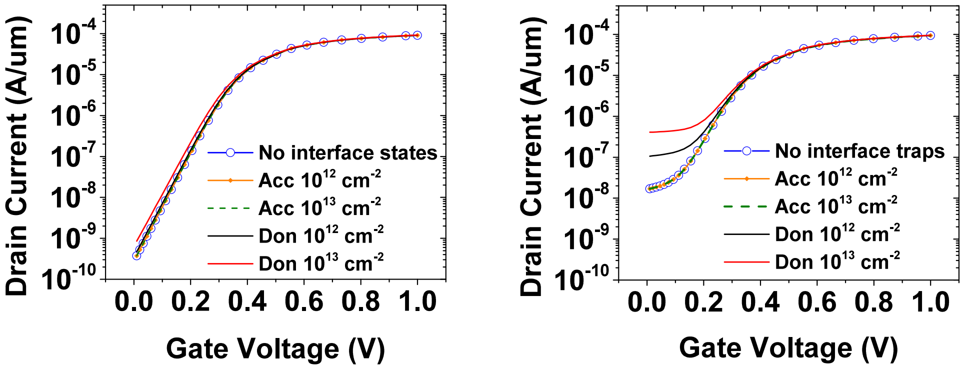

(a) No bulk oxide charge (b) N_{at}=3.5×10^{12} cm^{-2}

Figure 5.10: Interface traps introduced at the interface of the silicon with the BOX and STI. The device is solved with both no bulk oxide charge and bulk oxide charge of areal density 3.5×10^{12} cm^{-2}.

Simulations were also performed to examine the case where traps were formed due to transport of hydrogen species at the interface of the silicon film with the BOX and the STI. The I_d-V_g results are shown in Figure 5.10. Donor and acceptor interface traps were examined separately with areal concentrations up to 10^{13} cm^{-2}. The activation energies are 0.45 eV from the silicon conduction band for the acceptors traps and 0.45 eV from the valence band for the donor traps, that represent the worst case scenario.

Acceptor traps remained unoccupied based on the electrostatic potential at the Si/SiO$_2$ interface. Donor traps with concentration of 10^{13} cm^{-2} created a V_t shift of 12 mV and ΔI_{off} = 1.82×10^{-10} A/μm in the case where no bulk charge (N$_{ot}$) was considered. Under weak inversion of the parasitic transistor (N_{at} = 3.5×10^{12} cm^{-2}), further increase of leakage current when compared to the device with bulk oxide charge, ΔI_{off} = 3.93×10^{-10} A/μm, was observed. Interface traps have therefore increased I_{off} mostly at the point of weak inversion.

5.3 TID in 45 nm PDSOI MOSFET

The TID simulation methodology described in Chapter 4 is used here in two-dimensional models of the 45 nm PDSOI n-channel MOSFET.

A 2D cut is taken at the middle of the channel (Cut B in Figure 5.3(c)) in order to capture the effects of total ionizing dose in both the BOX and the STI. This is shown in Figure 5.11. The field oxides are simulated as semiconducting (OASC) structures.

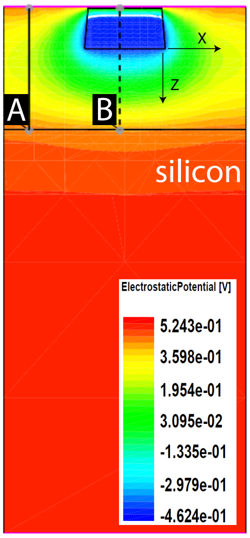

Figure 5.11: 2D slice of the 45 nm PDSOI MOSFET model

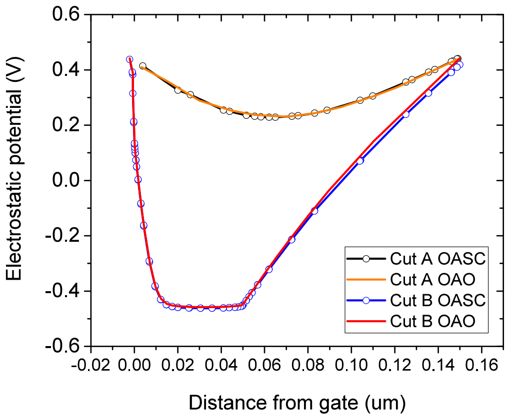

Figure 5.12: Calibration of electrostatic potential for radiation simulations.

The oxide region (OASC) has a direct contact with the gate, in order to simulate carriers escaping the material. There is an extra silicon region bellow the OASC. The OASC/Si interface has thermionic emission enabled. To fit the characteristics of the 3D transistor structure to the 2D slice, the electrostatic potential was fitted to the structure of the oxide as oxide (OAO) as shown in 5.12. A substrate bias of 0.8 V was applied to achieve this, as the potential changed after adding the Si region at the bottom. The hydrodynamic transport model can only be enabled for the whole simulation domain. It was therefore disabled as it was creating convergence issues. All transport is simulated using the drift-diffusion model.

The flux of the carriers generated inside the OASC region and passing through: a) the gate, b) the interface between the top silicon film and the OASC and c) the interface between the silicon substrate and the OASC are recorded and shown in Figure 5.13. The carriers follow paths according to the gate bias and the electrostatic potential charges due to trapping mechanisms. The flux through the interfaces is the average value for both directions. In Figure 5.13(a), electron flux through the gate electrode is higher at $V_g = 1$ V. Equivalently, hole flux in Figure 5.13(b) is higher at $V_g = 0$ V. The electron flux through the top silicon film interface with the oxide is increasing in both bias conditions (Figure 5.13(c)), and the hole flux (Figure 5.13(d)) is decreasing due to the increase in the number of holes trapped at the interface. Also, zero bias seems to favour hole transport through this interface more than electron transport through it. For the electron flux through the interface with the substrate (Figure 5.13(e)), while its value is higher under $V_g = 1$ V, however equilibrium does not seem to be reached. For the hole flux (Figure 5.13(f)), the lower value of flux density that occurs under $V_g = 1$ V could be due to the charge trapped at the bottom of the BOX.

2D trapped charge simulation results under the two bias conditions are shown in Figure 5.14. During both bias conditions, most of the trapped charge is aggregated around the silicon film. At $V_g = 1$ V, the trapped charge density is increased at the bottom of the BOX, as the holes are pushed towards it by the positive gate bias. This reduces the amount of holes trapped underneath the silicon film (Figure 5.14(b)).

The charges trapped in the oxide at the bottom silicon corner as a function of distance from it are shown in Figure 5.15 for $V_g = 0$ V and Figure 5.16 for $V_g = 1$ V. The initial concentration of trapped holes at the beginning of irradiation is nearly uniform and shaped by the electric field distribution. With increasing total dose, the trapped holes distribution is shaped by the change in the electric field.

In all cases, a reduction of the charge density is observed at approximately 400 KRad(SiO_2) and beyond. This is due to thermionic emission after inversion electrons reach the bottom corner. It is shown more clearly here that at $V_g = 1$ V, the charge trapped at the bottom of the BOX is increased at higher levels than around the silicon film due to the positive gate bias pushing holes towards the substrate.

Using Equation 3.39, the areal charge at the two directions at the bottom of the silicon angle is plotted as a function of total dose in Figure 5.17. It is seen that its value is increasing nearly identically in all directions. The highest areal trapped charge concentration is approximately 2×10^{11} cm^{-2} and is well below the inversion charge concentration of $\approx 3.5\times10^{12}$ cm^{-2} observed in section 5.2.

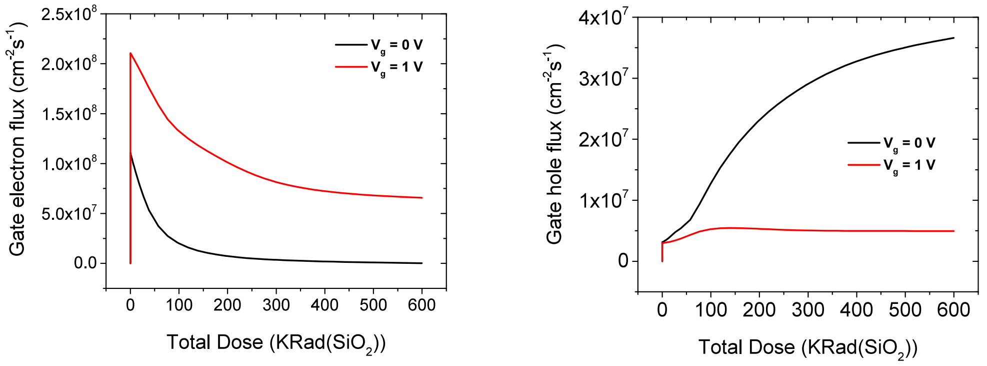

(a) Gate electron flux (b) Gate hole flux

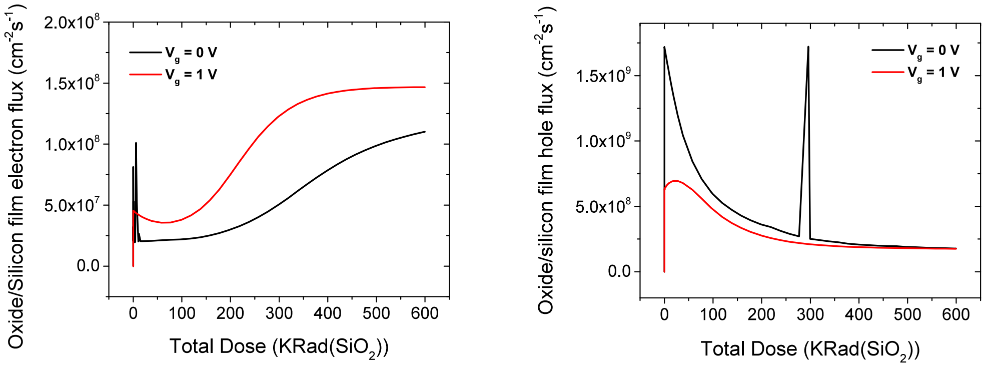

(c) Average oxide/silicon film electron flux (d) Average oxide/silicon film hole flux

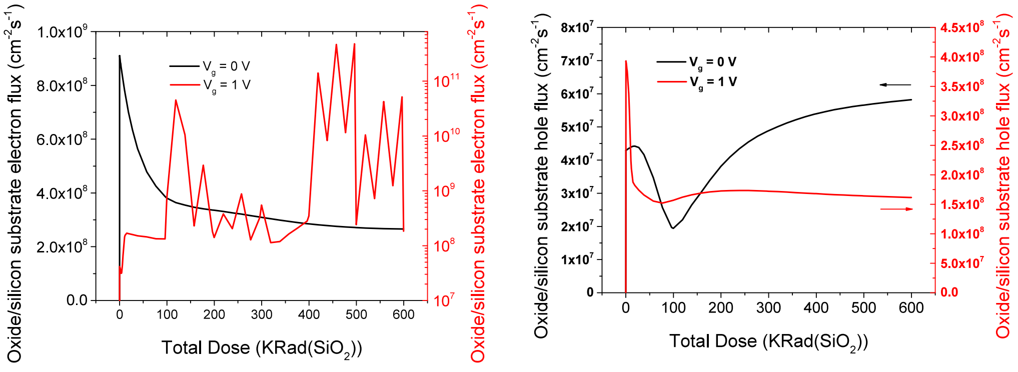

(e) Average oxide/silicon substrate electron flux (f) Average oxide/silicon substrate hole flux

Figure 5.13: PDSOI MOSET current densities passing through the gate contact and the interface of the oxide with the silicon

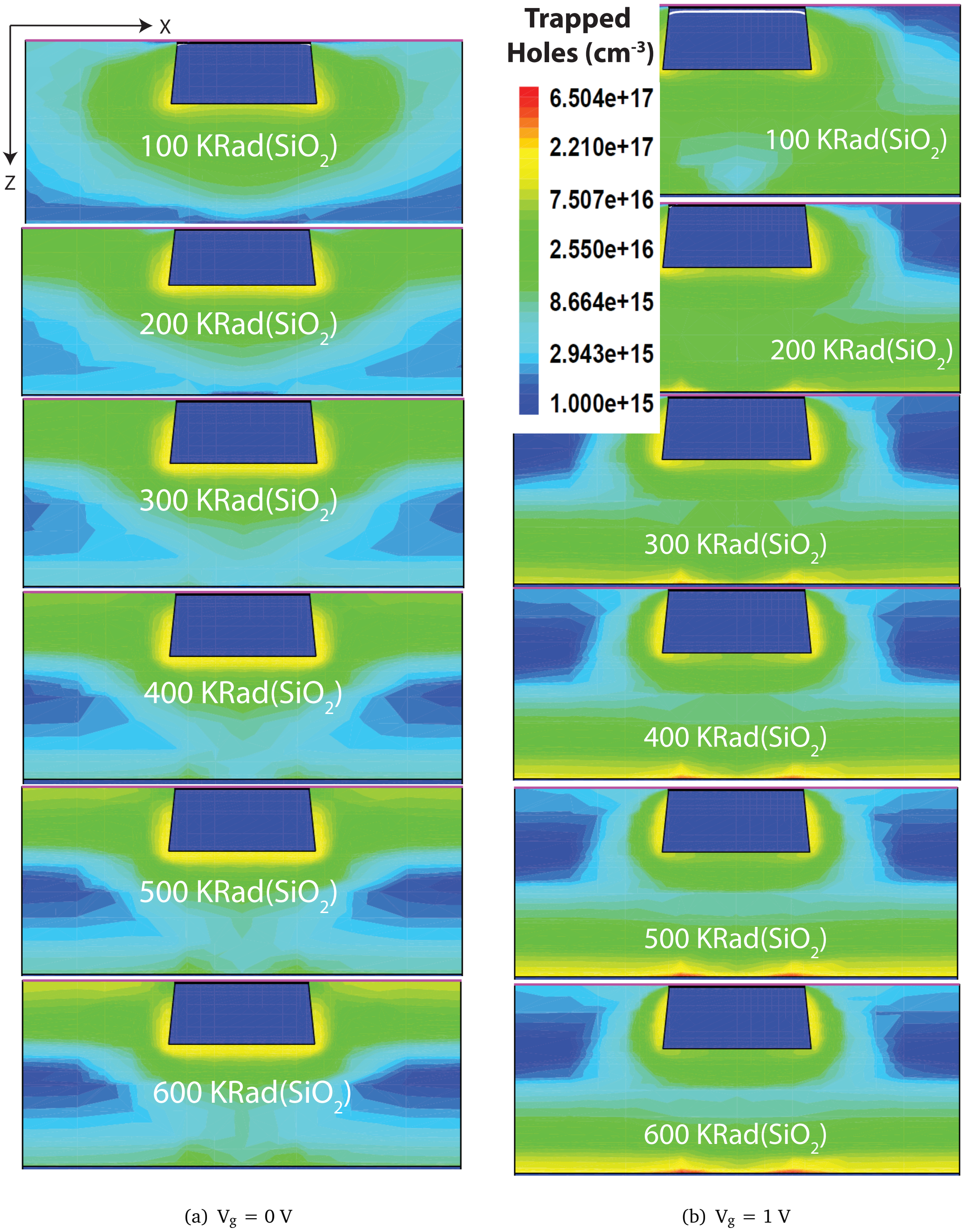

(a) V_g = 0 V (b) V_g = 1 V

Figure 5.14: Trapped holes in two-dimensional cut in the oxide (cm^{-3})

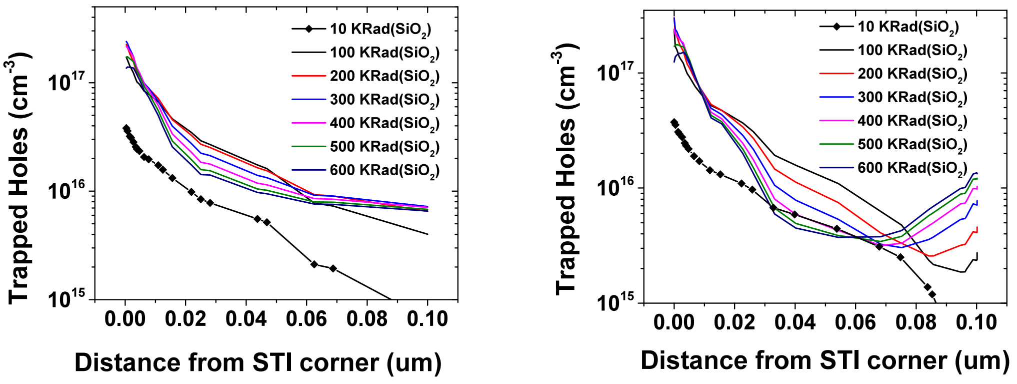

(a) X direction (b) Z direction

Figure 5.15: Trapped holes as a function of distance from the bottom silicon corner, $V_g = 0$ V

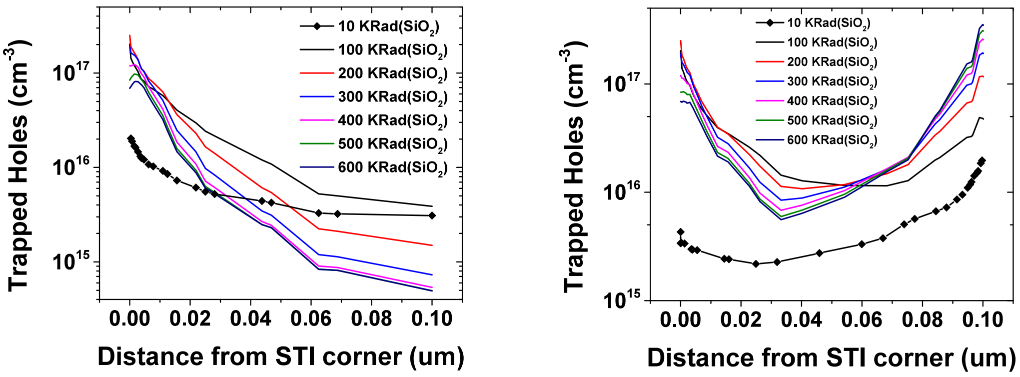

(a) X direction (b) Z direction

Figure 5.16: Trapped holes as a function of distance from the bottom silicon corner, $V_g = 1$ V

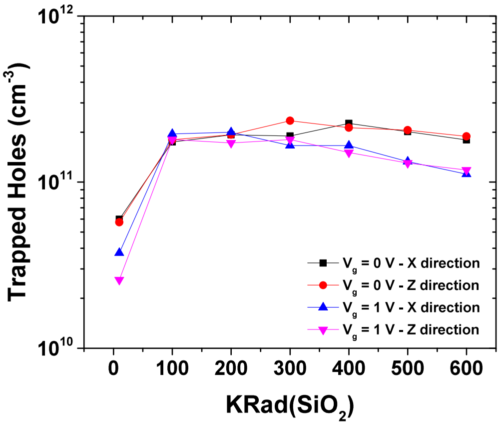

Figure 5.17: Areal charge at bottom silicon corner as a function of total dose

5.4 Random Dopant Fluctuations in the 45 nm PDSOI

5.4.1 Sano method

100 devices with randomized doping profiles were constructed in Sentaurus Mesh using the Sano method described in Section 3.7.1. Only the region directly underneath the gate was randomized (Figure 5.18(a)). The randomized species dataset is BoronActiveConcetration. Arsenic species randomization produced zero atoms in the given region. The rest of the implant profiles were therefore kept as they were. The total number of Boron atoms in this volume of the uniform profile transistor is 600. The range of the total Boron atom count during randomization was between 570 and 700 (Figure 5.18(b)) showing a normal distribution with a tail towards the maximum.

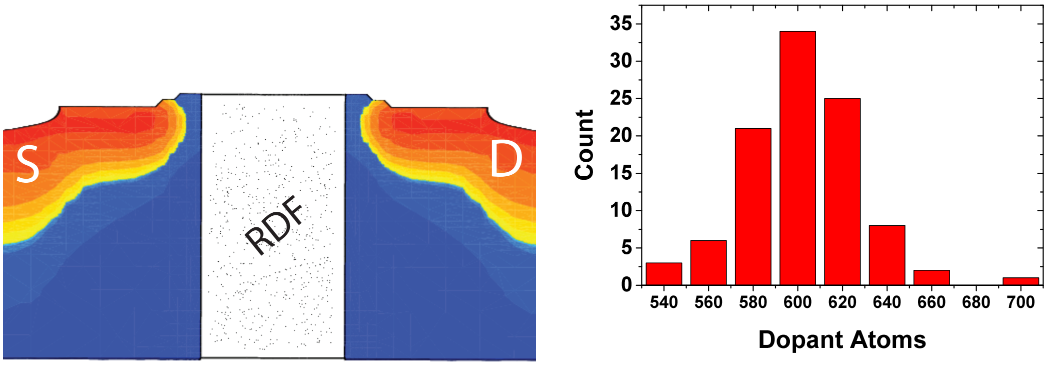

(a) Region where the RDFs are applied

(b) Frequencies of devices with total number of atoms in the region where randomization was performed as labelled in X axis

Figure 5.18: RDF volume and atom frequency counts.

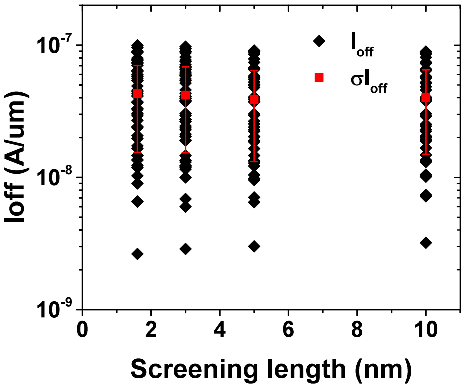

Figure 5.19: Effect of screening length in I_{off} of the randomized profile devices.

During the test procedure, the effect of the screening length to the I_{off} characteristics of the randomized devices was examined. This is shown in Figure 5.19. The spread in I_{off} values reduces with increasing screening length. The mean remains stable to a very good accuracy. Therefore, the value chosen for the screening factor is 3.3×10^6 cm^{-1} resulting from the Conwell-Weisskopf model with a doping concentration derived from the integral functionality in Sentaurus visual.

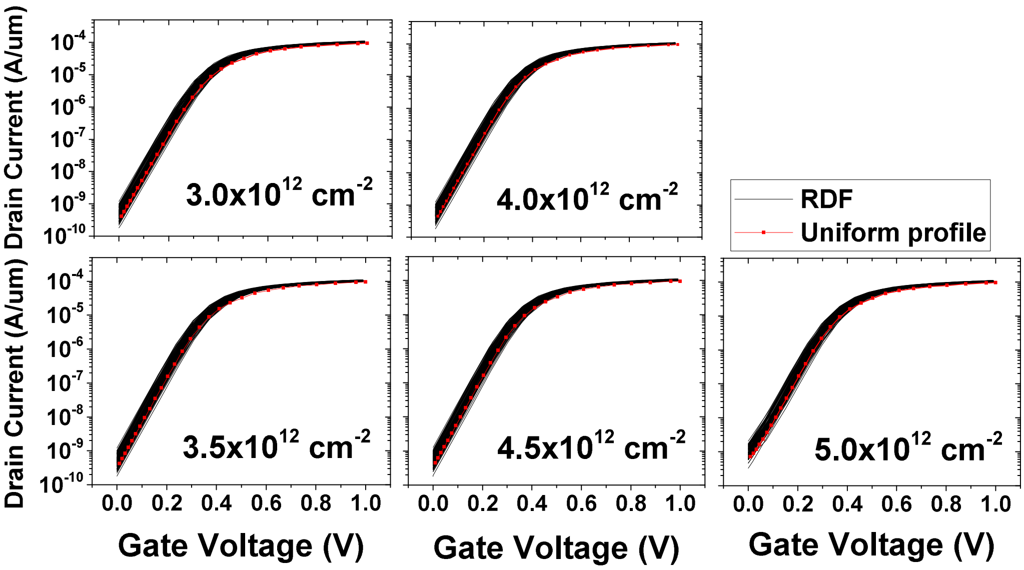

Figure 5.20: Combined RDF and TID results for charges defined in the BOX only

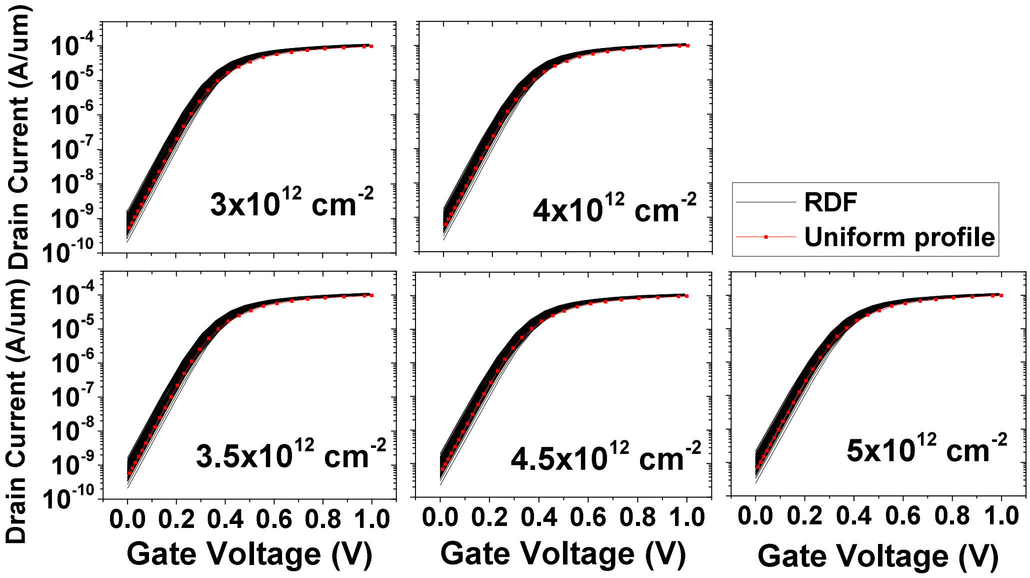

Figure 5.21: Combined RDF and STI results for charges defined in the STI only

I_d-V_g results of the devices with the randomized doping profiles for the cases of BOX and STI charge only are shown in Figures 5.20 and 5.21 respectively. RDFs appear to increase I_{off} and reduce V_t, however, the effects do not differ as oxide charge is increased. RDF I_d-V_g results for both BOX and STI charge are shown in Figure 5.22. RDFs most profoundly affect sub-threshold characteristics when $N_{at}=3.5\times10^{12}$ cm^{-2} is introduced in the oxides.

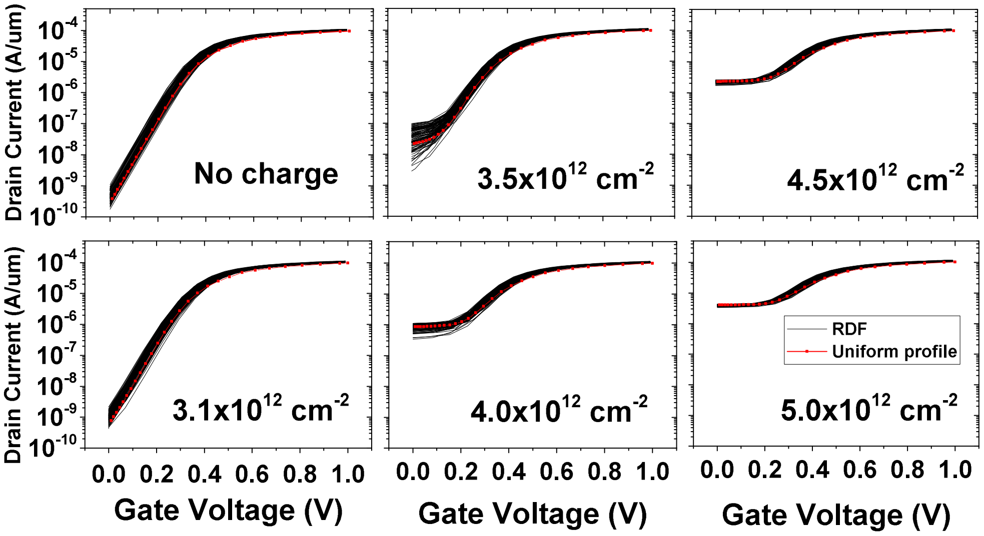

Figure 5.22: Combined RDF and STI results for charges defined in BOX and STI

It is also observed that at 3.5×10^{12} cm^{-2}, the uniform profile device shows lower subthreshold current values than the mean. This could potentially be caused by the lowering of the V_t of the parasitic transistor due to randomizing the position and number of the dopant atoms. The electrons can thus find the easiest routes through the channel and inversion occurs easier [123, 124]. The tail in the distribution of the dopant atoms in the randomized region (Figure 5.18(b)) is directly translated to the devices showing the highest resistance to TID during parasitic channel inversion. Threshold voltage (V_t) RDF results for the case of both BOX and STI charge are shown in Figure 5.23. σV_t remains constant in all states of the parasitic transistor.

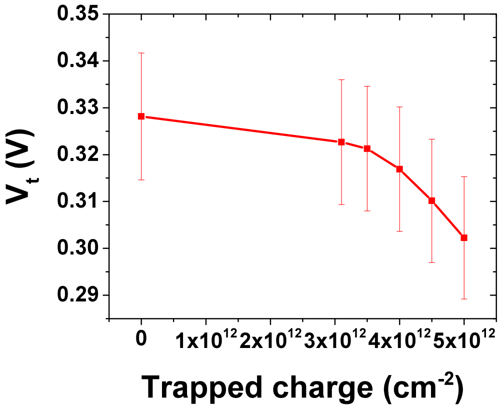

Figure 5.23: Standard deviation of threshold voltage of randomized devices

5.4.2 IFM Simulations

IFM simulations were performed for the same values of oxide charge examined in the previous section. Randomization was enabled for the same volume of the silicon film shown in Figure 5.18(a). Both Acceptor and Donor atoms were randomized. The two sources of variation were treated by sdevice as uncorrelated.

Attention was paid to the extraction method used for the I_d-V_g results of the randomized profile devices produced with the IFM. The linear current response of the randomized profile, $\delta \mathrm{I}_\mathrm{d}$, is linked to the nodal drain current $\mathrm{d}I_\mathrm{d}$ and the gate voltage $\mathrm{d}V_\mathrm{d}$ variations through the boundary condition [10],

$$\mathrm{d}I_\mathrm{d} = \delta I_\mathrm{d} + y_\mathrm{d,g}\mathrm{d}V_\mathrm{g} \tag{5.1}$$

where,

$$y_\mathrm{d,g} = \frac{\partial I_\mathrm{ref,d}}{\partial V_\mathrm{g}} \tag{5.2}$$

and $I_\mathrm{ref,d}$ is the drain current of the reference device.

There are different techniques used to derive I_d-V_g characteristics from the linear current response. These techniques are appropriate either for the on state of the transistor, weak inversion or leakage current. None of them, however, completely covers the situations examined in this work. Namely, it is not just the state of the front gate transistor that is recorded in the I_d-V_g results, but also the state of the parasitic transistor.

Two extraction methods were therefore used for the I_d-V_g results. The ‘exp’ method was used in the cases where the parasitic transistor is in the off state. The drain current in this case is given by [10],

$$I_\mathrm{v,d} = I_\mathrm{ref,d}\mathrm{exp}\left(\frac{\mathrm{d}I_\mathrm{v,d}}{I_\mathrm{ref,d}}\right) \tag{5.3}$$

This method is appropriate for leakage current, but not for the other transistor states. This is due to the breaking of the linearity assumption which results in non-Gaussian distribution of drain current in other bias regimes. Therefore, the ‘dI’ method is used for the cases where the parasitic transistor is in the weak inversion or the on state. This is given by [10],

$$I_\mathrm{v,d} = I_\mathrm{ref,d}\left(V_\mathrm{ref,g}\right) + \mathrm{d}I_\mathrm{v,d} \tag{5.4}$$

For the cases where non-physical, negative results occurred during the parasitic channel weak inversion, the 'exp' method was used to represent those specific I_d-V_g results.

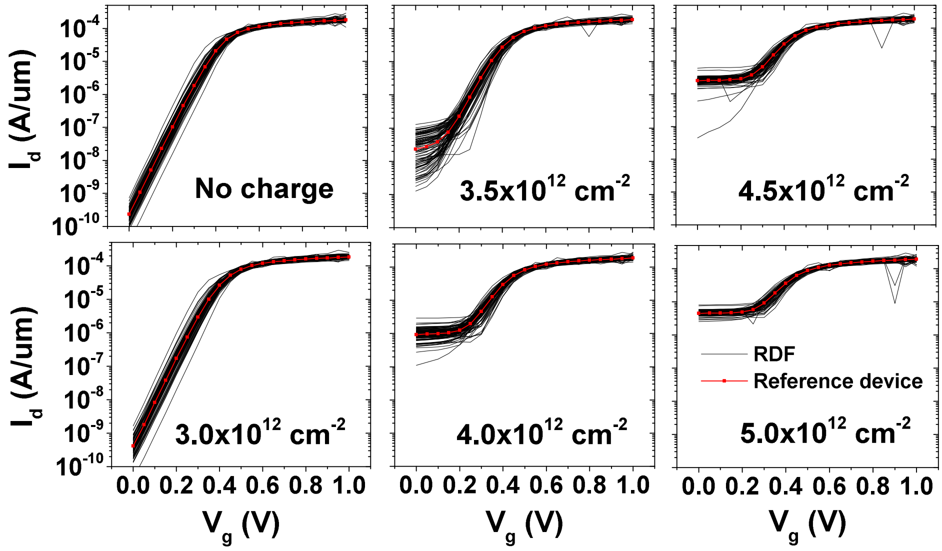

Figure 5.24: Combined RDF and STI results for charges defined in BOX and STI

The final characteristic of the randomized profile devices are shown in Figure 5.24. Up to oxide charges of 3.0×10^{12} cm^{-2}, the 'exp' method is used, while the 'dI' method is used for the remaining charges examined. The trends are similar to those in the results of the Sano method with the randomized profile devices exhibiting higher I_off spread as we approach the parasitic channel weak inversion and then reducing as the parasitic channel is completely turned on. The artefacts in the saturation region are due to the extraction method chosen.

A comparison between the two randomization methods is shown in Figure 5.25. The relative standard deviation in this figure is the ratio of the standard deviation of I_off to the mean. The trend is for RSD to increase until the $N_\mathrm{at}=3.5\times10^{12}$ cm^{-2} (parasitic transistor weak inversion) and then reach practically zero towards 5.0×10^{12} cm^{-2} (parasitic transistor saturation). The two methods are in good agreement, with the IFM producing slightly higher spread in I_off values.

The RSD(I_off) and I_off results of the devices with the randomized doping profiles using the IFM for the case where donor interface traps are included are shown in Figure 5.26. The interface traps considered have a concentration of 10^{13} cm^{-2} and are 0.45 eV from the valence band. The effects of the RDFs are similar to the case where fixed charge is considered. The point of weak inversion of the parasitic transistor has shifted to lower values of oxide charge (3×10^{12} cm^{-2}). However, the spread in I_off is again in its maximum during this condition and then reduces to negligible values when the parasitic transistor is completely turned on.

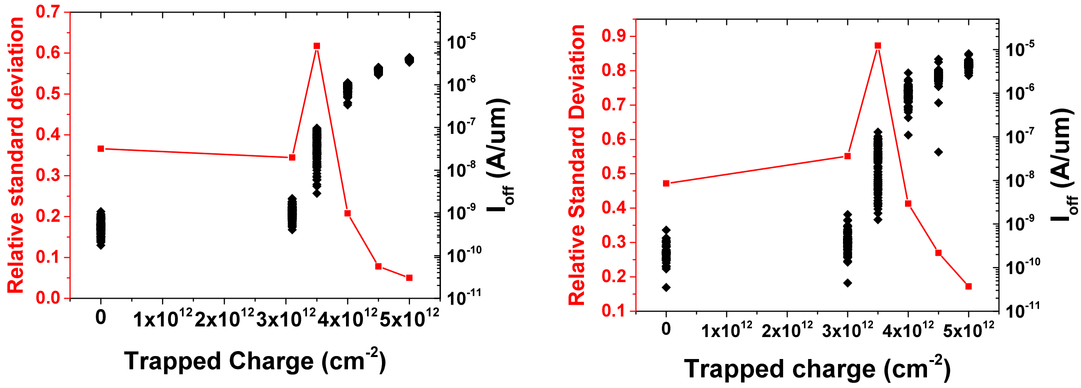

(a) Sano method (b) IFM

Figure 5.25: Relative standard deviation and I_{off} values as a function of oxide charge for the two RDF methods examined.

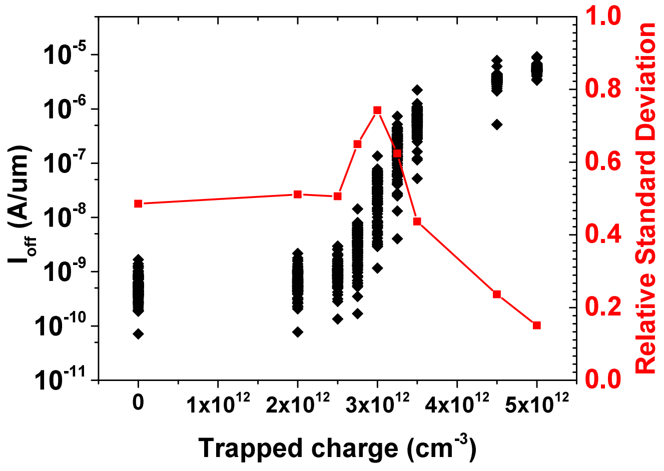

Figure 5.26: I_{off} and RSD of the randomized profile devices with donor interface traps of concentration $p_{\text{it}} = 10^{13}$ cm^{-2}, $E_{\text{it}} = 0.45$ eV. The x axis indicates bulk oxide areal charge concentration.

5.5 Conclusions

The combined effects of Total Ionizing Dose and Random Dopant Fluctuations have been examined in the 45 nm PDSOI MOSFET node. Using the fixed charge method, the highest current density is observed at the bottom silicon corner. Radiation simulations of two-dimensional cuts of the device structure confirm its potential existence as holes are trapped in greater numbers on this corner at the side of the STI. At zero bias, the highest concentration of trapped holes occurs close to the interface of the field oxides with the silicon film. At $V_g = 1$ V, the concentration of trapped holes increases at the bottom of the BOX as well, as a result of the positive gate bias. The areal oxide charge projected at the bottom silicon corner for a uniform trap concentration of 8.2×10^{17} cm^{-3} starts saturating at 100 KRad(SiO_2). The trapped hole density observed is about an order of magnitude less than the value required for parasitic inversion to occur, which shows that the device is extremely hardened against TID. Rounding the bottom silicon corner can reduce the possibility of leakage paths to be formed even further by reducing the magnitude of the electric field.

RDFs were examined using both the Sano and the IFM. The two methods are in good agreement. It was observed that RDFs create significant response deviation but only in post-irradiation results. In pre-irradiation, the contribution of RDFs is minimal. The post-irradiation device response can deviate significantly, and therefore a greater number of measurements needs to be taken into account for the statistical error. RDFs, generally, aggravate post-irradiation response decreasing the dose level at which the device is hardened against. Therefore, the effect is more pronounced at the point of weak inversion of the parasitic transistor.

Interface traps located at the Si/BOX and Si/STI interface only change the device characteristics in the case that they are of donor type. The RDF results using the IFM and interface traps produced the same qualitative results as in the case of bulk charges only. The only difference observed was a shift of the bulk charge required for parasitic channel inversion to occur.

Chapter 6

Total Ionizing Dose simulations of 22 nm bulk nFinFETs

FinFETs have been adopted in commercial state-of-the-art transistor technologies at and beyond the 25 nm gate length as scaling alternatives to partially and fully depleted SOI technologies. In SOI FinFETs, the TID effect has been shown to depend on the geometry of the fin [35, 36], while in bulk FinFET technologies its appearance is attributed mainly to charges gathering in the Shallow Trench Isolation (STI) neck region [125].

In this chapter, TID simulations of a bulk nFinFET model, calibrated to the Intel 22 nm node, are presented. The simulations include bulk charge trapping with the parameters extracted in Chapter 4 using experimental results of 400 nm SiO_2 capacitors fabricated at the University of Southampton.

6.1 Calibration to the Intel 22 nm FinFET node

The nFinFET structure is constructed based on the technology presented in [98]. The process steps are shown in Figure 6.1 and are similar to the Monte Carlo transport simulation model found in [126].

	Auth C.	This work
L_g	30	30
W_{fin} (nm)	8	8
H_{fin}	34	34
EOT (nm)	0.9	0.9 (0.6 SiO_2 + 2 HfO_2)
W_{eff} (nm) ($2\times H_{Si}+W_{Fin}$)	76	76

Table 6.1: Device characteristics for the simulation model and the commercial 22 nm bulk FinFET [98, 127]

The FinFET raised S/D regions are constructed using hexagonal region placement commands. The hexagonal structure results from Selective Epitaxial Growth when the fin is constructed with (110)/<110> orientations. Surface faceting in this case produces diamond-shaped S/D regions [128, 129]. However, the use of the Lombardi model parameters for this orientation, as calibrated in [126] produced many convergence problems in both quasi-stationary and radiation simulations. Therefore, although <110> orientation is assumed for the S/D geometry in sprocess, <100> orientation parametrization is used for carrier transport in sdevice.

The device characteristics are listed in Table 6.1. Important process parameters are shown in Table 6.2. FinFET channels are sometimes left undoped as their shape is mainly responsible for their I_{on}-I_{off} response. A threshold voltage adjustment implant was used here in order to gain better control over the final device characteristics. The complete structure is shown in Figure 6.2.

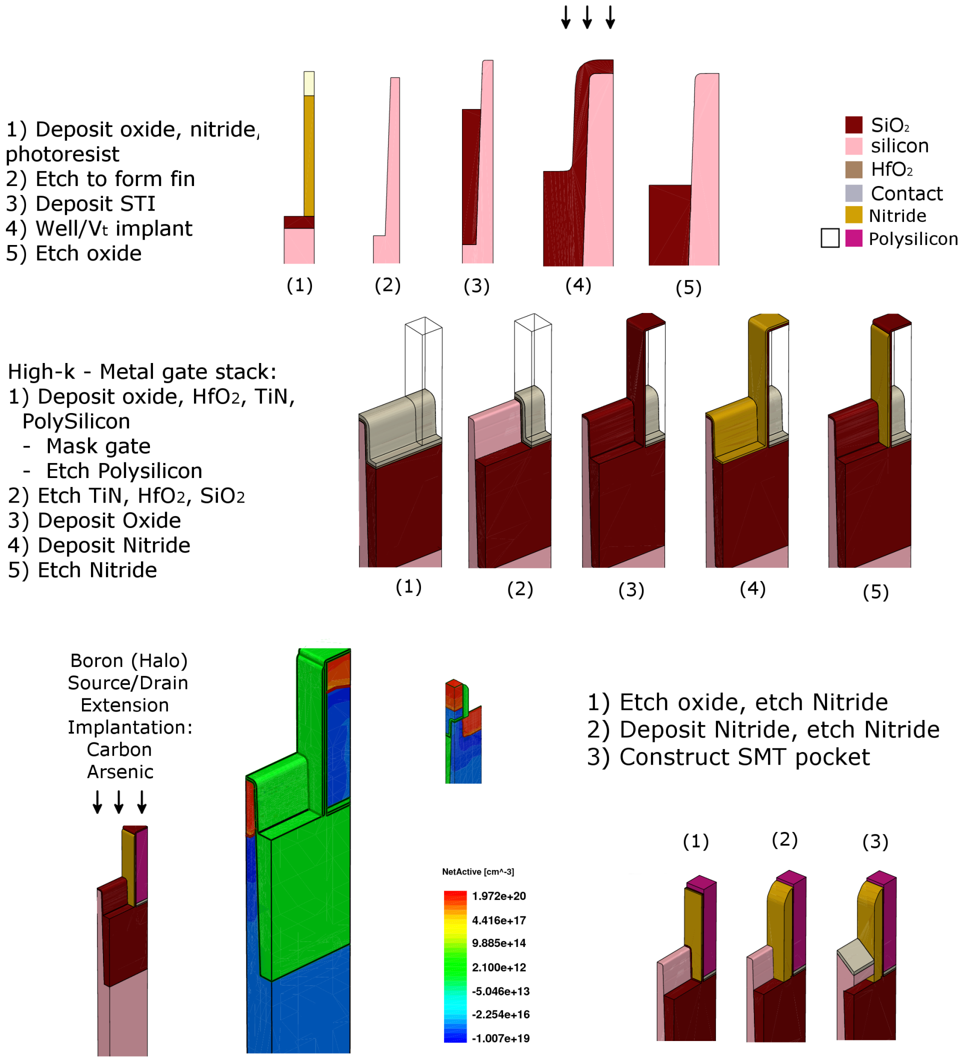

Figure 6.1: 22nm bulk FinFET process steps

The device models used are in accordance to [130]. The Philips Unified mobility model was used inside silicon (Table C.5) with velocity saturation for both electrons and holes, mobility degradation due to the electric field perpendicular to the semiconductor-insulator interface and silicon crystal orientation [100]. The parameters for the *enormaldependence* model are shown in Table C.7. SRH recombination was included with default parameters. Constant DOS mass values for silicon were used, which are for T = 300 K as follows: $m_{el} = 2.971\times10^{19}$ cm^{-3}, $m_h = 2.24\times10^{19}$ cm^{-3}. Constant mobility was also used with $\mu_{maxel} = 1.423\times10^3$ cm^2/Vs and $\mu_{maxh} = 476.07$ cm^2/Vs. The density gradient model was used for electrons only (Table C.8). Table 6.3 lists the device characteristics that resulted from calibrating to the High Performance candidate in [98].

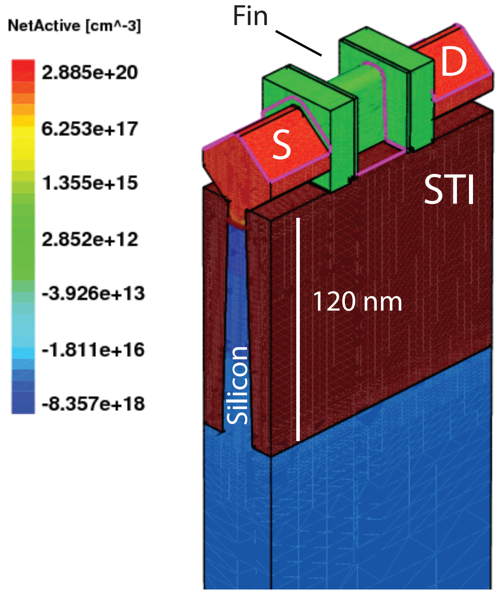

Figure 6.2: Complete structure of the 22 nm bulk FinFET

		Dose (cm^{-2})	Energy(keV)
V_t implant	B	10^{13}	180,60,15
Halo	B	8×10^{12}	5
S/D extension	C	10^{15}	2.5
S/D extension	As	2.5×10^{15}	4
S/D implant	As	5×10^{15}	12

Table 6.2: Process parameters for the simulation model of the 22 nm bulk FinFET

The device was solved in quasi-stationary first in order to observe the transfer characteristics with uniform fixed charges in the STI. This is shown in Figure 6.3. The STI charges cause increase in I_{off}. Inversion of the parasitic transistor starts taking place at an areal charge of 1.3×10^{12} cm^{-2}. At 2.6×10^{12} cm^{-2} and beyond, the FinFET fails to turn off.

The I_{off} increase is due to the inversion of the parasitic channel created in the ‘neck’ region of the fin [39]. The current density in a two-dimensional cut at the middle of

	Jan C.H. et al.	Auth C. et al.	This work
V_{dd} (V)	0.75	0.8	0.8
I_{off} (nA/μm)	100	10	1.72
I_{dSat} (mA/μm)	1.08	1.26	1.29
V_t (V) (V_{ds} = 0.05 V)	0.22	0.18	0.11

Table 6.3: Device parameters for the simulation model and the commercial 22 nm bulk FinFET node [98, 131]

the channel for the case of uniform oxide charge is shown in Figure 6.4. This figure shows the extension of the front-gate channel and subsequent formation of the parasitic channel, provided that adequate holes are trapped in the STI.

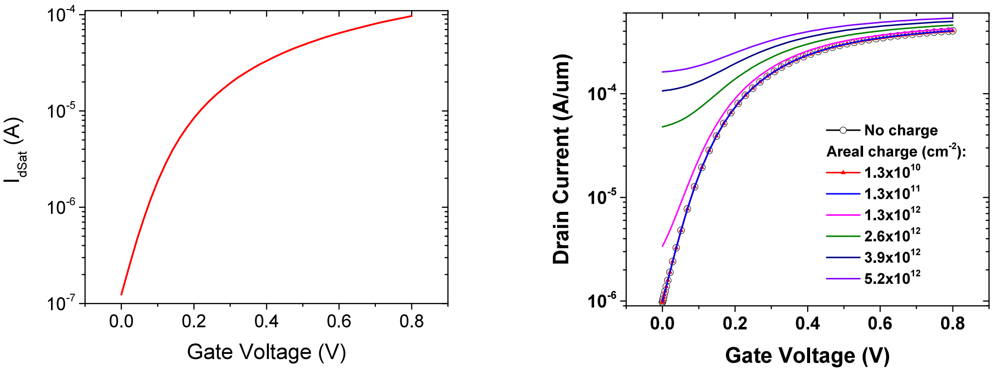

(a) V_{ds} = 0.8 V, No oxide charge

(b) V_{ds} = 0.05 V, fixed oxide charge

Figure 6.3: Simulation I_d - V_g results of the nFinFET. (a) I_{dSat} characteristics and (b) I_{off} increase with increasing areal charge

6.2 Total Ionizing Dose in 22 nm bulk nFinFETs

The same process for simulating TID in the PDSOI MOSFET structure was used here. Specifically, the direct contact of the gate electrode to the STI is defined as Schottky. The electrostatic potential in the two structures (OAO and OASC) is shown in Figure 6.5. In the simulation where the oxide is defined as a dielectric, there is also no direct contact between the STI and the gate electrode. This is the structure that is used in the quasi-stationary simulations producing I-V results. The initial solution of the Poisson equation gave the same results in both cases.

The radiation simulations were performed with a uniform bulk oxide trap density of 8.2×10^{17} cm^{-3} up to two total doses of 500 Krad(SiO_2) and 1 Mrad(SiO_2). The final density of trapped charge in the STI is shown in Figure 6.6. For the unbiased case examined here, the trapped charge is symmetrical on both the Source and Drain sides.

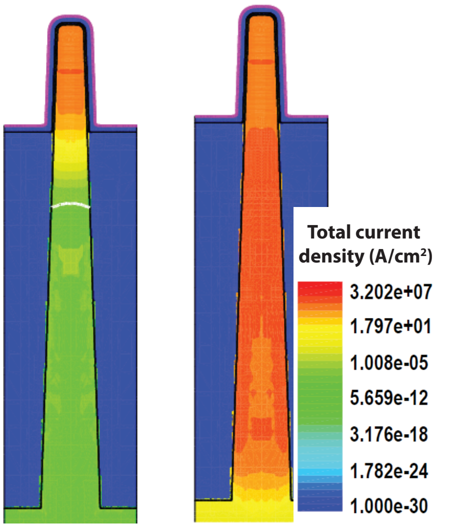

(a) No charge (b) Uniform fixed oxide charge with areal density of 2.6×10^{12} cm^{-2}.

Figure 6.4: Current density in the neck region of the fin. V_g = 0 V, V_{ds}=0.05 V.

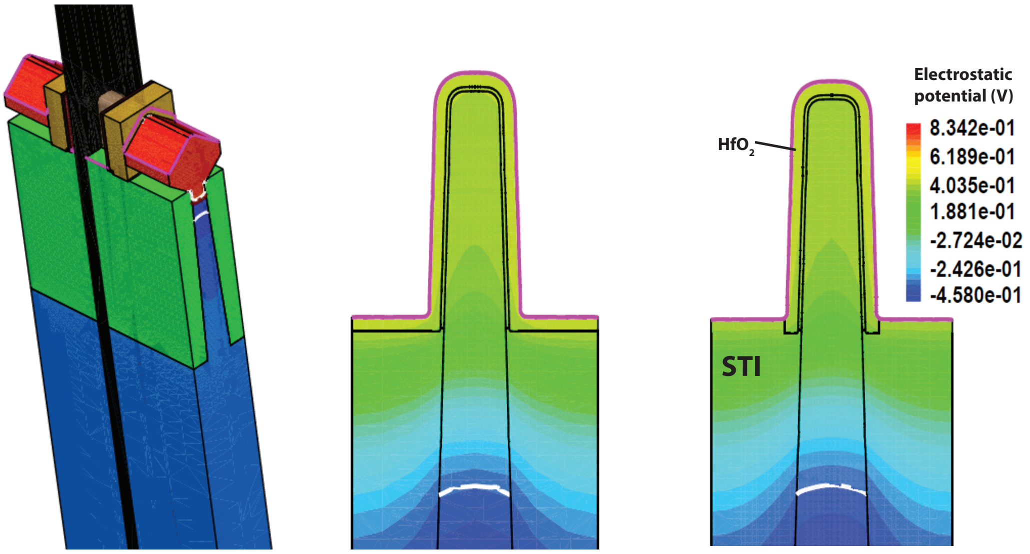

(a) Location of 2D cut (b) Electrostatic potential in OAO (c) Electrostatic potential in OASC

Figure 6.5: Electrostatic potential comparison of FinFET with STI regions defined as OAO and OASC with Schottky contact of the gate to the STI. Shown in (a) is the location of the cut. The legend is common for both figures.

The distribution of the trapped charge follows the electrostatic potential created by the doping concentration in the silicon. This is a result of the electric field in the STI and the path of the holes inside it. The acceptor concentration (inverse of the Net Active concentration in this case) in the silicon region at the neck of the fin as well as the trapped charge in the STI are shown in Figure 6.7. There is a peak of trapped charge 25 nm below the surface of the STI. The negatively charged acceptor atoms attract holes towards that location. The trapped charge density is increased as the path length of the holes increases since the flux of the holes is higher closer to the interface.

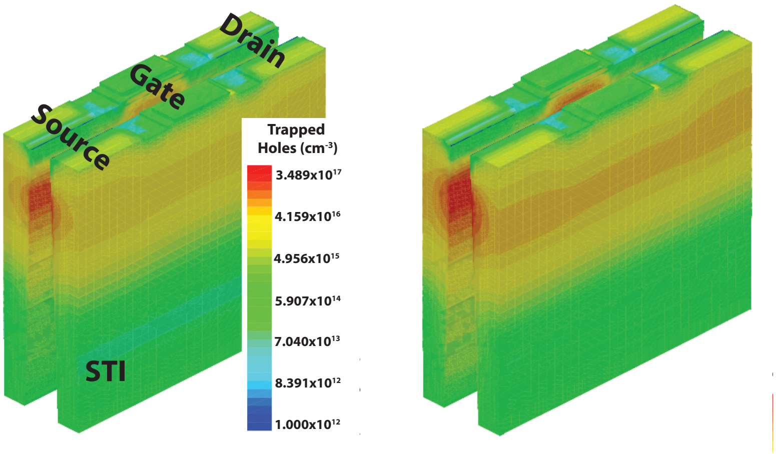

(a) 500 KRad(SiO_2) (b) 1 MRad(SiO_2)

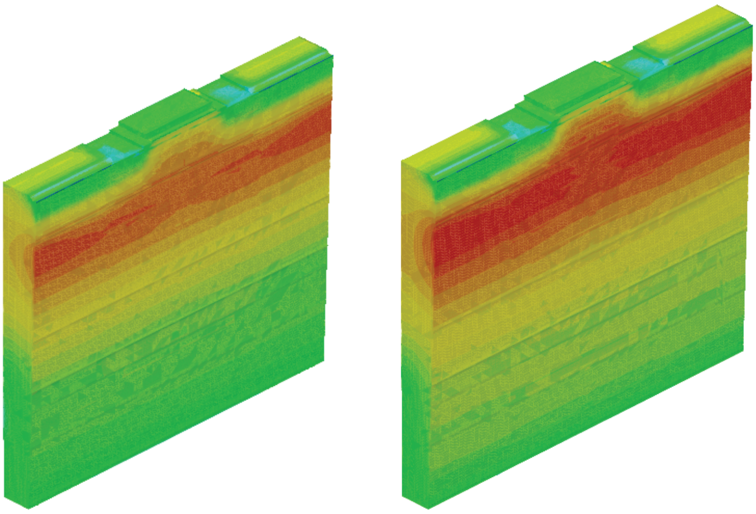

(c) 500 KRad(SiO_2) (d) 1 MRad(SiO_2)

Figure 6.6: Trapped charge density in the STI in the nFinFET irradiated unbiased up to two total doses as indicated below each figure. The gradient is common for all figures. Shown at the top are both sides of the STI and at the bottom only one side. The density is symmetrical for the unbiased case. The legend is common in all cases.

The density of the trapped holes as a function of distance from the Si/STI interface 25 nm from the surface of the STI (at the location of the peak) is shown in Figure 6.8. From this data, we extract the areal trapped charge of 3.64×10^{10} cm^{-2} at 500 kRad(SiO_2) and 6.1×10^{10} cm^{-2} at 1 MRad(SiO_2). Both of these values reveal an areal density that is not enough to invert the parasitic transistor channel as was found in the fixed oxide charge simulations in Figure 6.3(b).

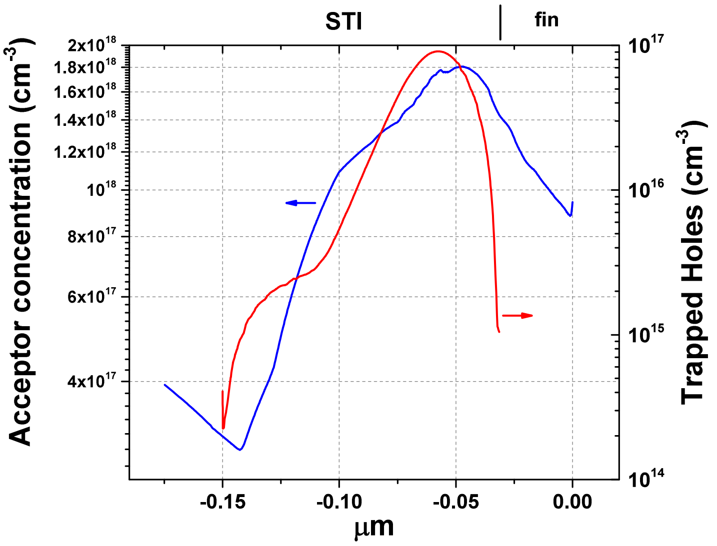

Figure 6.7: Acceptor concentration in the neck of the fin and trapped charge concentration in the STI.

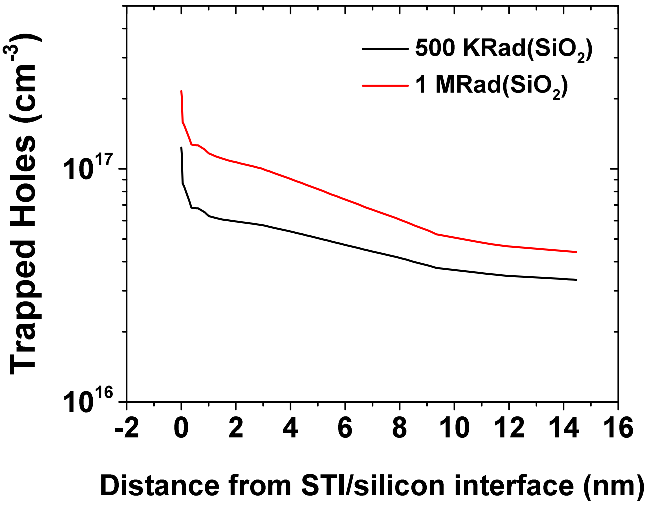

Figure 6.8: Trapped charge density as a distance from the Si/STI interface 25 nm below the surface of the STI.

6.3 Conclusions

The simulation methodology presented in Chapter 4 was used here to simulate TID effects in a 22 nm bulk nFinFET calibrated to the Intel node. Using the fixed charge method, onset of inversion of the parasitic transistor is found to occur at an areal charge of $\approx 1.3\times10^{12}$ cm^{-2}. The positive trapped charge found in the radiation simulations in the unbiased case shows a peak 25 nm below the surface of the STI. This revealed the depth at which the S/D parasitic channel will have in the neck region of the fin. The areal charge measured after irradiation simulations at that location using the 'image charge' method with a bulk trap density of 8.2×10^{17} cm^{-3} is more than an order of magnitude less than the value required for parasitic channel inversion. We conclude that the nFinFET technology examined here shows increased hardness against TID effects.

Chapter 7

Conclusions and future work

Total Ionizing dose effects have been systematically simulated using Synopsys Sentaurus. Calibration was performed to experimental results in 400 nm SiO_2 capacitors. The physics involved have been explained in detail. Adjustments to the normal device operation had to be made to properly account for carrier transport and trapping in the oxide regions. The carriers generated in the oxide were able to escape either through a direct contact of the oxide with the metal or through thermionic emission enabled at the Si/SiO_2 interface. This systematic method was subsequently used in two state-of-the-art FET technologies, namely, the 45 nm PDSOI nMOSFET and the 22 nm bulk nFinFET. These were calibrated to experimental results of the IBM and Intel nodes respectively.

In the case of the PDSOI, the location of the leakage path using the fixed charge method was identified to be the bottom Si corner of the active volume. Using two-dimensional simulations of slices of the device, the highest concentration of trapped charge at the side of the oxide was found to occur at this same corner, confirming the existence of the leakage path at this location. The dependency of the distribution of the trapped charge to the gate bias was checked by irradiating the device under different bias conditions. The trapped charge was higher at the interface of the Si with the STI in the unbiased case, while for the cases where the gate was biased at V_{dd}, the trapped holes density increased at the bottom of the BOX as well. Finally, three-dimensional simulations of interface traps located at the Si/STI and Si/BOX boundaries showed an increase in I_{off} in the case that they were of donor type.

TID simulations were also performed on three-dimensional FinFET structures. The trapped charge after irradiation under zero bias showed a peak about 25 nm from the STI surface. This is a result of the electric field in the oxide created by the doping distribution in the silicon. It is therefore expected to be subject to different implantation schemes in the device, or in the case where the fin channel is left undoped, by the S/D implant potential. Irradiation with the transistor biased in the on state (V_{dd} = 0.8 V) would exhibit a peak in the trapped holes density even further in the STI bulk.

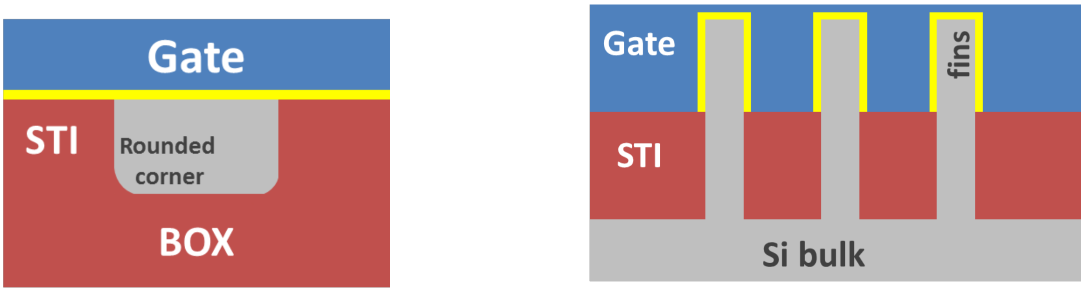

(a) Cross section of optimized geometry of the PDSOI MOSFET structure. The cut is taken parallel to the gate.

(b) Tri-gate FinFET transistor structure followed by Intel [98, 132].

Figure 7.1: Cross section of devices with increased radiation hardness

The higher the depth of the trapped holes, the more protected the device would be to forming leakage paths as the electrons would have to find a suitable route from the drain to the source. The radiation simulations performed showed that the areal trapped charge projected at the interface of the Si with the field isolation in the FinFET was about one order of magnitude lower than that required for parasitic inversion based on three-dimensional fixed charge simulations.

Overall, both technologies examined have showed an increased inherent resistance to TID-induced changes of their characteristics making them very suitable for applications in which ionizing radiation is most prominent in the environment. For the case of the PDSOI, it is predicted that rounding the bottom Si corner of the top film can further produce devices of increased TID-hardness (Figure 7.1(a)). This is due to the location of the leakage path found in section 5.2. Rounding the bottom silicon corner can reduce the intensity of the electric field, thereby reducing the level of electron current.

For the case of the FinFET, the existence of the lateral gates gives very good electrostatic

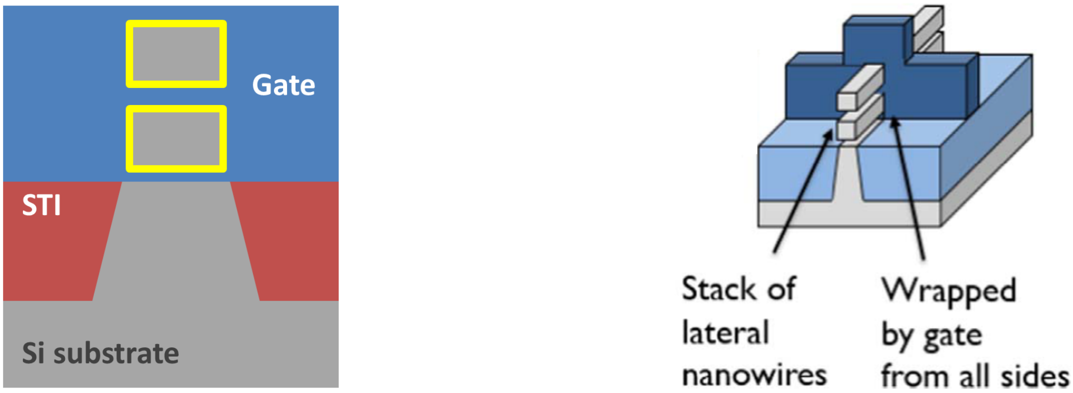

(a) Cross section of GAA NWFET of stacking type

(b) 3D view of GAA NWFET [133, 134]

Figure 7.2: Geometry of GAA NWFETs with Si, SiGe and Ge stacks

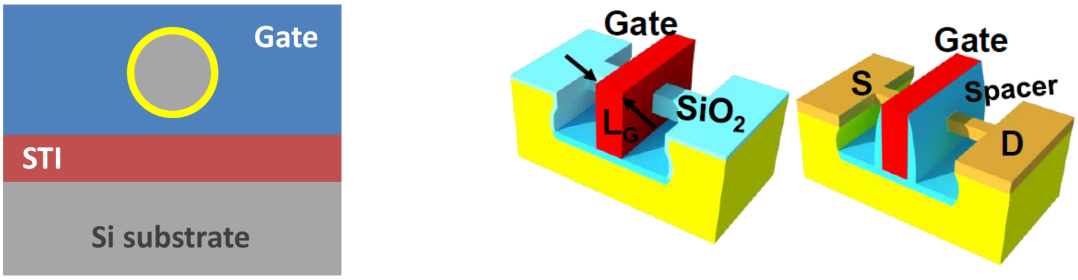

(a) Cross section of a generic GAA NWFET

(b) 3D view of SiNW GAA FETs [135]

Figure 7.3: Geometry of GAA NWFETs

control of the silicon fin. Therefore, bulk structures that have no BOX, show increased TID-hardness. Particularly, the tri-gate structure can create an environment where the middle fin is especially protected from trapped charge collection at its STI sides in the neck region (Figure 7.1(b)) reducing the possibility of contribution to the off-state current. Any contribution of the trapped charge in the STI is likely to occur from the outer isolation regions of the side fins.

This contribution is entirely eliminated in Gate-all-Around (GAA) NWFETs which are considered the ultimate scaling of FinFETs (Figure 7.2) [133, 134]. Particularly, the bulk devices shown in this figure in which the stacking materials (nanowires) are epitaxially grown on silicon are considered more robust than their SOI counterparts. The nanowires can be made of Si, SiGe or Ge and they are completely surrounded by the gate eliminating any contribution of charge trapped in the thick isolation region to the electrostatic control of the channel.

Alternatively, one suspended Si NW could be used as shown in Figure 7.3. This configuration has also been examined for its increased resistance to TID effects by the NASA Ames Research Center [135]. This wrapped SiNW channel provides increased performance and robust $I_{\text{on}}/I_{\text{off}}$ ratios.

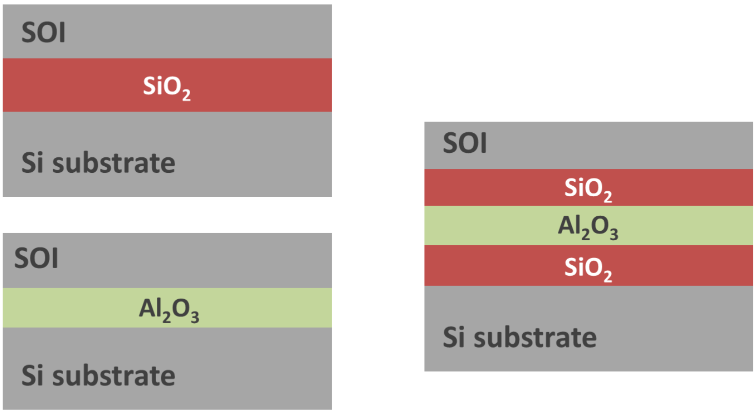

Figure 7.4: UTBOX SOI architectures with SiO_2 and Alumina BOX [136]

The other scaling direction to the FinFET is the FDSOI architecture in which the BOX has been significantly reduced to widths comparable of gate dielectrics (Figure 7.4). The FDSOI can significantly reduce variability, while the thin BOX insulating layer is protected from accumulating positive charges due to tunnelling effects and the small charge collection length (small path length of the carriers). The BOX materials can be either SiO_2, but also Al_2O_3 have been presented. In this latter case, negative fixed charges introduced in the BOX during fabrication can cancel out the positive charges gathered through irradiation, while it was shown that it is possible to control their density through careful design of the BOX deposition [136].

The ITRS [137] predicts that the FinFET will continue to be the CMOS workhorse down to 7nm scales. Commercial FPGAs that incorporate hardened FinFET transistors such as the Intel 22nm tri-gate ([138]) are very attractive solutions for the expanding space electronics market.

For the technologies studied in this work, TID simulations were combined with doping fluctuation simulations in the 45 nm PDSOI MOSFET node. In this case, I_{off} increase of the device was observed, while the RDFs contribution was more significant at the point of weak inversion of the parasitic transistor, where the highest σI_{off} was recorded. It could be of interest to examine how RDFs would affect the TID response of the nFinFETs. However, this is only applicable for the cases where doping is included in the experimental transistors. Generally, fully depleted devices, in which RDFs do not pose a risk, are expected to provide robust, scaled alternatives for TID-hardened transistors.

Extension of the bulk trapping model to include formation of interface states using state transitions has also been discussed. The model in this case includes transport of hydrogen that is uniformly spread throughout the oxide and can further be expanded to include hydrogen release from hole trapping sites within the oxide. The interface states are de-passivated through capturing a proton at the interface and releasing a hydrogen molecule, while their passivation occurs either by H_2, or H^+ capture. Using state transitions, a full treatment of TID effects can be made, taking into account situations where interface trap formation becomes important to device characteristics.

Generally, the TCAD/device simulation option can offer many advantages in producing very accurate results through the Finite Elements Method which is more detailed and versatile than the analytical approach. Anisotropic electronic structure of SiO_2 as well as a non-uniform distribution of traps can all be added to the simulation model. As we approach nano dimensions, the scales gradually require quantum effects to be more accurately simulated. This creates the need for multi-scale simulations of nano-transistors such as NW and 2D semiconductor FETs [100, 139]. Thick oxides continue to exist in such devices providing isolation from the substrate. In these cases, the same principles to TID apply. At the same time, ab-initio and DFT simulations continue to provide details on the FEM system parametrization. Ab-initio simulations will also be required in order to gain insight in the microscopic nature of traps located at the channel interfaces with the isolation oxides in more advanced transistor technologies such as 2D semiconductor FETs [140].

The only drawback to the FEM approach is the increased technical difficulty inherent to such numerical techniques (i.e. achieving convergence can sometimes be time-consuming). This situation could potentially change in smaller dimensions as the number of elements is reduced and it becomes easier to identify and fix bad elements. It is therefore evident that FEM simulators will continue to be tools essential to the device designer of state-of-the-art and future transistor technologies.

Appendix A

Bug work-around in Sentaurus mesh

There is a bug in the Sentaurus Mesh randomization functionality when using the Sano method. Randomization creates positive voltage shifts, which are not in accordance to the theory which states that there is a threshold voltage lowering as a result of the percolation paths created in the transistor channel [123, 124]. This increase in the threshold voltage is shown in Figure A.1.

To overcome this issue, we extracted the Net Active and Boron Active concentrations from 1D cuts in the transistor as shown in Figure A.2. The 1D doping profiles for the device with Uniform doping and that after randomization are shown in Figure A.3. The cuts were chosen such that the results were as much as possible inside the front and "sidewall" channels of the device. The location of the cuts is given in Table A.1.

Cut A	(x_1, y, z_1) (x_2, y, z_2) (μm)
A1	(0.0120, -0.0018, 0.0090) (0.0120, -0.0018, 0.0950)
A2	(0.0400, -0.0018, 0.0090) (0.0400, -0.0018, 0.0950)
Cut B	(x_1, y_1, z) (x_2, y_2, z) (μm)
B1	(0.0020, -0.0120, 0.0106) (0.0020, 0.0120, 0.0106)
B2	(0.0400, -0.0120, 0.0106) (0.0400, 0.0120, 0.0120)

Table A.1: Location of the cuts taken in Figure A.2.

After randomization, a significant increase in the Net Active concentration was observed (about half an order of magnitude), in contrast to the Boron active concentration, whose level remained close to the uniform concentration. The integral of the doping concentrations throughout the whole 3D volume was also extracted and shown in Table A.2.

To change this situation, a tdx script was devised in Sentaurus workbench that increases the amount of the Net active concentration dataset by a constant number. This number

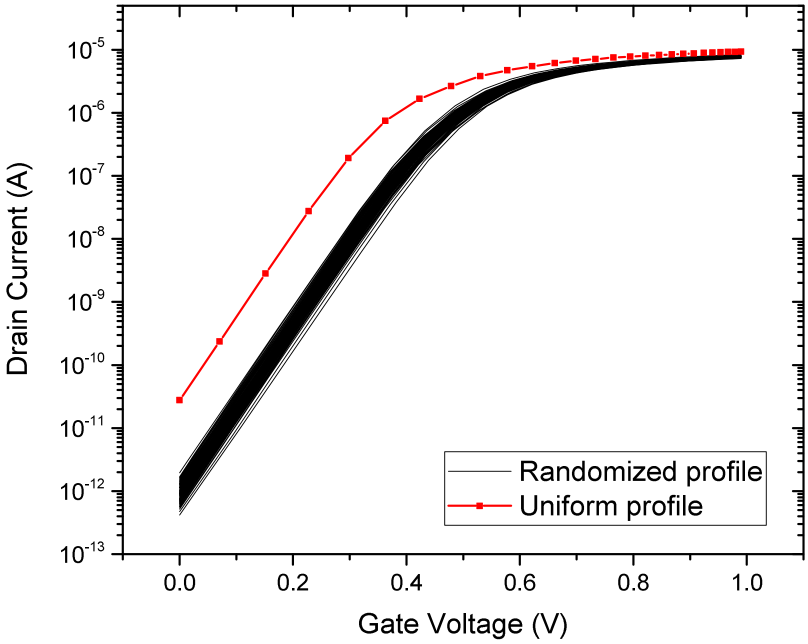

Figure A.1: $I_d - V_g$ results for randomized doping profile with no adjustment of the doping concentration after randomization. Comparison is with the uniform profile.

	Net Active (cm^{-3})	Boron Active (cm^{-3})
Uniform doping	-4.638×10^{18}	4.638×10^{18}
Randomized doping	-9.405×10^{17}	4.767×10^{18}

Table A.2: Integral of volume doping concentration in cm^{-3}

was chosen by calibrating the I_d-V_g results, as shown in Figure A.4. The final number that was chosen is 4.2×10^{18} cm^{-3}.

The integral of the Net active concentration after the script, is shown in Table A.3. The net active concentration at the 1D cuts compared to the Boron active concentration at the same location is shown in Figure A.5. In this figure, the NetActive concentration dataset was multiplied by -1 for ease of comparison.

	Net Active (cm^{-3})	Boron Active (cm^{-3})
Randomized doping plus add. const. in NetActive	-5.200×10^{18}	4.767×10^{18}

Table A.3: Integral of volume doping concentration in cm^{-3}

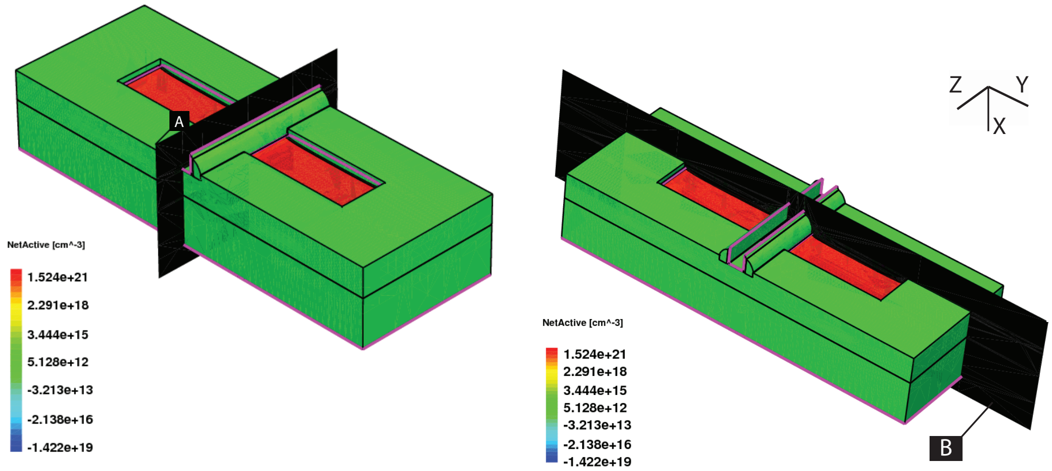

(a) 2D Cut A (b) 2D Cut B

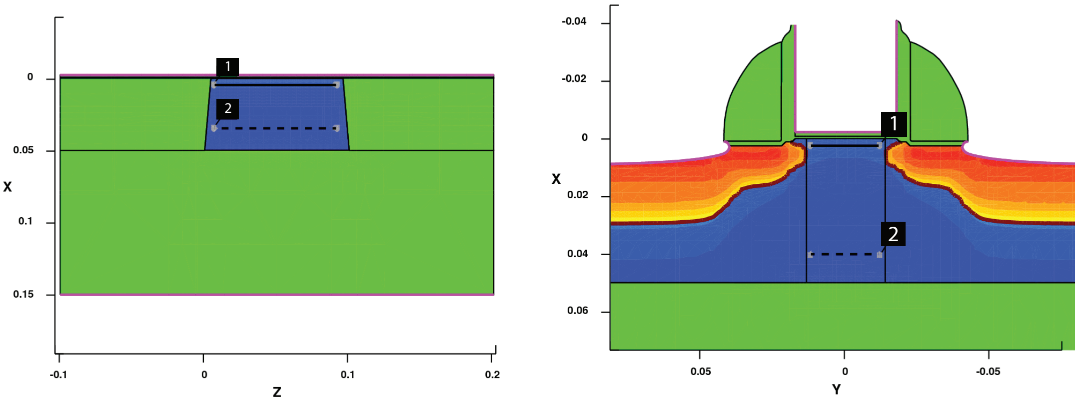

(c) 1D Cut 1 and 2 (d) 1D Cut B1 and B2

Figure A.2: Location of the cuts from which the doping concentration was taken.

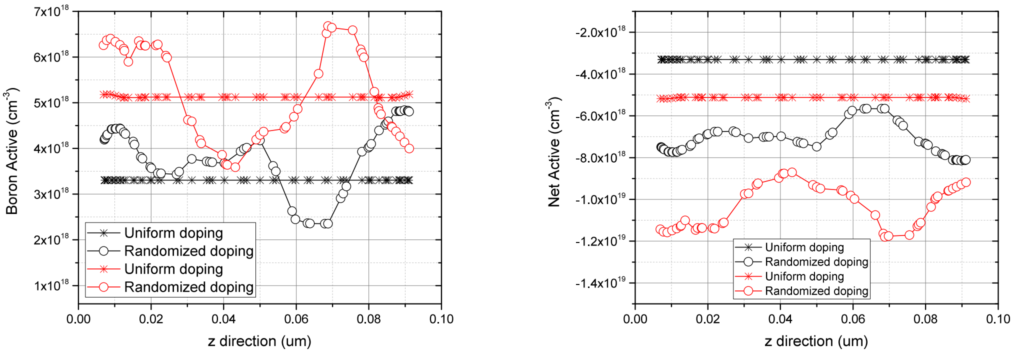

(a) Boron active concentration, Cut A1 and A2

(b) Net active concentration, Cut A1 and A2

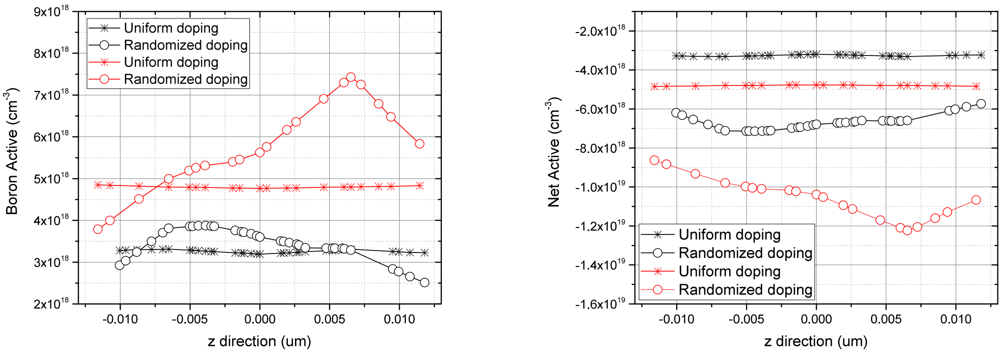

(c) Boron active concentration, Cut B1 and B2

(d) Net active concentration, Cut B1 and B2

Figure A.3: Shown in black is Cut A1/B1 and shown in red is A2/B2

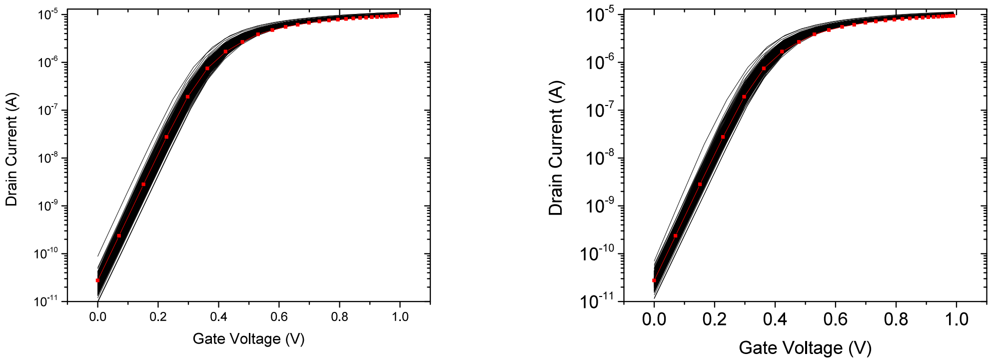

(a) Constant added: 3.7×10^{18} cm^{-3}

(b) Constant added: 3.8×10^{18} cm^{-3}

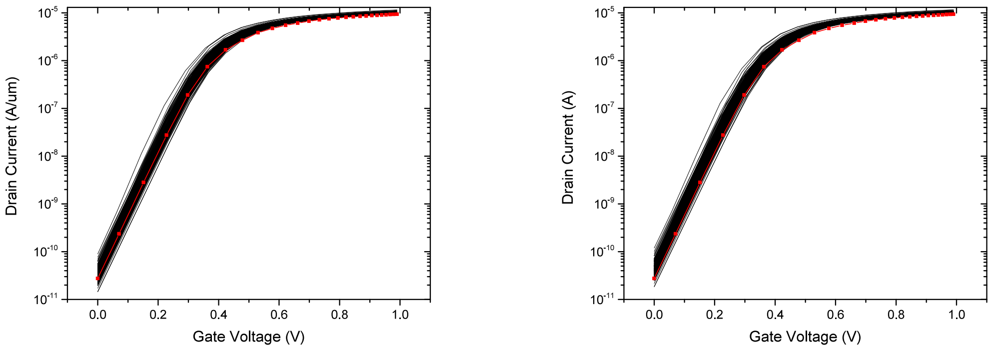

(c) Constant added: 4×10^{18} cm^{-3}

(d) Constant added: 4.2×10^{18} cm^{-3}

Figure A.4: Shown in black are the I-V results of the devices with the randomized profiles and in red dotted, the results of the device with the uniform profile.

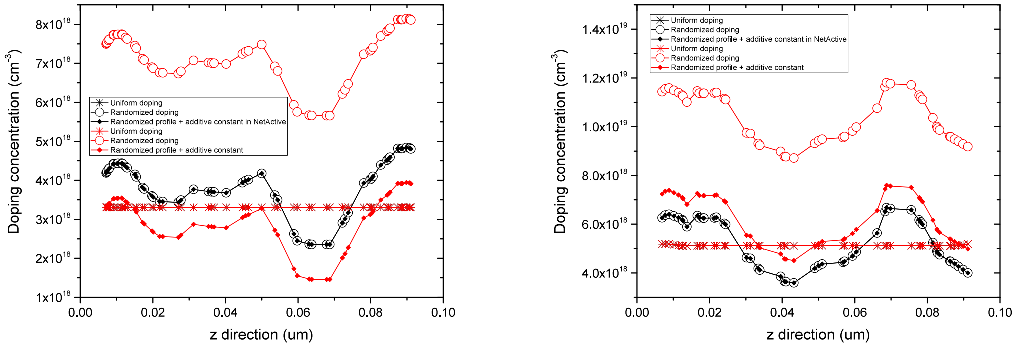

(a) Cut A1 (b) Cut A2

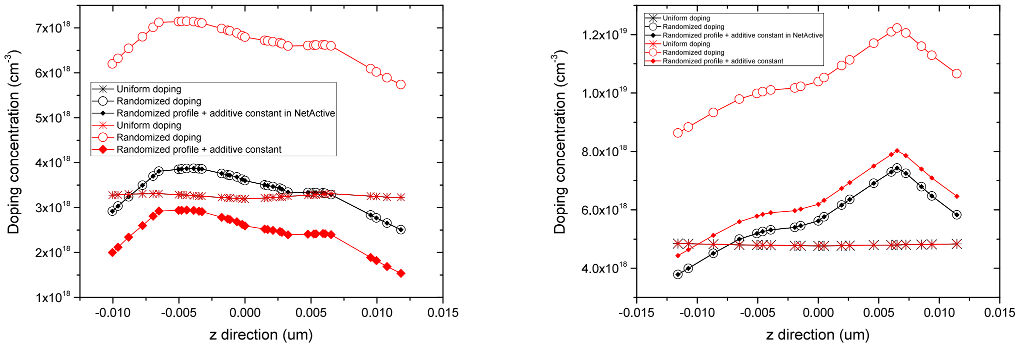

(c) Cut B1 (d) Cut B2

Figure A.5: Shown in black is Boron active concentration and shown in red is Net active concentration

Appendix B

Long-range Coulomb potential

The electric potential density of N acceptor atoms in real space can be represented by their delta functions times the atoms charge,

$$\rho\left(r\right) = -q\sum_{i=1}^{N}\delta\left(r - r_i\right) \tag{B.1}$$

Where r_i is the location of the i$^{\text{th}}$ atom.

Using the atom's wave representation, the density becomes,

$$\rho\left(r\right) = -q\sum_{i=1}^{N}\frac{1}{V}\sum_{k<k_c}\mathrm{e}^{ik\cdot(r-r_i)} - q\sum_{i=1}^{N}\frac{1}{V}\sum_{k>k_c}\mathrm{e}^{ik\cdot(r-r_i)} \tag{B.2}$$

For every factor in the RHS, the first sum is for all atoms, while the second is for the range of k values. kc is called the screening length and is used to discriminate between the short range and long range interactions. The short range interactions ($k<k_c$) are thought to be lost in scattering events, and therefore only the long range Coulomb potential ($k>k_c$) is taken into account for the doping density of the randomized acceptor profile.

Therefore, only taking into account the long range part of the Coulomb potential, the number density of one acceptor atom located at the origin (r_i = 0) is [93],

$$\rho\left(r\right) = \frac{k_\mathrm{c}^2}{2\pi^2}\frac{\sin\left(k_\mathrm{c}r\right) - \left(k_\mathrm{c}r\right)\cos\left(k_\mathrm{c}r\right)}{\left(k_\mathrm{c}r\right)} \tag{B.3}$$

Integrating the density in three dimensions,

$$\iiint \rho\left(r\right)\mathrm{d}r^3 \tag{B.4}$$

Since (B.3) is isotropic, and subsequently defined in spherical coordinates, we substitute $dr^3 = r^2 \sin\theta dr d\theta d\phi$ and the integral becomes,

$$4\pi \int r^2 \frac{k_\mathrm{c}^2}{2\pi^2} \frac{\sin(k_\mathrm{c}r) - (k_\mathrm{c}r)\cos(k_\mathrm{c}r)}{(k_\mathrm{c}r)} \mathrm{d}r \tag{B.5}$$

solving for the range 0<$k_c r$<4.4934,

$$\frac{2}{\pi} \left[\mathrm{Si}(k_c r) - \sin(k_c r)\right]_0^{\frac{4.4934}{k_c}} = 1.67539 \tag{B.6}$$

Sentaurus mesh includes a normalization factor N_f which is multiplied by (B.3) and assures 100% of the number density of the dopant atom is kept inside the active volume where the profile is randomized. This is especially useful for the atoms that are close to the boundaries. In the case where the number density of the atom is cut-off inside the volume, N_f takes the value of 0.59688 [94]. In other words,

$$N_\mathrm{f} \frac{k_c^2}{2\pi^2} \frac{\sin(k_\mathrm{c}r) - (k_\mathrm{c}r)\cos(k_\mathrm{c}r)}{(k_\mathrm{c}r)} = 0.59688 \times 1.67539 = 1 \tag{B.7}$$

Appendix C

Transistor parameters

C.1 PDSOI MOSFET parameters

Scharfetter model parameters			
Parameter	Electron	Hole	Unit
T_{max}	10^{-6}	10^{-6}	s
N_{ref}	10^{17}	10^{17}	cm^{-3}

Table C.1: PDSOI parameters for SRH recombination lifetimes

Lombardi_highk model

The *Enormal* set of models accounts for mobility degradation at gate Si/SiO$_2$ interface due to carrier scattering by acoustic surface phonons and surface roughness and surface roughness.

In the Lombardi_highk model, the surface contribution due to acoustic phonons is given by,

$$\mu_{ac} = \frac{B}{F_\perp} + \frac{C\left(\left(N_{A,0} + N_{D,0} + N_2\right)/N_0\right)^\lambda}{F_\perp^{1/3}\left(T/300K\right)^k} \tag{C.1}$$

The contribution due to surface roughness is,

$$\mu_{sr} = \left(\frac{\left(F_\perp/F_{ref}\right)^{A*}}{\delta} + \frac{F_\perp^3}{\eta}\right)^{-1} \tag{C.2}$$

The mobilities are combined together using Mathiessen's rule,

$$\frac{1}{\mu} = \frac{1}{\mu_b} + \frac{D}{\mu_{ac}} + \frac{D}{\mu_{sr}} \tag{C.3}$$

where

- $N_{D,0}$ and $N_{A,0}$ are the net donor and acceptor concentrations
- μ_b is the bulk mobility
- $D=\exp(-x/l_{crit})$
- x is the distance from the interface

and

$$A^* = A + \frac{(\alpha_{\perp,n} n + \alpha_{\perp,p} p)\, N_{ref}^{\nu}}{(N_{A,0} + N_{D,0} + N_1)^{\nu}} \tag{C.4}$$

- n is the electron concentration
- p is the hole concentration
- For electron mobility, $\alpha_{\perp,n}=\alpha_{\perp}$ and $\alpha_{\perp,p}=0$
- For hole mobility, $\alpha_{\perp,n}=0$ and $\alpha_{\perp,p}=\alpha_{\perp}$

The parameters for the models used in the mobility model are shown in Table C.2. Missing values are set as the default for silicon.

E normal dependence			
Enormal model coefficient	Electrons	Holes	Unit
B	3.61×10^{7}	1.51×10^{7}	cm/s
C	1.7×10^{4}	4.18×10^{3}	$\mathrm{cm}^{5/3}/(\mathrm{sV}^{2/3})$
λ	0.0233	0.0119	
κ	1.7	0.9	
Δ	3.58×10^{18}	4.1×10^{15}	V/s
A	2.58	2.18	
α	2×10^{-20}	3×10^{-20}	
ν	0.0767	0.123	
l_{crit}	1	1	cm
Lombardi highk model coefficients			
B	3.61×10^{7}	1.51×10^{7}	
C	1.7×10^{4}	4.18×10^{3}	
λ	0.0233	0.0119	
κ	1.7	0.9	
δ	3.58×10^{18}	4.1×10^{15}	
A	2.58	2.18	
α	6.85×10^{-21}	7.82×10^{-21}	
ν	0.0767	0.123	
η	10^{50}	10^{50}	
l_{crit}	10^{-6}	10^{-6}	

Table C.2: PDSOI parameters for enormaldependence model in silicon

Parameter	Symbol	Electrons	Holes	Unit
Energy relaxation time	τ_{w}	-	0.3	ps
HighFieldMob	K_{dT}	10^{-4}	10^{-4}	

Table C.3: PDSOI energy-dependent parameters

C.2 FinFET parameters

Bandgap parameters

$$E_g = E_g(0) \tag{C.5}$$

Parameter	Value	Unit
$\chi(0)$	4.05	eV
$E_g(0)$	1.12	eV

Table C.4: FinFET bandgap parameters

Energy relaxation time		
Parameter	Value	Unit
$\mu_{\text{max\_As}}$	1.423×10^3	cm^2/Vs
$\mu_{\text{min\_As}}$	55.9	cm^2/Vs
$\mu_{\text{max\_P}}$	1.423×10^3	cm^2/Vs
$\mu_{\text{max\_B}}$	476.070	cm^2/Vs

Table C.5: FinFET Philips Unified mobility model parameters for silicon

High field dependence		
Parameter	Electrons	Holes
β_0	1.109	1.213
$v_{\text{sat},0}$	1.02×10^7	8.37×10^6

Table C.6: FinFET velocity saturation parameters for silicon

EnormalMob model

The mobility models used for the FinFET obey the equations (C.1) - (C.3). The parameters are shown in Table C.7.

EnormalMob			
Parameter	Electrons	Holes	Unit
B	3.61×10^{7}	1.51×10^{7}	cm/s
C	1.7×10^{7}	4.18×10^{3}	$cm^{5/3}/V^{2/3}s$
λ	0.0233	0.0119	
δ	3.58×10^{18}	4.1×10^{15}	V/cm
A	2.58	2.18	
α	6.85×10^{-21}	7.82×10^{-21}	cm^{-3}
ν	0.0767	0.123	
η	10^{300}	10^{300}	$V^2/cm\cdot s$
Lombard_highk			
B	1.355×10^{7}	5.65×10^{6}	cm/s
C	7650	3344	$cm^{5/3}/V^{2/3}s$
λ	0.0233	0.0119	
k	1	1	
δ	3.58×10^{18}	4.1×10^{15}	V/cm
A	2.58	2.18	
α	6.85×10^{-21}	7.82×10^{-21}	cm^{-3}
ν	0.0767	0.123	
η	10^{300}	10^{300}	$V^2/cm\cdot s$
l_{crit}	10^{-6}	10^{-6}	cm
α_{rcs}	0	0	
α_{rps}	0	0	

Table C.7: Parameters for enormaldependence model for [100] orientation of the crystal structure

Density gradient quantum transport		
Parameters	Electrons	Holes
Weighting factor for quantum potential, γ	3.6	10.0
Weight for quadratic term, θ	0.5	0.5
Weight for quasi Fermi potential, χ	1	1
Weight for electrostatic potential, η	1	1
ν	0	0

Table C.8: Density gradient quantum transport

References

[1] Zell Holly. NASA's SDO Sees Massive Filament Erupt on Sun, 2013. URL `http://www.nasa.gov/mission/pages/sunearth/news/News090412-filament.html`.

[2] W. Q. Lohmeyer and K. Cahoy. Space weather radiation effects on geostationary satellite solid-state power amplifiers. *Space Weather*, 11(8):476–488, 2013. ISSN 15427390. doi: 10.1002/swe.20071.

[3] K.L. Bedingfield, R.D. Leach, and M.B. Alexander. Spacecraft system failures and anomalies attributed to the natural space environment. *NASA Reference Publication 1390*, (August):51, 1996. doi: doi:10.2514/6.1995-3564.

[4] V. Zoita, S. Soare, T. Craciunescu, M. Curuia, V. Kiptily, N. Balshaw, P. Blanchard, D. Croft, A. Murari, and B. Syme. Definition of the radiation fields for the JET gamma-ray spectrometer diagnostics. *Fusion Engineering and Design*, 88(6-8): 1366–1370, 2013. ISSN 09203796. doi: 10.1016/j.fusengdes.2013.01.083.

[5] R. Hull, J. Millard, and H. Brunnader. Development of radiation hardened electronics. In *The 2nd international conference on CANDU maintenance*, 1992.

[6] C. Leroy and P. G. Rancoita. *Principles Of Radiation Interaction In Matter And Detection*. World Scientific Publishing Company, 2nd edition, 2009.

[7] B. T. Pemberton. *A structured ASIC approach to a radiation hardened by design digital single sideband modulator for digital radio frequency memories*. PhD thesis, Wright State University, 2008.

[8] Microsemi®. FPGA Reliability and the Sunspot Cycle. Technical Report September, 2011.

[9] J. L. Leray. Total Dose Effects: Modeling for present and future. In *IEEE Nuclear and Space Radiation Effects Conference Short Course*, chapter III, pages III–1 – III–4. IEEE publishing, 1999.

[10] synopsys Inc. Sentaurus Device User Guide. 2015.

[11] B. Y. Nguyen, C. George, and M. Carlos. A Review of SOI Technology and its Applications. *Journal Integrated Circuits and Systems*, pages 51–54, 2009.

[12] F. El-Mamouni, E. X. Zhang, N. D. Pate, N. Hooten, R. D. Schrimpf, R. A. Reed, K. F. Galloway, D. Mcmorrow, J. Warner, E. Simoen, C. Claeys, A. Griffoni, D. Linten, and G. Vizkelethy. Laser- and Heavy Ion-Induced Charge Collection in Bulk FinFETs. *IEEE Transactions on Nuclear Science*, (December):2563–2569, 2011.

[13] R. D. Schrimpf, D. M. Fleetwood, M. L. Alles, R. A. Reed, G. Lucovsky, and S. T. Pantelides. Radiation effects in new materials for nano-devices. *Microelectronic Engineering*, 88(7):1259–1264, July 2011. ISSN 01679317. doi: 10.1016/j.mee.2011.03.117.

[14] N. Seifert, B. Gill, S. Jahinuzzaman, J. Basile, V. Ambrose, Q. Shi, and R. Allmon. Soft Error Susceptibilities of 22 nm Tri-Gate Devices. (December):2666–2673, 2012.

[15] L. Gonella, F. Faccio, M. Silvestri, S. Gerardin, D. Pantano, V. Re, M. Manghisoni, L. Ratti, and A. Ranieri. Total Ionizing Dose effects in 130-nm commercial CMOS technologies for HEP experiments. *Nuclear Instruments and Methods in Physics Research Section A: Accelerators, Spectrometers, Detectors and Associated Equipment*, 582(3):750–754, December 2007. ISSN 01689002. doi: 10.1016/j.nima.2007.07.068.

[16] N. Rezzak. *The Effect of Shallow Trench Isolation (STI) Topology, Sidewall Doping and Layout-related Stress on Radiation-induced Leakage Current*. PhD thesis, University of Vanderbilt, 2010.

[17] N. Rezzak and R. D. Schrimpf. Layout-related stress effects on radiation-induced leakage current. *IEEE Transactions on Nuclear Science*, 57(6):3288–3292, 2010.

[18] Y. Li, N. Rezzak, E. X. Zhang, R. D. Schrimpf, D. M. Fleetwood, J. Wang, and D. Wang. Including the Effects of Process-Related Variability on Radiation Response in Advanced Foundry Process Design Kits. *IEEE Transactions on Nuclear Science*, 57(6):3570–3574, 2010.

[19] N. Rezzak, E. X. Zhang, and D. R. Ball. Total-ionizing-dose radiation response of 32 nm partially and 45 nm fully-depleted SOI devices. In *IEEE International SOI Conference*, pages 31–32, 2012. ISBN 9781467326919.

[20] M. F. Bukhori, S. Roy, and A. Asenov. Simulation of statistical aspects of charge trapping and related degradation in bulk MOSFETs in the presence of random discrete dopants. *IEEE Transactions on Electron Devices*, 57(4):795–803, 2010.

[21] K. J. Kuhn. Reducing Variation in Advanced Logic Technologies: Approaches to Process and Design for Manufacturability of Nanoscale CMOS. *2007 IEEE International Electron Devices Meeting*, pages 471–474, 2007. doi: 10.1109/IEDM.2007.4418976.

[22] A. R. Brown, V. Huard, and A. Asenov. Statistical Simulation of Progressive NBTI Degradation in a 45-nm Technology pMOSFET. *IEEE Transactions on Electron Devices*, 57(9):2320–2323, 2010.

[23] D. M. Fleetwood. Total Ionizing Dose Effects in MOS and Low-Dose-Rate-Sensitive Linear-Bipolar Devices. *IEEE Transactions on Nuclear Science*, 60(3): 1706–1730, 2013.

[24] P. S. Winokur. *Basic mechanisms of radiation effects on electronic materials and devices*. 1989.

[25] J. R. Schwank, V. Ferlet-Cavrois, M. R. Shaneyfelt, P. Paillet, and P. E. Dodd. Radiation effects in SOI technologies. *IEEE Transactions on Nuclear Science*, 50 (3):522–538, June 2003. ISSN 0018-9499. doi: 10.1109/TNS.2003.812930.

[26] I. S. Esqueda, H. J. Barnaby, , and M. L. Alles. Two-Dimensional Methodology for modeling radiation-induced off-state leakage in CMOS Technologies. *IEEE Transactions on Nuclear Science*, 52(December):2259–2264, 2005.

[27] C. Peng, Z. Hu, Z. Zhang, H. Huang, B. Ning, and D. Bi. Total ionizing dose effect in 0.2μm PDSOI NMOSFETs with shallow trench isolation. *Microelectronics Reliability*, 54(4):730–737, April 2014. ISSN 00262714. doi: 10.1016/j.microrel.2013.12.016. URL `http://linkinghub.elsevier.com/retrieve/pii/S0026271413004678`.

[28] S. T. Liu, A. Hurst, H. L. Hughes, P. McMarr, J. Benedito, and C. Capasso. Total dose radiation response of a 45nm SOI Technology. *2010 IEEE International SOI Conference*, pages 5–6, 2010.

[29] P. Paillet and M. Gaillardin. Total ionizing dose effects on deca-nanometer fully depleted SOI devices. *IEEE Transaction on Nuclear Science*, 52(6):2345–2352, 2005.

[30] M. Gaillardin, P. Paillet, V. Ferlet-Cavrois, O. Faynot, C. Jahan, and S. Cristoloveanu. Total Ionizing Dose Effects on Triple-Gate FETs. *Nuclear Science, IEEE Transactions on*, 53(6):3158–3165, 2006. doi: 10.1109/tns.2006.884351.

[31] J. P. Colinge, A. Orozco, and J. Rudee. Radiation dose effects in trigate SOI MOS transistors. *IEEE Transactions on Nuclear Science*, 53(6):3237–3241, 2006.

[32] S. Put, E. Simoen, N. Collaert, A. De Keersgieter, C. Claeys, M. Van Uffelen, and P. Leroux. Influence of back-gate bias and process conditions on the gamma-degradation of the transconductance of MuGFETs. *Proceedings of the European Conference on Radiation and its Effects on Components and Systems, RADECS*, 57 (4):14–19, 2009. ISSN 00189499. doi: 10.1109/RADECS.2009.5994545.

[33] E. X. Zhang, D. M. Fleetwood, F. El-mamouni, M. L. Alles, R. D. Schrimpf, W. Xiong, Hobbs. C., K. Akarvadar, and S. Cristoloveanu. Total ionizing dose effects on finFET-based capacitor-less 1T-DRAMs. *IEEE Transactions on Nuclear Science*, 57(6):3298–3304, 2010.

[34] C. C. M. Bordallo, F. F. Teixeira, M. A. G. Silveira, P. G. D. Agopian, E. Simoen, C. Claeys, and J. A. Martino. Influence of X-ray radiation on standard and uniaxial strained triple-gate SOI FinFETs. In *Proceedings of the European Conference on Radiation and its Effects on Components and Systems, RADECS*, 2013. doi: 10.1109/RADECS.2013.6937356.

[35] M. Gaillardin, P. Paillet, V. Ferlet-Cavrois, S. Cristoloveanu, O. Faynot, and C. Jahan. High tolerance to total ionizing dose of Ω-shaped gate field-effect transistors. *Applied Physics Letters*, 88(22):223511, 2006. ISSN 00036951. doi: 10.1063/1.2206097.

[36] J. J. Song, B. K. Choi, E. X. Zhang, R.D. Schrimpf, D. M. Fleetwood, C. H. Park, Y. H. Jeong, and O. Kim. Fin Width and Bias Dependence of the Response of Triple-Gate MOSFETs to Total Dose Irradiation. *IEEE Transactions on Nuclear Science*, 58(6):2871–2875, December 2011. ISSN 0018-9499. doi: 10.1109/TNS.2011.2168977.

[37] F. E. Mamouni, E. X. Zhang, R. D Schrimpf, Daniel M. Fleetwood, and R. A. Reed. Fin-Width Dependence of Ionizing Radiation-Induced Subthreshold-Swing Degradation in. *IEEE Transactions on Nuclear Science*, 56(6):3250–3255, 2009.

[38] I. Chatterjee, E. X. Zhang, B. L. Bhuva, R. a. Reed, M. L. Alles, N. N. Mahatme, D. R. Ball, R. D. Schrimpf, D. M. Fleetwood, D. Linten, E. Simoen, J. Mitard, and C. Claeys. Geometry dependence of total-dose effects in bulk FinFETs. *IEEE Transactions on Nuclear Science*, 61(6):2951–2958, 2014. ISSN 00189499. doi: 10.1109/TNS.2014.2367157.

[39] I. Chatterje, E. X. Zhang, B. L. Bhuva, and D. M. Fleetwood. Length and Fin Number Dependence of Ionizing Degradation in Bulk FinFETs. *2013 IEEE International Reliability Physics Symposium (IRPS)*, pages 1–6, 2013.

[40] T.K. Taur and Y. Ning. *Fundamentals of Modern VLSI design*, volume 2. Cambridge University Press, 2009. ISBN 978-0-521-83294-6.

[41] C. H. Lin, R. Kambhampati, R. J. Miller, T. B. Hook, A. Bryant, W. Haensch, P. Oldiges, I. Lauer, T. Yamashita, V. Basker, T. Standaert, K. Rim, E. Leobandung, H. Bu, and M. Khare. Channel doping impact on FinFETs for 22nm and beyond. *2012 Symposium on VLSI Technology (VLSIT)*, pages 15–16, June 2012. doi: 10.1109/VLSIT.2012.6242438.

[42] M. Gaillardin, P. Paillet, V. Ferlet-Cavrois, J. Baggio, D. McMorrow, O. Faynot, C. Jahan, L. Tosti, and S. Cristoloveanu. Transient radiation response of single- and multiple-gate FD SOI transistors. *IEEE Transactions on Nuclear Science*, 54 (6):2355–2362, 2007. ISSN 00189499. doi: 10.1109/TNS.2007.910860.

[43] O. Weber, O. Faynot, F. Andrieu, F. Allain, P. Scheiblin, J. Foucher, N. Daval, D. Lafond, L. Tosti, L. Brevard, O. Rozeau, M. Marin, F. Boeuf, D. Delprat, K. Bourdelle, B. Nguyen, and S. Deleonibus. High Immunity to Threshold Voltage Variability in Undoped Ultra-Thin FDSOI MOSFETs and its Physical Understanding. *IEEE Electron Devices Meeting, 2008*, pages 10–13, 2009.

[44] X. Wang, A. R. Brown, B. Cheng, and A. Asenov. Statistical Variability and Reliability in Nanoscale FinFETs. *IEEE Electron Devices Meeting, 2008*, pages 103–106, 2011.

[45] V. Ferlet-Cavrois, T. Colladant, P. Paillet, J. L. Leray, O. Musseau, J. R. Schwank, M. R. Shaneyfelt, J. L. Pelloie, and J. du Port de Poncharra. Worst-case bias during total dose irradiation of SOI transistors. *IEEE Transactions on Nuclear Science*, 47 (6):2183–2188, 2000. ISSN 00189499. doi: 10.1109/23.903751.

[46] B. Ning, D. Bi, H. Huang, Z. Zhang, Z. Hu, M. Chen, and S. Zou. Bias dependence of TID radiation responses of 0.13μm partially depleted SOI NMOSFETs. *Microelectronics Reliability*, pages 1–6, August 2012. ISSN 00262714. doi: 10.1016/j.microrel.2012.08.005.

[47] M. Gaillardin, M. Martinez, P. Paillet, F. Andrieu, S. Girard, M. Raine, C. Marcandella, O. Duhamel, N. Richard, and O. Faynot. Impact of SOI Substrate on the Radiation Response of UltraThin Transistors Down to the 20 nm Node. *IEEE Transactions on Nuclear Science*, 60(4):1–7, 2013.

[48] G. X. Duan, C. X. Zhang, E. X. Zhang, J. Hachtel, D. M. Fleetwood, R. D. Schrimpf, R. A. Reed, M. L. Alles, S. T. Pantelides, G. Bersuker, and C. D. Young. Bias Dependence of Total Ionizing Dose Effects in SiGe-SiO_2/HfO_2 pMOS FinFETs. *IEEE Transactions on Nuclear Science*, (December):2834–2838, 2014.

[49] M. Turowski. Nonuniform total-dose-induced charge distribution in shallow-trench isolation oxides. *IEEE Transactions on Nuclear Science*, 51(6):3166–3171, 2004.

[50] R. A. Weeks. Paramagnetic resonance of lattice defects in irradiated quartz. *Journal of Applied Physics*, 27(1956):1376–1381, 1956. ISSN 00218979. doi: 10.1063/1.1722267.

[51] R. A. Weeks and C. M. Nelson. Trapped Electrons In Irradiated Quartz and Silica .2. Electron Spin Resonance. *Journal of the American Ceramic Society*, 43:399–404, 1960. ISSN 1551-2916. doi: 10.1111/j.1151-2916.1960.tb13682.x.

[52] D. L. Griscom and E. J. Friebele. Fundamental radiation-induced defect centers in synthetic fused silicas: Atomic chlorine, delocalized e centers, and a triplet state. *Physical Review B*, 34(December 1986):7524–7533, 1986. ISSN 01631829. doi: 10.1103/PhysRevB.34.7524.

[53] K. L. Yip and W. B. Fowler. Electronic structure of E1 centers in SiO_2. *Physical Review B*, 11:2327–2338, 1975. ISSN 01631829. doi: 10.1103/PhysRevB.11.2327.

[54] M. Boero, A. Pasquarello, J. Sarnthein, and R. Car. Structure and Hyperfine Parameters of E1 Centers in α-Quartz and in Vitreous SiO_2. *Physical Review Letters*, 78(5):887–890, 1997. ISSN 0031-9007. doi: 10.1103/PhysRevLett.78.887.

[55] J. R. Chavez, S. P. Karna, K. Vanheusden, C. P. Brothers, R. D. Pugh, B. K. Singaraju, W. L. Warren, and R. A. B. Devine. Microscopic structure of the E_δ' center in amorphous SiO_2: A first principles quantum mechanical investigation. *IEEE Transactions on Nuclear Science*, 44(December):1799–1803, 1997. ISSN 00189499. doi: 10.1109/23.658945.

[56] K. Vanheusden and Stesmans A. Characterization and depth profiling of E' defects in buried SiO_2. *Journal of Applied Physics*, 74(1):275–283, 1993. ISSN 00218979. doi: 10.1063/1.354103.

[57] L. Zhang and R. G. Leisure. The E_δ' and triplet-state centers in x-irradiated high-purity amorphous SiO_2. *J. Appl. Phys.*, 80(7):3744, 1996. ISSN 00218979. doi: 10.1063/1.363279.

[58] G. Buscarino, S. Agnello, and F. M. Geraldi. Delocalized nature of the E' center in amorphous silicon dioxide. *Physical Review Letters*, 94(12):1–4, 2005. ISSN 00319007. doi: 10.1103/PhysRevLett.94.125501.

[59] Z. Y. Lu, C. J. Nicklaw, D. M. Fleetwood, R. D. Schrimpf, and S. T. Pantelides. Structure, Properties, and Dynamics of Oxygen Vacancies in Amorphous SiO_2. *Physical Review Letters*, 89:285505, 2002. ISSN 0031-9007. doi: 10.1103/PhysRevLett.89.187201.

[60] S. T. Pantelides, Z. Y. Lu, C. Nicklaw, T. Bakos, S. N. Rashkeev, D. M. Fleetwood, and R. D. Schrimpf. The E center and oxygen vacancies in SiO_2. *Journal of Non-Crystalline Solids*, 354(2008):217–223, 2008. ISSN 00223093. doi: 10.1016/j.jnoncrysol.2007.08.080.

[61] B. R. Tuttle and S. T. Pantelides. Vacancy-related defects and the Eδ center in amorphous silicon dioxide: Density functional calculations. *Physical Review B - Condensed Matter and Materials Physics*, 79:11–15, 2009. ISSN 10980121. doi: 10.1103/PhysRevB.79.115206.

[62] K. L. Brower, P. M. Lenahan, and P. V. Dressendorfer. Defects and impurities in thermal oxides on silicon. *Applied Physics Letters*, 41(May 2016):251–253, 1982. ISSN 00036951. doi: 10.1063/1.93484.

[63] T. P. Ma and P. V. Dressendorfer. *Ionizing Radiation Effects in MOS Devices and Circuits*. Willey-Interscience, 1989.

[64] D. B. Brown and N. S. Saks. Time dependence of radiation-induced interface trap formation in metal-oxide-semiconductor devices as a function of oxide thickness and applied field. *Journal of Applied Physics*, 70(1991):3734–3747, 1991. ISSN 00218979. doi: 10.1063/1.349226.

[65] D. L. Griscom. Hydrogen model for radiation-induced interface states in SiO_2-on-Si Structures: A review of the evidence. *Journal of Electronic Materials*, 21: 763–767, 1992. doi: 10.1007/BF02655608.

[66] E. Patrick, N. Rowsey, and M. E. Law. Total Dose Radiation Damage: A Simulation Framework. *IEEE Transactions on Nuclear Science*, 62(4):1650–1657, 2015. doi: 10.1109/TNS.2015.2425226.

[67] J. H. Stathis and E. Cartier. Atomic Hydrogen Reactions with Pb Centers at the (100) Si/SiO_2 Interface. *Applied Physics Letters*, 72(April):2745 – 2748, 1994.

[68] S.T. Pantelides, S.N. Rashkeev, R. Buczko, D.M. Fleetwood, and R.D. Schrimpf. Reactions of hydrogen with Si-SiO_2 interfaces. *IEEE Transactions on Nuclear Science*, 47(6):2262–2268, 2000. ISSN 00189499. doi: 10.1109/23.903763.

[69] S. N. Rashkeev, D. M. Fleetwood, R. D. Schrimpf, and S. T. Pantelides. Defect Generation by Hydrogen at the Si-SiO_2 Interface. *Physical Review Letters*, 87: 165506, 2001. ISSN 0031-9007. doi: 10.1103/PhysRevLett.87.165506.

[70] S. N. Rashkeev, D. M. Fleetwood, R. D. Schrimpf, and S. T. Pantelides. Proton-induced defect generation at the Si-SiO_2 interface. *IEEE Transactions on Nuclear Science*, 48(December):2086–2092, 2001. ISSN 00189499. doi: 10.1109/23.983177.

[71] H. Jafari, S. A. H. Feghhi, and S. Boorboor. The effect of interface trapped charge on threshold voltage shift estimation for gamma irradiated MOS device. *Radiation Measurements*, 73(2015):69–77, 2014. ISSN 13504487. doi: 10.1016/j.radmeas.2014.12.008.

[72] P. E. Bunson, M. D. Ventra, S. T. Pantelides, R. D. Schrimpf, and K. F. Galloway. Ab initio calculations of H^+ energetics in SiO_2: Implications for transport. *IEEE Transactions on Nuclear Science*, 46(6):1568–1573, December 1999. ISSN 0018-9499. doi: 10.1109/23.819122.

[73] B. R. Tuttle, D. R. Hughart, R. D. Schrimpf, D. M. Fleetwood, and S. T. Pantelides. Defect interactions of H2 in SiO_2: Implications for ELDRS and latent interface trap buildup. *IEEE Transactions on Nuclear Science*, 57(December):3046–3053, 2010. ISSN 00189499. doi: 10.1109/TNS.2010.2086076.

[74] X. J. Chen, H. J. Barnaby, B. Vermeire, K. Holbert, D. Wright, R. L. Pease, G. Dunham, D. G. Platteter, J. Seiler, S. McClure, and P. Adell. Mechanisms of enhanced radiation-induced degradation due to excess molecular hydrogen in bipolar oxides, 2007. ISSN 00189499.

[75] I. G. Batyrev, D. Hughart, R. Durand, M. Bounasser, B. R. Tuttle, D. M. Fleetwood, R. D. Schrimpf, S. N. Rashkeev, G. W. Dunham, M. Law, and S. T. Pantelides. Effects of hydrogen on the radiation response of bipolar transistors: Experiment and modeling. *IEEE Transactions on Nuclear Science*, 55(December):3039–3045, 2008. ISSN 00189499. doi: 10.1109/TNS.2008.2009353.

[76] H. J. Barnaby, M. L. McLain, I. S. Esqueda, and J. C. Xiao. Modeling Ionizing Radiation Effects in Solid State Materials and CMOS Devices. *IEEE Transactions on Circuits and Systems I: Regular Papers*, 56(August):1870–1883, 2009. ISSN 1549-8328. doi: 10.1109/TCSI.2009.2028411.

[77] H. P. Hjalmarson, R. L. Pease, S. C. Witczak, M. R. Shaneyfelt, J. R. Schwank, A. H. Edwards, C. E. Hembree, and T. R. Mattsson. Mechanisms for Radiation Dose-Rate Sensitivity of Bipolar Transistors. *IEEE Transactions on Nuclear Science*, 50(6 I):1901–1909, 2003. ISSN 00189499. doi: 10.1109/TNS.2003.821803.

[78] H. P. Hjalmarson, R. L. Pease, C. E. Hembree, R. M. Van Ginhoven, and P. A. Schultz. Dose-rate dependence of radiation-induced interface trap density in silicon bipolar transistors. *Nuclear Instruments and Methods in Physics Research, Section B: Beam Interactions with Materials and Atoms*, 250:269–273, 2006. ISSN 0168583X. doi: 10.1016/j.nimb.2006.04.122.

[79] H. P. Hjalmarson, R. L. Pease, and R. A. B. Devine. Calculations of Radiation Dose-Rate Sensitivity of Bipolar Transistors. *IEEE Transactions on Nuclear Science*, 55(6):3009–3015, December 2008. ISSN 0018-9499. doi: 10.1109/TNS.2008.2007487.

[80] R. L. Pease, R. D. Schrimpf, and D. M. Fleetwood. ELDRS in Bipolar Linear Circuits: A Review. *IEEE Transactions on Nuclear Science*, 56:1894–1908, 2009. ISSN 0018-9499. doi: 10.1109/TNS.2008.2011485.

[81] S. T. Pantelides, L. Tsetseris, M. J. Beck, S. N. Rashkeev, G. Hadjisavvas, I. G. Batyrev, B. R. Tuttle, A. G. Marinopoulos, X. J. Zhou, D. M. Fleetwood,

and R. D. Schrimpf. Performance, reliability, radiation effects, and aging issues in microelectronics - From atomic-scale physics to engineering-level modeling. *Solid-State Electronics*, 54(9):841–848, 2010. ISSN 00381101. doi: 10.1016/j.sse.2010.04.041.

[82] I. S. Esqueda, H. J Barnaby, and P. C Adell. Modeling the Effects of Hydrogen on the Mechanisms of Dose Rate Sensitivity. *Nuclear Science, IEEE Transactions on*, 59(4):701–706, 2012. doi: 10.1109/tns.2012.2195201.

[83] N. L. Rowsey, M. E. Law, R. D Schrimpf, D. M. Fleetwood, B. R. Tuttle, and S. T. Pantelides. Mechanisms Separating Time-Dependent and True Dose-Rate Effects in Irradiated Bipolar Oxides. *Nuclear Science, IEEE Transactions on*, 59(6):3069–3076, 2012. doi: 10.1109/TNS.2012.2222669.

[84] S. N. Rashkeev, C. R. Cirba, D. M. Fleetwood, R. D. Schrimpf, S. C. Witczak, A. Michez, and S. T. Pantelides. Physical model for enhanced interface-trap formation at low dose rates. *IEEE Transactions on Nuclear Science*, 49(6):2650–2655, December 2002. ISSN 0018-9499. doi: 10.1109/TNS.2002.805387.

[85] S. Humphries. *Finite Element Methods for Electromagnetics*. Albuquerque, New Mexico, 2010. ISBN 0-8493-1668-5.

[86] J. L. Leray and P. Paillet. Oxide charge modeling with CEA-TRAPPOX code version 4. Comparison of trapping models on desktop computer. *Radiation and Its Effects*, pages 53–58, 1999.

[87] W. M. Haynes. CRC handbook of chemistry and physics: a ready-reference book of chemical and physical data, 2011. ISSN 0889-311X.

[88] J. C. Nicklaw and R. Weller. *Multi-level modelling of Total Ionizing Dose in a-SiO$_2$: First principles to circuits*. PhD thesis, Vanderbilt University, 2003.

[89] Integrated Systems Engineering. ISE TCAD Release 10.0, DESSIS, 2004.

[90] S. S. Nekrashevich and V. A. Gritsenko. Electronic structure of silicon dioxide (a review). *Physics of the Solid State*, 56:207–222, 2014. ISSN 1063-7834. doi: 10.1134/S106378341402022X.

[91] C. M. Wu and E. S. Yang. Carrier transport across heterojunction interfaces. *Solid State Electronics*, 22(3):241–248, 1979. ISSN 00381101. doi: 10.1016/0038-1101(79)90028-5.

[92] K. Horio and H. Yanai. Numerical modeling of heterojunctions including the thermionic emission mechanism at the heterojunction interface. *IEEE transactions on electron devices*, 37(4), 1990.

[93] N. Sano and K. Matsuzawa. Role of long-range and short-range Coulomb potentials in threshold characteristics under discrete dopants in sub-0.1 μm Si-MOSFETs. *Devices Meeting, 2000*, pages 275–278, 2000.

[94] synopsys Inc. Sentaurus Mesh User Guide. 2015.

[95] A. Wettstein, O. Penzin, E. Lyumkis, and W. Fichtner. Random dopant fluctuation modelling with the impedance field method. *International Conference on Simulation of Semiconductor Processes and Devices, SISPAD*, (October 2003):91–94, 2003. doi: 10.1109/SISPAD.2003.1233645.

[96] K. El Sayed, A. Wettstein, S. D. Simeonov, E. Lyumkis, and B. Polsky. Investigation of the statistical variability of static noise margins of SRAM cells using the statistical impedance field method. *IEEE Transactions on Electron Devices*, 59(6): 1738–1744, 2012. ISSN 00189383. doi: 10.1109/TED.2012.2189860.

[97] S. Lee, B. Jagannathan, S. Narasimha, A. Chou, N. Zamdmer, R. Williams, L. Wagner, J. Kim, J. O. Plouchart, J. Pekarik, S. Springer, and G. Freeman. Record RF performance of 45-nm SOI CMOS Technology. *IEEE Electron Device Meeting*, 2007.

[98] C. Auth, C. Allen, A. Blattner, D. Bergstrom, M. Brazier, M. Bost, M. Buehler, V. Chikarmane, T. Ghani, T. Glassman, R. Grover, W. Han, D. Hanken, M. Hattendorf, P. Hentges, R. Heussner, J. Hicks, D. Ingerly, P. Jain, S. Jaloviar, R. James, D. Jones, J. Jopling, S. Joshi, C. Kenyon, H. Liu, R. Mcfadden, B. Mcintyre, J Neirynck, C. Parker, L. Pipes, I. Post, S. Pradhan, M. Prince, S. Ramey, T. Reynolds, J. Roesler, J. Sandford, J. Seiple, P. Smith, C. Thomas, D. Towner, T. Troeger, C. Weber, P. Yashar, K. Zawadzki, and K. Mistry. A 22nm High Performance and Low-Power CMOS Technology Featuring Fully-Depleted Tri-Gate Transistors , Self-Aligned Contacts and High Density MIM Capacitor. *Symposium on VLSI Technology Digest of Technical Papers*, 980(2003):131–132, 2012.

[99] Y. M. Lin, K. A. Jenkins, A. Valdes-Garcia, J. P. Small, D. B. Farmer, and P. Avouris. Operation of graphene transistors at gigahertz frequencies. *Nano letters*, 9(2): 422–426, 2009. doi: 10.1021/nl803316h.

[100] B. Radisavljevic, A. Radenovic, J. Brivio, V. Giacometti, and A. Kis. Single-layer MoS2 transistors. *Nature nanotechnology*, 6(3):147–50, 2011. doi: 10.1038/nnano.2010.279.

[101] C. X. Zhang and E. X. Zhang. Total ionizing dose effects and reliability of graphene-based non-volatile memory devices. *IEEE Aerospace Conference*, pages 1–8, 2013.

[102] K. Potter, K. Morgan, C. Shaw, P. Ashburn, William R. W., and C. H. De Groot. Total ionizing dose response of fluorine implanted Silicon-On-Insulator buried

oxide. *Microelectronics Reliability*, 54(9-10):2339–2343, 2014. doi: 10.1016/j.microrel.2014.07.018.

[103] E. H. Nicollian and A. Goetzberger. Lateral ac current flow model for metal-insulator-semiconductor capacitors. *IEEE Transactions on Electron Devices*, 12(3): 108–117, Mar 1965. ISSN 0018-9383. doi: 10.1109/T-ED.1965.15465.

[104] Raymond T. Tung. The physics and chemistry of the Schottky barrier height. *Applied Physics Reviews*, 1(1):011304, mar 2014. doi: 10.1063/1.4858400.

[105] J. R. Schwank. Basic mechanisms of radiation effects in the natural space radiation environment. 1994.

[106] C. L Claeys and E. Simoen. *Radiation effects in advanced semiconductor materials and devices*. Springer, 2002. doi: 10.1007/978-3-662-04974-7.

[107] A. H. Johnston, R. T. Swimm, G. R. Allen, and T. F. Miyahira. Total Dose Effects in CMOS Trench Isolation Regions. *IEEE Transactions on Nuclear Science*, 56(4): 1941–1949, August 2009. ISSN 0018-9499. doi: 10.1109/TNS.2009.2019273.

[108] W. L. Warren, D. M. Shaneyfelt, D. M. Fleetwood, J. R. Schwank, P. S. Winokur, and Devine R. A. B. Microscopic nature of border traps in MOS oxides. *IEEE Transactions on Nuclear Science*, 41:1817, 1994.

[109] J. T. Ryan, A. Matsuda, J. P. Campbell, and K. P. Cheung. Interface-state capture cross section: Why does it vary so much? *Applied Physics Letters*, 106(2015): 163503, 2015. ISSN 0003-6951. doi: 10.1063/1.4919100.

[110] S.N. Rashkeev, D.M. Fleetwood, R.D. Schrimpf, and S.T. Pantelides. Effects of hydrogen motion on interface trap formation and annealing. *IEEE TNS*, 51(December):3158–3165, 2004. ISSN 0018-9499. doi: 10.1109/TNS.2004.839202.

[111] D. C. Mayer. Modes of operation and radiation sensitivity of ultrathin SOI transistors. *IEEE Transactions on Electron Devices*, 31(5):1280–1288, 1990.

[112] F. T. Brady, J. D. Maimon, and M. J. Hurt. A scaleable, radiation hardened shallow trench isolation. *IEEE Transactions on Nuclear Science*, 46(December 1999):1836–1840, 1999.

[113] Synopsys. Process and Device Simulation of Partially Depleted SOI MOSFET, 2012.

[114] S. Narasimha, K. Onishi, H. M. Nayfeh, a. Waite, M. Weybright, J. Johnson, C. Fonseca, D. Corliss, C. Robinson, M. Crouse, D. Yang, C-H.J. Wu, a. Gabor, T. Adam, I. Ahsan, M. Belyansky, L. Black, S. Butt, J. Cheng, a. Chou, G. Costrini, C. Dimitrakopoulos, a. Domenicucci, P. Fisher, a. Frye, S. Gates,

S. Greco, S. Grunow, M. Hargrove, J. Holt, S-J. Jeng, M. Kelling, B. Kim, W. Landers, G. Larosa, D. Lea, M.H. Lee, X. Liu, N. Lustig, a. McKnight, L. Nicholson, D. Nielsen, K. Nummy, V. Ontalus, C. Ouyang, X. Ouyang, C. Prindle, R. Pal, W. Rausch, D. Restaino, C. Sheraw, J. Sim, a. Simon, T. Standaert, C. Y. Sung, K. Tabakman, C. Tian, R. Van Den Nieuwenhuizen, H. Van Meer, a. Vayshenker, D. Wehella-Gamage, J. Werking, R. C. Wong, S. Wu, J. Yu, R. Augur, D. Brown, X. Chen, D. Edelstein, a. Grill, M. Khare, Y. Li, S. Luning, J. Norum, S. Sankaran, D. Schepis, R. Wachnik, R. Wise, C. Wann, T. Ivers, and P. Agnello. High Performance 45-nm SOI Technology with Enhanced Strain, Porous Low-k BEOL, and Immersion Lithography. pages 1–4. IEEE, 2006. ISBN 1-4244-0438-X. doi: 10.1109/IEDM.2006.346879.

[115] M. Chudzik, B. Doris, R. Mo, J. Sleight, E. Cartier, C. Dewan, D. Park, H. Bu, W. Natzle, W. Yan, C. Ouyang, K. Henson, D. Boyd, S. Callegari, R. Carter, D. Casarotto, M. Gribelyuk, M. Hargrove, W. He, Y. Kim, B. Linder, N. Moumen, V. K. Paruchuri, J. Stathis, M. Steen, A. Vayshenker, X. Wang, S. Zafar, T. Ando, R. Iijima, M. Takayanagi, V. Narayanan, R. Wise, Y. Zhang, R. Divakaruni, M. Khare, and T. C. Chen. High-Performance High- K / Metal Gates for 45nm CMOS and Beyond with Gate-First Processing. *VLSI Technology, 2007 IEEE Symposium on*, pages 194–195, 2007. doi: 10.1109/VLSIT.2007.4339689.

[116] H. S. Yang, R. Malik, S. Narasimha, Y. Li, R. Divakaruni, P. Agnello, S. Allen, a. Antreasyan, J.C. Arnold, K. Bandy, M. Belyansky, a. Bonnoit, G. Bronner, V. Chan, X. Chen, Z. Chen, D. Chidambarrao, a. Chou, W. Clark, S.W. Crowder, B. Engel, H. Harifuchi, S.F. Huang, R. Jagannathan, F.F. Jamin, Y. Kohyama, H. Kuroda, C. W. Lai, H.K. Lee, W.-H. Lee, E. H. Lim, W. Lai, a. Mallikarjunan, K. Matsumoto, a. McKnight, J. Nayak, H. Y. Ng, S. Panda, R. Rengarajan, M. Steigerwalt, S. Subbanna, K. Subramanian, J. Sudijono, G. Sudo, S.-P. Sun, B. Tessier, Y. Toyoshima, P. Tran, R. Wise, R. Wong, I.Y. Yang, C.H. Wann, L.T. Su, M. Horstmann, Th Feudel, a. Wei, K. Frohberg, G. Burbach, M. Gerhardt, M. Lenski, R. Stephan, K. Wieczorek, M. Schaller, H. Salz, J. Hohage, H. Ruelke, J. Klais, P. Huebler, S. Luning, R. van Bentum, G. Grasshoff, C. Schwan, E. Ehrichs, S. Goad, J. Buller, S. Krishnan, D. Greenlaw, M. Raab, and N. Kepler. Dual stress liner for high performance sub-45nm gate length SOI CMOS manufacturing. *Applied Physics Letters*, 75:1075–1077, 2004. ISSN 00036951. doi: 10.1109/IEDM.2004.1419385.

[117] N. Rezzak, M. L. Alles, R. D. Schrimpf, S. Kalemeris, L. W. Massengill, J. Sochacki, and H. J. Barnaby. The sensitivity of radiation-induced leakage to STI topology and sidewall doping. *Microelectronics Reliability*, 51(5):889–894, May 2011. ISSN 00262714. doi: 10.1016/j.microrel.2010.12.013.

[118] F. T. Brady and H. L. Hughes. Total dose hardening of SIMOX buried oxides for fully depleted devices in rad-tolerant applications. *IEEE Transaction on Nuclear Science*, 43(6):2646–2650, 1996.

[119] M. Nandakumar and A. Chatterjee. Shallow trench isolation for advanced ULSI CMOS technologies. *IEDM Meeting 1998*, pages 133–136, 1998.

[120] A. H. Johnston. Low dose rate effects in shallow trench isolation regions. *IEEE Transactions on Nuclear Science*, 57(December):3279–3287, 2010.

[121] G. I. Zebrev, M. S. Gorbunov, V. E. Shunkov, P. N. Osipenko, B. V. Vasilegin, and A. V. Sogoyan. Physical Modeling and Circuit Simulation of Hardness of SOI Transistors and Circuits for Space Applications. *RADECS 2006 report*, 2006.

[122] M. L. Alles, H. L. Hughes, D. R. Ball, P. J. McMarr, and R. D. Schrimpf. Total-ionizing-dose response of narrow, long channel 45 nm PDSOI transistors. *IEEE Transactions on Nuclear Science*, 61(6):2945–2950, 2014. ISSN 00189499. doi: 10.1109/TNS.2014.2366725.

[123] A. Asenov. Random dopant induced threshold voltage lowering and fluctuations in sub-0.1 μm MOSFET's: A 3-D "atomistic" simulation study. *IEEE Transactions on Electron Devices*, 45(12):2505–2513, 1998. ISSN 00189383. doi: 10.1109/16.735728.

[124] A. Asenov, G. Slavcheva, A. R. Brown, J. H. Davies, and S. Saini. Increase in the random dopant induced threshold fluctuations and lowering in sub-100 nm MOSFETs due to quantum effects: A 3-D density-gradient simulation study. *IEEE Transactions on Electron Devices*, 48(April):722–729, 2001. ISSN 00189383. doi: 10.1109/16.915703.

[125] I. Chatterjee, E. X. Zhang, B. L. Bhuva, M.A. Alles, R. D. Schrimpf, D. M. Fleetwood, Y. P. Fang, and A. Oates. Bias Dependence of Total-Dose Effects in Bulk FinFETs. *IEEE Transactions on Nuclear Science*, 60(6):4476–4482, 2013.

[126] Synopsys Inc. Device Monte Carlo Simulation Methodology of Two-dimensional FinFET Slices. 2012.

[127] C C Wu, D W Lin, a Keshavarzi, C H Huang, C T Chan, C H Tseng, C L Chen, C Y Hsieh, K Y Wong, M L Cheng, T H Li, and Y C Lin. High Performance 22/20nm FinFET CMOS Devices with Advanced High-K/Metal Gate Scheme. *IEEE International Electron Devices Meeting*, pages 600–603, 2010.

[128] J. Kavalieros, B. Doyle, S. Datta, G. Dewey, M. Doczy, B. Jin, D. Lionberger, M. Metz, W. Rachmady, M. Radosavljevic, U. Shah, N. Zelick, and R. Chau. Tri-Gate Transistor Architecture with High-k Gate Dielectrics , Metal Gates and Strain Engineering. In *2006 Symposium on VLSI Technology Digest of Technical Papers*, number c, pages 5–6, 2006. ISBN 1424400058.

[129] J. P. Colinge. *FinFETs and Other Multi-Gate Transistors*. Springer US, Boston, MA, 2008. ISBN 978-0-387-71751-7. doi: 10.1007/978-0-387-71752-4.

[130] Synopsys Inc. Three-dimensional Simulations of Raised Source Drain FinFET. 2011.

[131] C. H. Jan, U. Bhattacharya, R. Brain, S. J. Choi, G. Curello, G. Gupta, W. Hafez, M. Jang, M. Kang, K. Komeyli, T. Leo, N. Nidhi, L. Pan, J. Park, K. Phoa, a. Rahman, C. Staus, H. Tashiro, C. Tsai, P. Vandervoorn, L. Yang, J. Y. Yeh, and P. Bai. A 22nm SoC platform technology featuring 3-D tri-gate and high-k/metal gate, optimized for ultra low power, high performance and high density SoC applications. *2012 International Electron Devices Meeting*, pages 3.1.1–3.1.4, December 2012. doi: 10.1109/IEDM.2012.6478969.

[132] Mark Bohr. 14 nm Process Technology: Opening New Horizons. In *Intel Developer Forum (IDF'14)*, 2014.

[133] A Hikavyy, I Zyulkov, H Mertens, L Witters, R Loo, and N Horiguchi. Use of high order precursors for manufacturing Gate all around devices. *Materials Science in Semiconductor Processing*, (October):33139, 2016. doi: 10.1016/j.mssp.2016.10.044.

[134] A Veloso, A De Keersgieter, P Matagne, N Horiguchi, and N Collaert. Advances on doping strategies for triple-gate fi nFETs and lateral gate-all- around nanowire FETs and their impact on device performance. *Materials Science in Semiconductor Processing*, (October):0–1, 2016. doi: 10.1016/j.mssp.2016.10.018.

[135] Dong-Il Moon, Jin-Woo Han, and Meyya Meyyappan. Fabrication of a Silicon Nanowire on a Bulk Substrate by Use of a Plasma Etching and Total Ionizing Dose Effects on a Gate-All-Around Field-Effect Transistor Artificial satellites Fabrication of Suspended SiNWs Radiation Effects on SiNW GAA FETs Advantage. Technical report, NASA Ames Research Center, 2016.

[136] D. Landru, F. Allibert, N. Daval, and O. Kononchuk. UTBOX SOI Substrate with Composite Insulating Layer. *ECS Journal of Solid State Science and Technology*, 2 (6):Q83–Q87, 2013. doi: 10.1149/2.014306jss.

[137] ITRS. The International Technology Roadmap for Semiconductors, 2015. URL `http://www.itrs2.net`.

[138] T. P. Morgan. Inside Intel's deal to let FPGA biz Altera use its 22nm Tri-Gate fabs, 2013. URL `https://www.theregister.co.uk/2013/02/26/intel_altera_fab_deal/`.

[139] Li Tao, Eugenio Cinquanta, Daniele Chiappe, Carlo Grazianetti, Marco Fanciulli, Madan Dubey, Alessandro Molle, and Deji Akinwande. Silicene field-effect transistors operating at room temperature. *Nature Nanotechnology*, 10(3):227–231, 2015. doi: 10.1038/nnano.2014.325.

[140] Cory D. Cress, James G. Champlain, Ivan S. Esqueda, Jeremy T. Robinson, Adam L. Friedman, and Julian J. McMorrow. Total ionizing dose induced charge carrier scattering in graphene devices. *IEEE Transactions on Nuclear Science*, 59 (6):3045–3053, 2012. ISSN 00189499. doi: 10.1109/TNS.2012.2221479.